From the body to the brain: Studying drug delivery and physiological interactions using MRI

by

Miranda Dawson

B.S., Bioengineering, University of Illinois at Urbana-Champaign (2018)

Submitted to the Department of Biological Engineering
in partial fulfillment of the requirements for the degree of

DOCTOR OF PHILOSOPHY

at the

MASSACHUSETTS INSTITUTE OF TECHNOLOGY

September 2024

Authored by: Miranda Dawson
Department of Biological Engineering
June 24, 2024

Certified by: Alan Jasanoff
Professor of Biological Engineering, Thesis Supervisor

Accepted by: Forest White
Professor of Biological Enginerring
Graduate Officer, Department of Biological Engineering

Thesis Committee Members:

Professor Alan Jasanoff
Thesis Supervisor
Professor of Biological Engineering, Brain and Cognitive Sciences, Nuclear Science and Engineering, MIT

Professor Angela N. Koehler
Thesis Chair
Associate Professor of Biological Engineering, MIT

Professor Guoping Feng
James W. (1963) and Patricia T. Poitras Professor of Brain and Cognitive Sciences, MIT

From the body to the brain: Studying drug delivery and physiological interactions using MRI

by

Miranda Dawson

Submitted to the Department of Biological Engineering
on June 24, 2024 in partial fulfillment of the requirements for the degree of

DOCTOR OF PHILOSOPHY

ABSTRACT

The brain is in continuous communication with the rest of the body. Nerves connect the peripheral and central nervous system, and complex vasculature networks selectively permit passage of small molecules with an exogenous origin into the brain parenchyma. Although brain-body interactions underpin a host of cognitive and physiological phenomena, they are often overlooked in studies of brain biology and mental function. We studied aspects of the interaction between brain and body using functional and molecular magnetic resonance imaging (MRI), in combination with other tools. In a first project, we examined properties of the blood-brain barrier (BBB). The BBB is a highly selective collection of endothelial cells and tight junction proteins that restrict passage of extracerebral substances from the blood vessels into the brain tissue. We disrupted and bypassed the BBB to deliver an MRI contrast agent and quantitatively assessed the resulting contrast dynamics. We discovered that individual brain regions display method-independent susceptibility to BBB disruption and washout, suggesting principles for calibrating drug delivery and understanding the propensity for chemical exchange across the BBB. We then used one of the wide-field brain delivery techniques to apply a novel contrast agent for the study of the cholinergic system, a neurochemical pathway important for motor control mechanisms in both the central and peripheral nervous systems. Kinetic modeling of probe distributions revealed intrinsic localization of cholinergic enzymes. Finally, we applied related neuroimaging tools to an animal model of substance abuse, a pathology for which brain-body interactions are particularly engaged but underappreciated. We designed a study to investigate the role of the insula, a cortical mediator of peripheral physiological signals, in responses to opioid exposure. With molecular imaging approaches, we show the insula shapes drug-dependent brain phenotypes and physiological responses during substance exposure and withdrawal. In all, this work serves as a demonstration of the power of quantitative neuroimaging methods for multifaceted investigation of brain and body relationships.

Thesis supervisor: Alan Jasanoff
Title: Professor of Biological Engineering

Acknowledgments

Thank you to my advisor, Alan Jasanoff, for being a kind and supportive mentor. Your guidance has allowed me to grow exponentially as an academic and scientist. I still remember our first meeting. We discussed topics ranging from neuroimaging to Cartesian philosophy, and it was then I knew I had found my match in an advisor.

Thank you to my committee. Angela Koehler, you have been an extremely supportive committee chair and have provided feedback and encouragement during crucial points in this thesis. Guoping Feng, your ability to provide deeper neuroscientific insight has been very valuable in this process.

Thank you to my many labmates over the years who have contributed to moments of collaboration, insightful conversation, and laughter. Some special shout out goes to Sarah, your guidance is the reason that I (a former benchtop engineer that was married to her pipette) am now a proper *in vivo* scientist. Your teaching enabled me to enter the exciting world of experimental neuroscience. To Sajal, it has been a joy working with you. Whether we are troubleshooting at the 7T MRI or scouring obscure scientific literature at Hayden Library, you always keep a positive attitude and persevere. To Kevin, thanks to you, I now have an above average knowledge of axolotol, beetle, and quail husbandry. To Greg, you introduced me to the love of biking. To Souparno, you encouraged me to stay true to myself even in those uncertain, early days of graduate school. To Diane, your support has been invaluable over the years.

Thank you to my cohort, I am thankful to have gone through the ups and downs of graduate school with such intelligent and thoughtful people. From deriving 20.420 equations in "The Dungeon" to years of Secret Santa exchanges, it has been a pleasure.

Thank you to Ulya, Alli, Jackie, Blake, and my many other friends along the way. You have been my second family here in Boston. I am thankful to have friendships where I feel seen and embraced.

And finally, thank you to my family. To my grandmother, thank you for rejecting your numerous marriage proposals from men in rural Indiana to instead pursue a college degree. You set the example for the women in the generations that followed. Mitchell, thank you for the phone calls during our respective commutes from work. No matter our age, you will always be my little brother. To my father, I am grateful for the sacrifices you have made for our family. You taught me not to fear challenge. To my mother, thank you for encouraging my curiosity and embracing my quirks. It is thanks to you, I am here today.

Contents

List of Figures

List of Tables

Chapter 1

Introduction

The brain is in continuous communication with the rest of the body. Nerves connect the peripheral and central nervous system, and complex vasculature networks selectively permit passage of small molecules with an exogenous origin into the brain parenchyma [1–3]. While brain-body connections are explicit in the study of physiological functions such as breathing and heart rate, when the brain is studied in the context of mind, behavior, and cognition, there is a tendency to approach the brain independently of the remainder of the body [4]. This is likely due to the fact that the brain is treated as a physical substrate of mind. A body of literature indicates humans are intuitive Dualists - that is they consider mind distinct from their corporeal form [5]. What emerges is a contradiction. We acknowledge the brain as a biological organ physically communicating with the rest of the body. Yet, we still approach neuroscientific questions with our intuitions of brain-body duality. To approach neuroscience with an appreciation for brain and body integration, we require adequate tools and methods to support incisive hypotheses.

This thesis approaches this nexus using the tools of functional and molecular MRI. This includes characterizing physical routes for bypassing the blood-brain barrier (BBB), applying a cholinergic agent designed to study aspects of brain-body biology, and discerning functional significance of brain-body coupling in a pathology that is,

at times, attributed exclusively to the brain.

1.1 Varied spatiotemporal approaches in neuroscience

The tools used to study the nervous system dictate the spatiotemporal scope of hypotheses. In fact, these differing scales lead to a bifurcation of molecular and systems-level neuroscience. The tools available to each subfield determine the questions that researchers are able to ask. For instance, molecular scientists may choose to investigate the structure of cells in the nervous system with post-mortem histology, or they may employ patch clamp electrophysiology to study how dynamics in neurotransmitter release alter neuronal activity [6, 7]. Modern-day neuroscience was born out of these molecular investigations. As early as the 1880s, the scientist Santiago Ramon y Cajal was using histological staining methods to make foundational discoveries. Incubating tissue in potassium dichromate and silver nitrate, he was able to visualize neurons which lead to his conclusion that the nervous system is represented by individual cellular elements. The concept of a synapse in which information travels along axons to cell bodies and dendrites emerged from this work. [8, 9]. Now with modern optical techniques, it is possible to image at resolutions as precise as 100s of nanometers. This has led to discoveries ranging from the structure of striosomal and dopaminergic fibers in dendrons to the organization of chromatin in nuclear structures [10].

While microscale structure and function is important, so are the larger-scale dynamic processes governing the living brain. All stimuli achieve effects through multiregional interactions that ultimately give rise to coordinated behavior. Studying structures or activity in a single region cannot possibly explain how brain activity gives rise to cognition and action. This is where systems neuroscientists play a key role. Systems neuroscientists employ a variety of tools including electrode arrays, positron emission tomography (PET), magnetic resonance imaging (MRI), wide-field

optical imaging, and computational modeling [11].

A natural question is how we can relate these molecular events to their influence on larger scale systems and vice versa. For example, in studying reward, one may ask how influxes of dopamine in subcortical neurons influence downstream activity in the cerebral cortex. The effort to create and employ tools at this spatiotemporal intersection has led to the emerging field of "molecular systems neuroscience" in which molecular-level events can be mapped to macroscopic brain states and behavior. [12].

1.2 Limits of current neurobiological methods in bridging the spatiotemporal gap

The capacity of our tools dictates the scientific questions we are able to explore (Figure 1). Often, spatial information must be sacrificed for temporal precision and vice versa. For instance, while RNA sequencing allows us to obtain a comprehensive list of transcriptional activity across the whole brain, it is restricted to presenting us the activity at precisely one point in time as it relies on post mortem tissue [13]. Collecting multiple points requires large cohorts and does not allow serial measurements from the same subject [14]. Alternatively, optical gene reporters (i.e., fluorophores and luciferases) allow for a temporally dynamic read-out of gene expression, but they often lack spatial range. This is because optical imaging is limited in deeper tissue as a result of light scattering and absorption [15]. Recordings using these optical reporters often require implantation of cranial windows to bypass the skull, but even this only provides information from a fraction of the brain and fails to capture whole-brain dynamics [16]. How then do we achieve molecular information with greater spatiotemporal resolution and range?

Noninvasive imaging methods famous for their application in medicine, such as positron emission tomography (PET) and magnetic resonance imaging (MRI), offer a promising solution. Both methods allow volumetric imaging across the whole brain. While PET relies on the detection of radioactive tracers, MRI tracks magnetic prop-

erties of tissue. When comparing the advantages of selecting either PET to MRI for a study, a major consideration is spatial resolution. PET offers resolution of down to 1 to 2 mm [17]. While this may be effective for human studies, it is often too imprecise when using small-animal models. The average mouse brain is approximately 9 x 5 x 11 mm in size, and can be sampled only coarsely with PET [18]. MRI has an advantage in that it has the ability to collect data in the submillimeter range. A single unit of volumetric space (voxel) used for mouse MRI is typically about 100 x 100 x 500 µm [19]. Furthermore PET imaging has a temporal resolution of tens of seconds to minutes while MRI is able to collect images on the orders of milliseconds to seconds. Thus, MRI has an edge in providing the spatiotemporal characteristics desired for studying neurobiological mechanisms.

1.3 Magnetic resonance imaging (MRI) and MRI probe development

MRI can measure numerous properties of living tissue, but a dominant application in neuroscience is the use of functional MRI (fMRI) to image neural activity patterns in the living brain. Typically, fMRI records increases in neural activity by tracking changes in blood flow, a concept known as hemodynamics [20]. While many types of hemodynamic contrast exist, the most used is a method known as blood oxygen level–dependent (BOLD) imaging. When a portion of the brain becomes metabolically active, an increase in blood flow will induce oxygenation of the paramagnetic hemoglobin circulating in that region. This produces a detectable alteration in an MRI signaling parameter known as T_2* [21]. MRI signal parameters describe changes in nuclear spins, and T_2* relaxivity represents the dephasing of nuclear spins in the plan transverse from equilibrium due to adjacent spin-spin interactions (T_2), as well as additional inhomogeneities due to the magnetic field stability. This is in contrast to the parameter T_1 relaxivity which captures longitudinal magnetization back to equilibrium following a radio frequency (RF) perturbation [22]. While this technique

has been broadly explored in the literature, a common issue underlies many of the findings – the precise molecular changes inducing particular blood oxygen changes are unknown. The process of neuronal induced changes in blood flow, known as neurovascular coupling, is thought to be influenced by a number of signaling pathways. This includes the action of neuronally-derived substances such as nitric oxide (NO) and glutamate [23]. Distinguishing individual molecular or cellular components of neural function is impossible using conventional fMRI methods, however.

Instead, we must use MRI-responsive sensors specific to our analyte of interest. Previous work from our lab has led to a suite of these MRI probes (Figure 2). This includes engineered proteins with iron-containing heme domains that shift T_1 relaxivity following binding to dopamine and serotonin [24, 25]. Other approaches have conjugated iron nanoparticles to analyte-responsive proteins and small molecules [26, 27]. An alternative class of sensors takes advantage of metalloporphyrins that are cleaved in the presence of an enyzyme of interest [28, 29]. Most of these probes have been applied locally in single brain regions. However, when we attempt to apply these sensors to the whole brain, we are met with the blood-brain barrier.

1.4 Confronting the blood-brain barrier

In 1885, Paul Ehlrich reported that intravenous injection of various dyes lead to staining in almost all animal tissue except the brain and spinal cord [30, 31]. However, the explanation for this phenomena was widely debated for decades. It was not until 1967 in which electron microscopy revealed that horseradish peroxidase (HRP) was trapped in the lumen of the CNS endothelium. Complexes of tight junctions joined the endothelial cells and formed a contiguous, largely impenetrable endothelium [32]. We now refer to this selectively permeable structure of tightly connected endothelium as the blood-brain barrier (BBB). Unlike cellular junctions in other organs of the body, the brain's blood-brain barrier is more selective typically only passing small, lipophilic molecules [33]. This selectivity of the BBB poses is-

sues in transporting exogenous molecular into brain parenchyma. By some accounts only 5% of small-molecule therapeutics effectively cross the BBB on their own [34]. However, exceptions exist thanks to natural mechanisms of transport. This includes passive diffusion of lipophilic molecules include ion channels, passage of bioessential polar molecules via carrier-mediated transport, receptor-mediated transporters, and adsorption-mediated transcytosis (Figure 3) [35].

To surpass the blood-brain barrier is to physically bypass a brain-body distinction. We need to imagine how to apply diagnostics and therapeutics past this impediment. Molecules can be engineered to hijack or curtail these natural mechanisms. A great way to study how the BBB may be disrupted or bypassed is molecular imaging.

Disruption can be achieved either mechanically or chemically. The mechanical approach of choice is ultrasound-mediated (US) BBB disruption. This is due to its ability reversibly disrupt tight junctions of the BBB with a transducer remaining physically outside the brain tissue. It is an increasingly popular approach currently being implemented in various clinical trials [36, 37]. While ultrasound was first being reported as a means of brain delivery as early as 1956, its first widespread use in human trials began in 2017 [38]. Ultrasound can be applied in a focused or unfocused manner depending on the acoustic wave beam length. Focused US targets precise regions of interest while unfocused US spans larger tissue volumes [39]. Besides mechanical disruption, one can also imagine chemical disruption. One such approach is to induce osmolarity. This is done by introducing hypertonic solutions that shrink endothelial cells to subsequently break tight junctions. This has been exhibited with formulations of arabinose, mannitol, saline, and urea among others [40]. However variable outcomes has lead to limited clinical usage [41].

Another approach is to ignore the vasculature altogether and infuse agents through the cerebrospinal fluid (CSF). This approach is being used clinically for chemotherapy and pain management [42, 43]. Given the ability to access CSF, one may ask why explore delivery via the vasculature in the first place. The first is that accessing the CSF involves invasive catheterization. Improper implantation can lead to CSF

leakage, infection, and depending on where it is accessed, damage to the spinal cord [44]. The second reason to consider vasculature is the comparatively limited physical access CSF delivery affords. In humans, the mean percentage of total ventricle volume within total brain volume has been cited as 2% while the cerebral blood volume is thought to be closer to 4.25% [45, 46]. A larger portion of brain volume is dedicated to the vasculature system. While the density of the ventricles is highly localized , every neuron is within 15 um of a blood vessel [47]. Thus, both CSF (for its relative ease of access) and intravasculature delivery (for the promiscuity of blood vessels in the brain) are attractive options in surpassing the BBB. A quantitative comparison of methods surpassing the BBB is presented in Chapter 2.

1.5 Widefield application of an MRI probe for investigating the cholinergic system

In Chapter 3 of this thesis we describe the application of a CSF delivery technique in a proof-of-concept study of a new molecular imaging probe designed to study the biology of acetylcholine, a neurotransmitter at the heart of brain-body interactions. Acetylcholine (Ach) was the first discovered neurotransmitter and is present in both the peripheral and central nervous system [48]. Its transmission is terminated at the synaptic cleft by cholinesterase, a serine hydrolase [49]. One direct way Ach modulates brain-body physiology is by modulating the vagal nerve, a physically connection from the brain stem to branches of nerves in visceral organs [50]. Additionally, Ach circulating in the blood is introduced into the brain parenchyma via specialized choline transporters in the blood-brain barrier [51].

Regulation of homeostatic brain-to-body ACh communication diverges in disease [52]. In neurodegenerative diseases such as Alzheimer's, there is a degeneration of cholinergic neurons. Longitudinal studies of the administration of cholinesterase inhibitors have suggested improvement of long-term cognitive decline [53, 54]. In autism spectrum disorder (ASD), cholinergic dysfunction has also been implicated. The structure and size of neurons in the basal forebrain cholinergic nucleus of young chil-

dren with ASD is abnormal [55]. There is also a reported reduction of M1 type muscarinic-cholinergic receptors (mAChR) in the cortex, cerebellum, thalamus, and striatum in the post-mortem tissue of humans with ASD [56]. As in Alzheimer's, administration of cholinesterase inhibitors have been explored as an avenue of treatment for ASD. Systemic administration of the acetylcholineesterase inhibitor, Donepezil, was shown to mitigate cognitive and social deficiency in mouse models of autism [57].

The literature reveals that much of our understanding of cholinergic functions has been explored in post-mortem tissue or through indirect behavioral and cognitive measurements. To better understand these dynamics in living tissue, molecular imaging probes of cholinergic function serves as an attractive route of investigation.

1.6 A molecular systems approach for studying the neurobiology of substance abuse

Ultimately, our aim is to apply an integrated view of the brain and body to investigate brain states and behavior. An application space that is commonly ridden with a dualist view is substance abuse. The brain is seen as the locus of addiction whereas in fact, brain-body interactions lie at its core. Thus, the neurobiology of opioid dependence serves as a valuable application space for the molecular imaging approaches developed in Chapter 2 and 3.

Opioid use disorder (OUD) is a chronic disorder that is initiated by hedonic effects. This transitions into negative consequences of withdrawal following long-term abuse [58]. On a molecular level, it is known that opioids bind to endogenous opioid receptors in both the central and peripheral nervous system. This includes mu (μ), kappa (κ), and delta (δ) receptors [59]. In particular, the activation of μ-opioid receptors (endorphins) produces rewarding analgesic and euphoric effects [60]. A hallmark of the disorder is that long-term exposure to opioids induces tolerance, meaning more opioid is needed to produce the same level of reward [58]. To understand the disorder, a heavy amount of focus has been placed on observing changes in the brain following

intoxication. Following opioid exposure, altered hemodynamic response and transcriptional activity is observed in the regions of the canonical dopaminergic pathway, namely the ventral tegmental area and nucleus accumbens [61, 62]. After long term abuse, withdrawal from opioids induces negative affect and physical symptoms such as piloerection, chills, insomnia, gastrointestinal distress, and aches [63]. Mitigating adverse effects plays a role in this cycle of addictive behavior.

Fundamentally, the abuse of opioids manifests beyond the brain. The rewarding experience of intoxication is paired to peripheral analgesia, and severe, adverse somatic symptoms plague chronic users experiencing withdrawal. To understand the brain-body connection in this space, we designed a study to investigate the insula, a cortical mediator of physiological signals from the body [64]. We hypothesized that (1) in opioid abuse, the insula mediates striatal connectivity in canonical reward pathways and (2) the insular cortex mediates physiological symptoms of withdrawal following chronic opioid use. To test our first hypothesis, we implemented a molecular tool previously developed in the lab, Paramus [65]. This is a paramagnetic conjugate of the $GABA_A$ agonist muscimol. Its delivery allows us for the simultaneous reduction of neuronal excitability while visualizing the agent's spread. Acute fentanyl exposure was performed in the MRI with and without a Paramus infusion to the insular cortex. The resultant impact on striatal network connectivty was examined. Additionally, we used a genetically encodable probe in conjunction with functional MRI to examine insular modulation of the withdrawal state. Designer Receptors Activated Only by Designer Drug (DREADDs) are receptors activated by small molecule chemical actuators [66]. Using an inhibitory version of the DREADD, hM4Di [67], we silenced neuronal activity in the insula during withdrawal. We paired neuroimaging studies with behavioral tests that showed a deviation of peripheral, somatic symptoms following insular inhibition. Ultimately this pairing of neuroimaging and behavior illustrate the interplay of brain and body in opioid abuse. This work is outline in Chapter 4 of this thesis.

1.7 Organization of the thesis

This thesis is composed of five chapters. The first is this introduction. Chapter 2 is "Quantitative comparison of methods for wide-field delivery of small molecules across the blood-brain barrier." Here we quantitatively evaluate and compare three strategies for wide-field brain delivery that employ transient BBB disruption or infusion via the cerebrospinal fluid (CSF) in rats. This work directly informed our widefield brain delivery approach used in Chapter 3, "Probing cholinergic activity by MRI." Here we investigate a neurochemical pathway important for motor control mechanisms in both the central and peripheral nervous systems. In Chapter 4, "Investigating interoception in opioid dependence," we apply molecular imaging tools in the context fentanyl abuse. This is a phenomena often attributed solely to the brain, but in truth, brain-body interactions lie at its core. Chapter 5 addresses conclusions and future directions of this work.

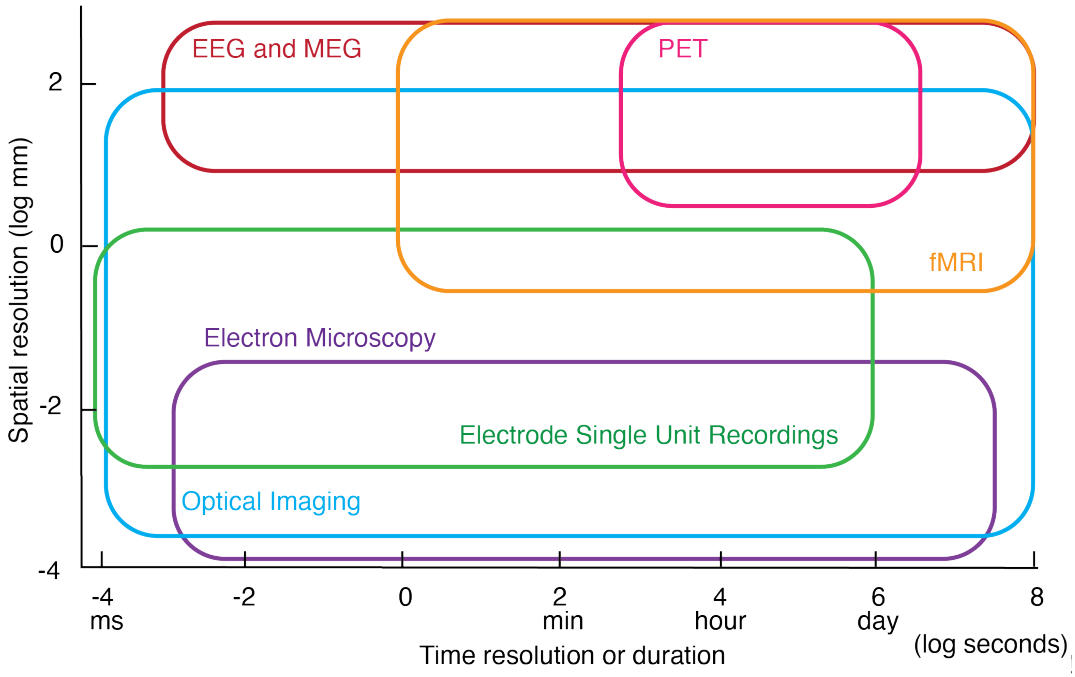

Figure 1.1: **Spatiotemporal resolutions of neuroscience tools.** EEG = electroencephalograhy, fMRI = functional MRI, MEG = magnetoencephalography, PET = positron emission tomography (*adapted from Grinvald and Hildesheim, 2004* [68])

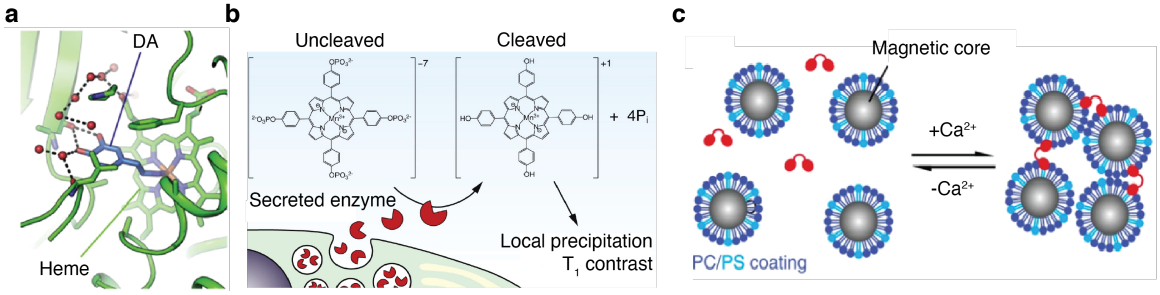

Figure 1.2: **MRI-responsive molecular sensors.**
(a) Enzymatically cleaved metalloporphyrins [29]. (b) Dopamine-binding heme protein [19, 24]. (c) Calcium-responsive magnetic nanoparticles [26].

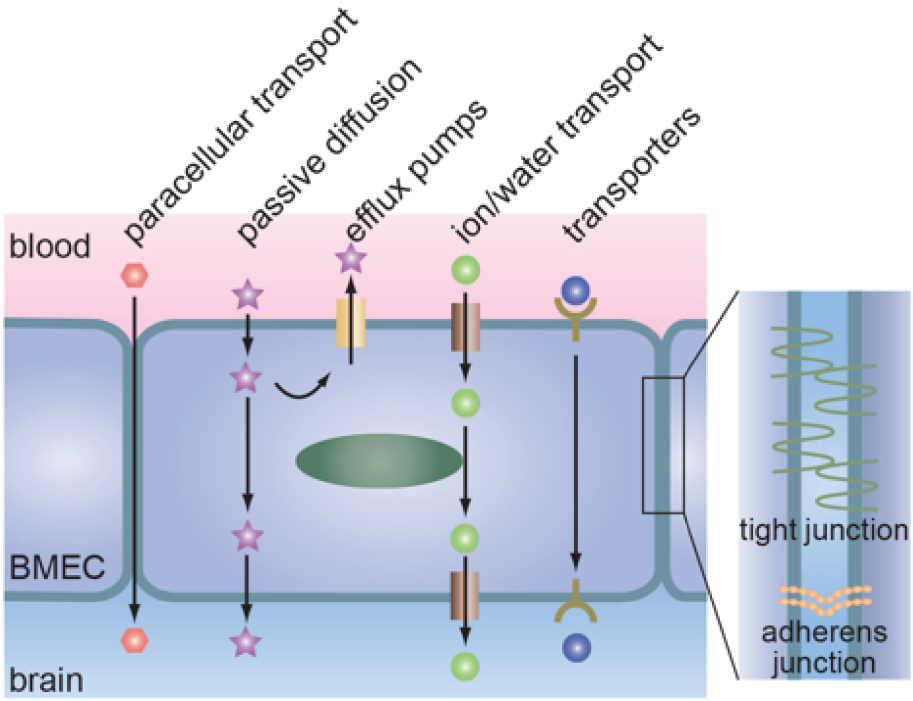

Figure 1.3: **Natural mechanisms of BBB transport.**
From Wong, et. al, 2013 [35].

Chapter 2

Quantitative comparison of methods for wide-field delivery of small molecules across the blood-brain barrier

This work was done in collaboration with Dr. Sarah Bricault and Dr. Pete Harvey.

2.1 Abstract

Delivery of therapeutic and diagnostic agents to the central nervous system is hindered by the blood-brain barrier (BBB), a system of tightly juxtaposed endothelial and perivascular cells that prevents extravasation of most blood-borne molecules. Brain-wide administration of exogenous molecules past the BBB could address many purposes, but achieving systematic delivery remains a challenge. Here we quantitatively evaluate and compare three strategies for wide-field brain delivery that employ transient BBB disruption or infusion via the cerebrospinal fluid (CSF) in rats. Using molecular magnetic resonance imaging (MRI) techniques, we find that the three techniques produce spatially differentiated labeling patterns, with the most homogeneous delivery produced either using chemically mediated or unfocused ultrasound-based BBB manipulation methods. Contrast enhancement distributions are similar following chemical and ultrasound procedures, suggesting that BBB structures in different brain areas display consistent susceptibility to disruption. Regional washout rates apparently track density of blood vessels and tight junction proteins but deviate in the chemically-mediated condition likely due to the density of the endogenous ligand receptor. Our results thus document systematic spatial variation of BBB properties while offering guidance about brain-wide application of molecular technologies in neuroscience and neuromedicine.

2.2 Introduction

The blood-brain barrier (BBB) shields the brain from harmful and useful substances alike [69, 70]. Although the barrier protects effectively against many toxins and infectious agents, it also bars entry to most drugs, complicating the treatment of disorders such as brain cancer, neuroinflammatory conditions, and neurological conditions [71]. By some accounts, only 5% of small-molecule therapeutics effectively cross the BBB on their own [34]. Tools of modern biomedicine, including engineered proteins, nanoparticles, and cells, are even more likely to be hindered because of their larger sizes. Important reagents in basic science, such as chemical actuators, imaging probes, and viral vectors, are also blocked, complicating fundamental investigations of brain biology. In some cases, reagents have been engineered to undergo spontaneous BBB permeation, for instance by conjugating them to substrates of receptor-mediated transcytosis across the BBB [72, 73]. Such strategies require modification of each substance to be administered, however, and still result in relatively inefficient delivery. For other molecules, more active strategies are required to facilitate brain delivery. Discovering and characterizing minimally disruptive ways to bypass the BBB when needed is thus an outstanding challenge in biomedical research.

Several techniques for minimally invasive brain delivery of BBB-impermeant substances have emerged. Infusion of chemicals into the cerebrospinal fluid (CSF) has long been used to bypass the BBB, and studies of CSF flow profiles have shown that infusion into specific fluid reservoirs can enable injected agents to spread throughout much of the brain [74, 75]. Physical disruption of the BBB using low frequency ($\leq$ 2 MHz) transcranial focused ultrasound (US) has been used to permit substances to enter the brain from the vasculature with spatial selectivity, and a small number of studies have shown that unfocused US can also facilitate delivery to large brain areas in small animals [76–79]. Finally, chemically induced BBB disruption techniques have also demonstrated promise for wide-field delivery of various agents from the vasculature. Delivery of small molecules and nanoparticles has been demonstrated using a specific approach in which BBB disruption is promoted by intravenous infusion of

lysophosphatidic acid (LPA), an approach that parallels effects of clinically applied hyperosmotic BBB disruption methods [80–82].

To decide how to choose and use methods for wide-field delivery of small molecules, it is important to understand how these techniques compare under analogous situations. How do CSF delivery or BBB disruption techniques perform under matched conditions in which the same molecule is delivered using each modality? Are there areas of the brain that are accessed preferentially by one delivery method or another? How do kinetics of labeling and washout compare among the methods? Can regional or technique-dependent differences in trans-BBB delivery performance be understood mechanistically? Here we address these questions by combining brain administration methods with noninvasive molecular imaging in rodents. Quantitative comparison of the wide-field delivery techniques using consistent experimental parameters identifies strengths and weaknesses of each technique, indicating approaches that could provide optimal utility for numerous contexts in basic and preclinical neuroscience research.

2.3 Results

2.3.1 Paradigms for wide-field delivery of a small molecule contrast agent

To compare delivery techniques, we assessed the ability of each method to achieve brain-wide distributions of gadoteridol, a small (559 Da), neutral gadolinium complex that causes brightening in longitudinal relaxation time (T_1)-weighted magnetic resonance imaging (MRI) [83]. We measured gadoteridol-induced contrast changes using *in vivo* MRI of Sprague-Dawley rats, following four treatments (Figure 1a,b): (1) intravenous delivery without BBB disruption (a negative control); (2) intravenous delivery in conjunction with wide-field microbubble-assisted US-mediated BBB disruption, using a 2.5 cm-diameter unfocused transducer; (3) intracarotid delivery with chemically mediated BBB disruption using coinfusion of 2 mg/kg LPA; and (4) intra-CSF delivery via infusion into the cisterna magna, a CSF reservoir that has been shown to facilitate brain-wide spread of injected substances. For the peripheral delivery treatments (1-3), a 1 mL dose of 500 mM gadoteridol was injected intravascularly. For the intra-CSF method (4) a 100 µL dose of 25 mM contrast agent was administered, under the supposition that dilution of this amount throughout $\tilde{2}$ mL brain tissue would produce roughly the same final concentration as present in blood after the intravascular injections [84, 85].

MRI results from parasagittal and coronal slices show that all the treatments, except the negative control, produce strong T_1-weighted signal enhancements in the brain, reflective of substantial gadoteridol delivery to representative animals. The bases of these image effects are quantitatively indicated by maps of the longitudinal relaxation rate R_1 ($= 1/T_1$), a physical parameter that determines T_1 contrast and varies linearly with the gadoteridol concentration by previously reported factors of 2.75 $mM^{-1}s^{-1}$ at 7T and 2.64 $mM^{-1}s^{-1}$ at 9.4T [86, 87].

Differences in R_1 over baseline values of about 0.430 ± 0.002 s^{-1} in untreated control rat brains indicate that all three delivery techniques produce widespread effects

corresponding to gadoteridol concentrations of up to ~100 µM (Figure 1c). Changes could be further quantified by examining histograms of R_1 values obtained from multiple animals per condition (Figure 1d). Average relaxation rates measured from control animals were 0.507 ± 0.004 s^{-1} ($n = 4$), whereas values measured from US, and LPA, and CSF animals were 1.033 ± 0.056 s^{-1} ($n = 3$), 1.410 ± 0.187 s^{-1} ($n = 5$), and 1.090 ± 0.093 s^{-1} ($n = 4$), respectively. Most voxels in the three delivery conditions displayed R_1 values more than two standard deviations above the mean R_1 for the control condition: 91.75 ± 0.35% for US, 99.29 ± 0.36% for LPA, and 75.99 ± 8.32% for CSF techniques, respectively. These results indicate that trans-BBB and intra-CSF delivery schemes were all highly effective at spreading gadoteridol over large volumes of brain tissue.

2.3.2 Quantification of spatial aspects of brain delivery

Although each of the three tested methods successfully achieved wide-field brain delivery of gadoteridol, the maps of Figure 1 clearly show that there is spatial heterogeneity of the resulting R_1 enhancements. We sought to characterize this heterogeneity and determine its reproducibility. Mean and standard deviation maps depicting changes in R_1 were obtained from animals subjected to US-mediated, LPA-mediated, and intra-CSF delivery of gadoteridol (Figure 2a). Results indicate that US-mediated delivery accesses tissue fairly homogeneously in a swath of tissue with full-width at half-height of 3.9 mm, likely reflecting the limited pressure field afforded by the transducer; this could be extended by applying multiple sonications ([77], Supplementary Figure 1). LPA-assisted delivery produces more homogeneous delivery along the rostrocaudal axis, but with a left-right asymmetry resulting from unilateral infusion through the carotid artery (Supplementary Figure 2). Additionally, delivering LPA via the tail vein shows contrast agent enhancement, but less enhancement than via the carotid artery route (Supplementary Figure 3). Intra-CSF delivery is less homogeneous, tending to reach ventral areas and regions close to the ventricles and cisterns for which the partial volume of CSF might be high [75]. In our hands, the most reproducible results were obtained using the US technique, as indicated by the low standard deviations of R_1

throughout the sagittal section analyzed. Although LPA results were less reproducible, normalization of contrast changes by the whole brain signals after LPA-mediated delivery narrowed the distribution of ROI results (Supplementary Figure 4), suggesting that relative susceptibility of ROIs to chemical disruption was largely conserved across animals.

To form a more systematic impression of delivery efficacy to different brain areas, we analyzed gadoteridol-mediated R_1 enhancements over regions of interest (ROIs) based on a standard brain atlas (Figure 2b). Mean changes in R_1 from baseline (R_1 values) varied by as much as four-fold over the different ROIs (Figure 2c). The hypothalamus and ventral striatum experienced effective delivery using all three techniques, whereas the cerebellum was poorly accessed in each case. Quantitative comparison of ROI-level delivery results (Figure 2d,e) showed very close correspondence between average R_1 values obtained using the US and LPA techniques (Pearson's correlation coefficient, CC = 0.97, p = 6.35E-7, n = 10 ROIs), but much looser correspondence between intra-CSF infusion and LPA-mediated delivery (CC = -0.16, p = 0.64). The comparison between CSF infusion and US-mediated delivery (Supplementary Figure 5) was similarly weak (CC = -0.16 p = 0.63).

2.3.3 Kinetic analysis of contrast agent dynamics after delivery

Contrast changes induced by US-mediated, LPA-assisted, and CSF infusion-based gadoteridol delivery using the procedures of Figure 1 were measured over a period of 100-200 minutes following each procedure, raising the possibility of comparing the dynamics of molecular delivery using each approach. We examined the R_1 time series results to determine whether information could be obtained in this way. Despite stark differences in the nature and timing of the three delivery protocols, all three methods resulted in brain-wide MRI signal increases that peaked on the order of an hour after the delivery treatment (Figure 3a). Similar temporal profiles were observed within individual ROIs as well (Supplementary Figure 6). Mean times to peak were 30.67 ± 8.67 min for US, 30.60 ± 5.27 min for LPA, and 65.6 ± 4.29 min for CSF delivery (Figure 3b), indicating that gadoteridol continued to enter the brain or spread from

initial sites of entry for many minutes following each procedure.

To analyze this process more precisely, we fit the time series at each voxel to a linear two-compartment kinetic model in which all sources of out-of-voxel gadoteridol were lumped into one compartment and the within-voxel contrast was represented by the second compartment (Supplementary Figure 7). The time course of relaxivity change predicted in this scenario is given by:

$$q_2(t) = \frac{AK_1}{k_{out} - k_{in}}(e^{k_{in}t} - e^{k_{out}t}) \quad \text{(Eq.1)}$$

where the rate constant k_{in} describes influx of agent into a voxel, k_{out} describes efflux, and c is a scaling constant. Data from each voxel exhibiting substantial R_1 changes were fit to Eq. 1, yielding parameter estimates from 94.82 ± 0.86%, 90.38 ± 1.94%, and 55.09 ± 10.73% voxels across 3-5 animals in the US, LPA, and CSF delivery conditions, respectively (Figure 3c). Average fitted values of k_{out} and k_{in} are diagrammed in Figure 3d and Supplementary Figure 8.

Values of k_{out} in particular reflect dissipation of contrast agent after each delivery procedure is largely completed, so we surmised that these rate constants might reflect consistent properties of small molecule transport in the brain. Indeed, mean k_{out} values do fall in a relatively uniform range, with brain-wide averages of 0.0077 ± 0.00010 s^{-1} for US, 0.0102 ± 0.00009 s^{-1} for LPA, and 0.0087 ± 0.00013 s^{-1} for CSF delivery data (Figure 3e). MRI signal decreases were significantly slower following US versus LPA delivery in deep brain areas including the ventral striatum and hypothalamus (t-test $p = 0.0165$ and 0.009, $n = 2$ US, 4 LPA). This is reflected in the lack of significant correlation between the LPA and US as well as the LPA and CSF k_{out} values (CC=0.0125, p=0.9727, CC=.5503, p=0.0993, Supplementary Figure 9). However, the k_{out} values for US and CSF delivery were significantly correlated (CC=0.774 and p=0.0086, Figure 3f).

2.3.4 Molecular correlates of brain delivery and washout

The close correspondence of trans-BBB delivery profiles achieved following US and LPA treatments led us to wonder whether specific tissue properties could account for the observed contrast distributions. We speculated that determinants could include the density of blood vessels, from which contrast agent enters the tissue in the presence of a compromised BBB, and the prevalence of tight junctions that promote BBB integrity and are disrupted by US or LPA [88, 89]. To examine the importance of these factors, we used immunohistochemistry to label markers of vascular endothelial cells (tomato lectin), tight junction protein Claudin-5, and the LPA receptor across sagittal brain slices approximately matched to the MRI geometry of Figs. 1-3 (Figure 4a,b Supplementary Figure 10). Both markers stained with varying intensities across the field of view and could be quantified in maps and ROIs similar to those used to characterize contrast agent delivery parameters measured by MRI.

The staining results indicate that some of the regions that experienced the greatest k_{out} were the most densely vascularized. Reflecting this, the spatial correlation between contrast agent clearance by the US-mediated method and vascular histology measures was and 0.734 (p =0.0383) for tomato lectin staining and 0.729 (p =0.0400) for Claudin-5 staining (Figure 4c,d, Supplementary Table 1). Given the deep brain regions (ventral striatum and hypothalamus) were already implicated as having divergent profiles of clearance in the LPA condition, we expected these regions to remain as outliers. This was indeed the case (CC=0.201 and p=0.578 for lectin, CC=-0.3766 and p=0.283 for Claudin-5) with significant correlation only occurring in the absence of these regions (CC=0.979 and p=8.23x10^{-7} for lectin, CC=0.9971 and p=1.19x10^{-6} for Claudin-5). In CSF delivery, the spatial correlations between k_{out} values and histology measures (CC=0.741 and p=0.086 for lectin, CC=0.788 and p=0.007 for Claudin-5) indicated these trends persist independent of whether the initial delivery was vascular. These findings thus suggest that tissue parameters, rather than biophysical properties of the delivery methods themselves, largely determine the efficacy of wide-field trains-BBB delivery of small molecules to the brain.

2.4 Discussion

Achieving wide-field delivery of chemicals to the brain remains a formidable challenge for applications in biotechnology and biomedicine. Here we have used molecular MRI to assess performance of three wide-field delivery techniques that each enable the exogenous contrast agent gadoteridol to reach broad regions of brain tissue in rodents. We found that US- and LPA-mediated BBB disruption promote variegated but spatially similar profiles of delivery throughout cortical and subcortical areas. Conversely, CSF infusion via the cisterna magna produced less homogeneous distributions that were more pronounced around CSF reservoirs and ventral brain regions, consistent with previous reports [75, 90]. Analysis of MRI time courses following delivery showed that contrast changes peak about an hour after treatment with each method, and that average washout rate constants of order 0.01 s^{-1} are observed for all brain regions following each delivery approach. Some of our spatial results appeared to reflect the distribution of markers in brain vasculature, emphasizing the interaction of delivery parameters with physiological characteristics of the brain itself.

Each of the brain delivery methods we evaluated displayed pros and cons with respect to the others. The US technique produced widespread and relatively stable contrast enhancement (k_{out} values twofold lower than for LPA). Although it required specialized equipment and coinjection of microbubbles, results obtained with this approach were quite reproducible [91]. Even using the 2.5 cm-diameter flat transducer we applied, the US technique could not produce uniform brain labeling, but we found that application of US treatment at four isocenters could address this limitation. The LPA-mediated delivery method was the easiest to implement in our hands. Although the technique as we applied it involved preimplantation with a carotid catheter, subsequent delivery results could be readily obtained following just a single acute injection via the catheter. Intra-CSF delivery was the most invasive procedure and the least effective in reaching multiple brain areas, but it uses less of the injected substance and does not impinge on peripheral tissues and organs. A combination of these methods might be most effective at delivering substances everywhere in the brain. In particular,

the CSF method we used was adept at accessing caudal and ventral structures that the US and LPA methods addressed less successfully.

A limitation of our analysis is the fact that we had to make arbitrary choices about the way we implemented each of the delivery methods. This involved choosing timing, injection routes, concentrations, and other parameters for all techniques, plus apparatus for the US method. In addition, we performed all delivery experiments in rats, using a single molecule—the hydrophilic but neutral MRI contrast agent gadoteridol—as a delivery substrate. Each of the methods we used is likely to scale differently for brains and species of different size, with brain-wide distributions more difficult to achieve for larger brains due to transport issues, among other factors. Larger or more hydrophobic molecules will also be more difficult to deliver. Previous studies have shown that trans-BBB delivery of large agents results in much more restricted spread from vascular compartments [92, 93]; the same consideration applies to spreading from the perivascular Virchow-Robin space following intra-CSF injection [94].

Two of our findings are likely to hold despite these concerns, however: First, the complementary characteristics of intra-CSF and trans-BBB molecular delivery profiles follow neuroanatomical features that are conserved across mammalian species and naturally independent of the delivered molecule. Complementarity of CSF and trans-BBB delivery profiles is therefore likely to persist across species and substrates. Second, spatial similarities we have documented between wide-field US and LPA trans-BBB delivery distributions, which arise from different mechanisms but also parallel vascular markers, suggest that specifics of how the protocols are implemented are less important than tissue parameters in determining spatial contours of the delivery results. This conclusion may apply to brain delivery methods untested in our experiments, such as techniques that employ osmotic shock or perhaps even receptor-mediated transport pathways [73, 82]. The comparative study we present here may thus offer both a guide to applying the specific brain delivery techniques we assessed and a basis for anticipating results of delivery approaches that are yet to be investigated.

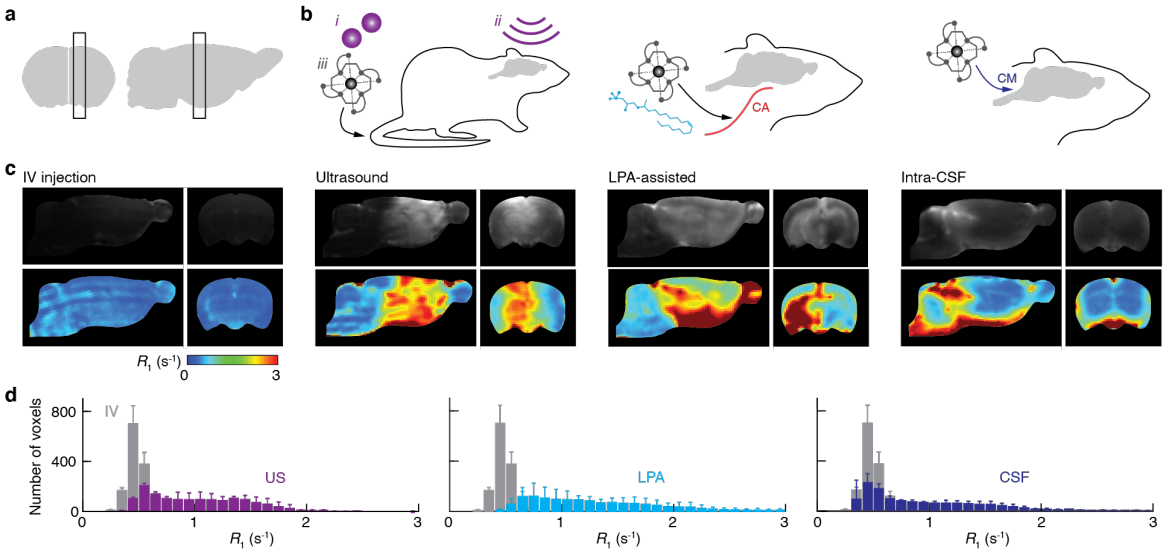

Figure 2.1: **Methods of wide-field delivery.**
(a) Diagram showing the placement of the sagittal slice (2 mm from midline) and coronal slice (5 mm behind the olfactory bulb). (b) Schematics showing ultrasound (US), LPA-assissted, and intra-CSF delivery of the contrast agent. (c) Representative T_1-weighted images and R_1 maps showing distribution of contrast agent 20 minutes post-injection. (d) Histograms displaying the distribution of voxels following each delivery techinique as compared to the intravenous negative control.

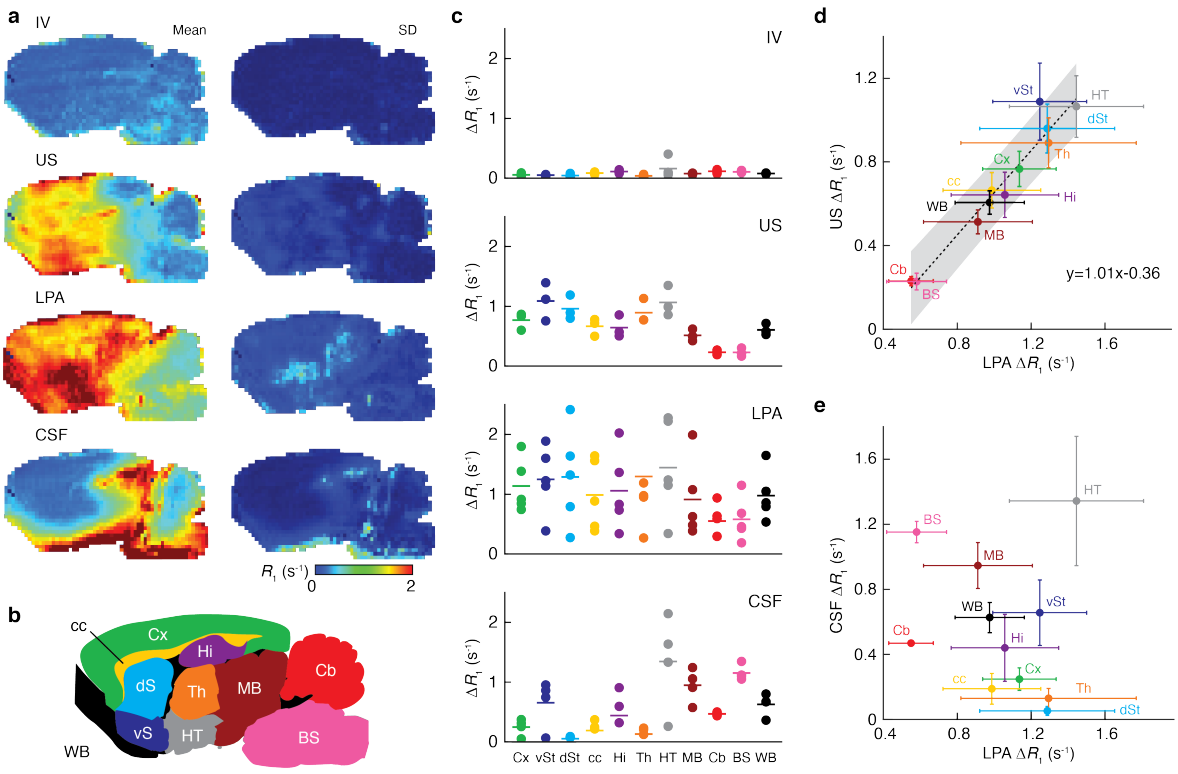

Figure 2.2: **Spatial aspects of brain delivery.**
(a) Mean and standard deviation of R_1 following contrast agent delivery. (b) Atlas with relevant regions of interest. (c) ΔR_1 for each technique by ROI. (d) Correlation between LPA and US ΔR_1 across ROIs along with their linear fit. Gray represents the 95% confidence interval for the linear fit. (e) Correlation between LPA and CSF ΔR_1 across ROIs.

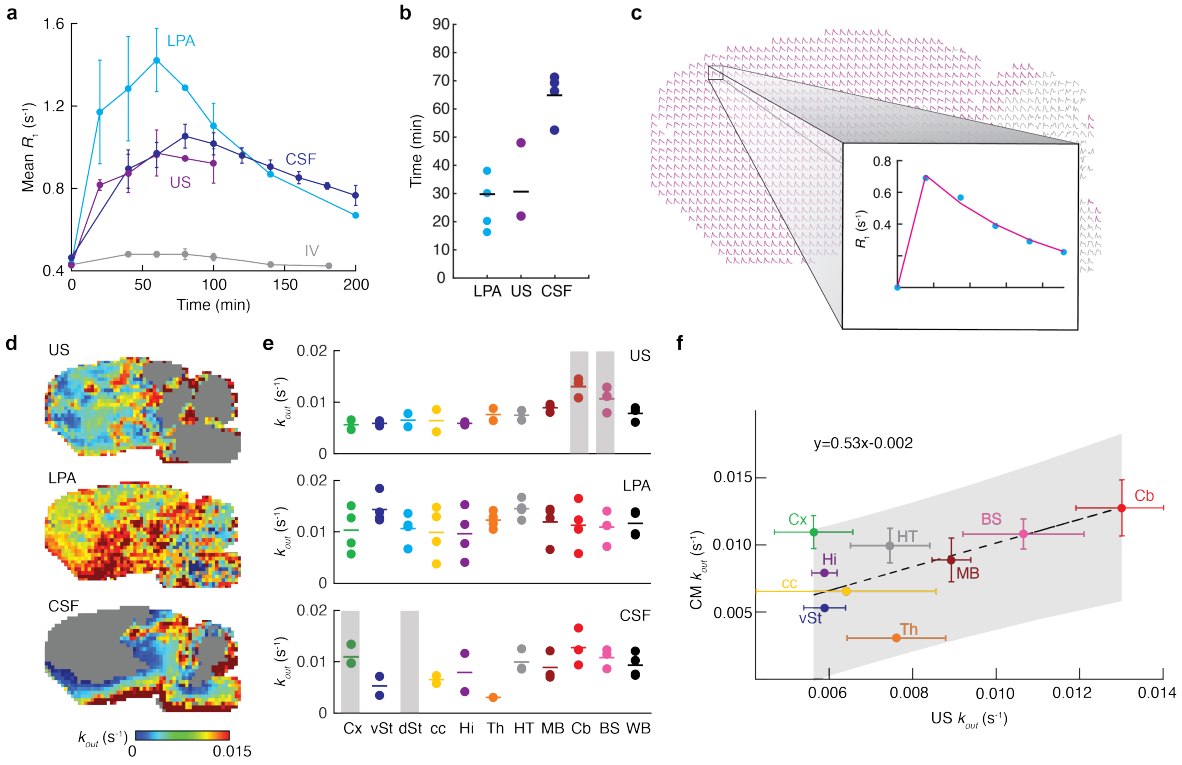

Figure 2.3: **Kinetics of contrast agent delivery.**
(a) Time course of mean R_1 post-injection. (b) Time to peak whole brain contrast agent enhancement for each method. (c) Representative voxel fit to the kinetic model. (d) Average k_{out} in each condition. (e) ROI-level values of k_{out}. Shaded regions represent regions with less than 50% of voxels achieving a fit to the kinetic model. (f) Correlation of US and CM k_{out} values.

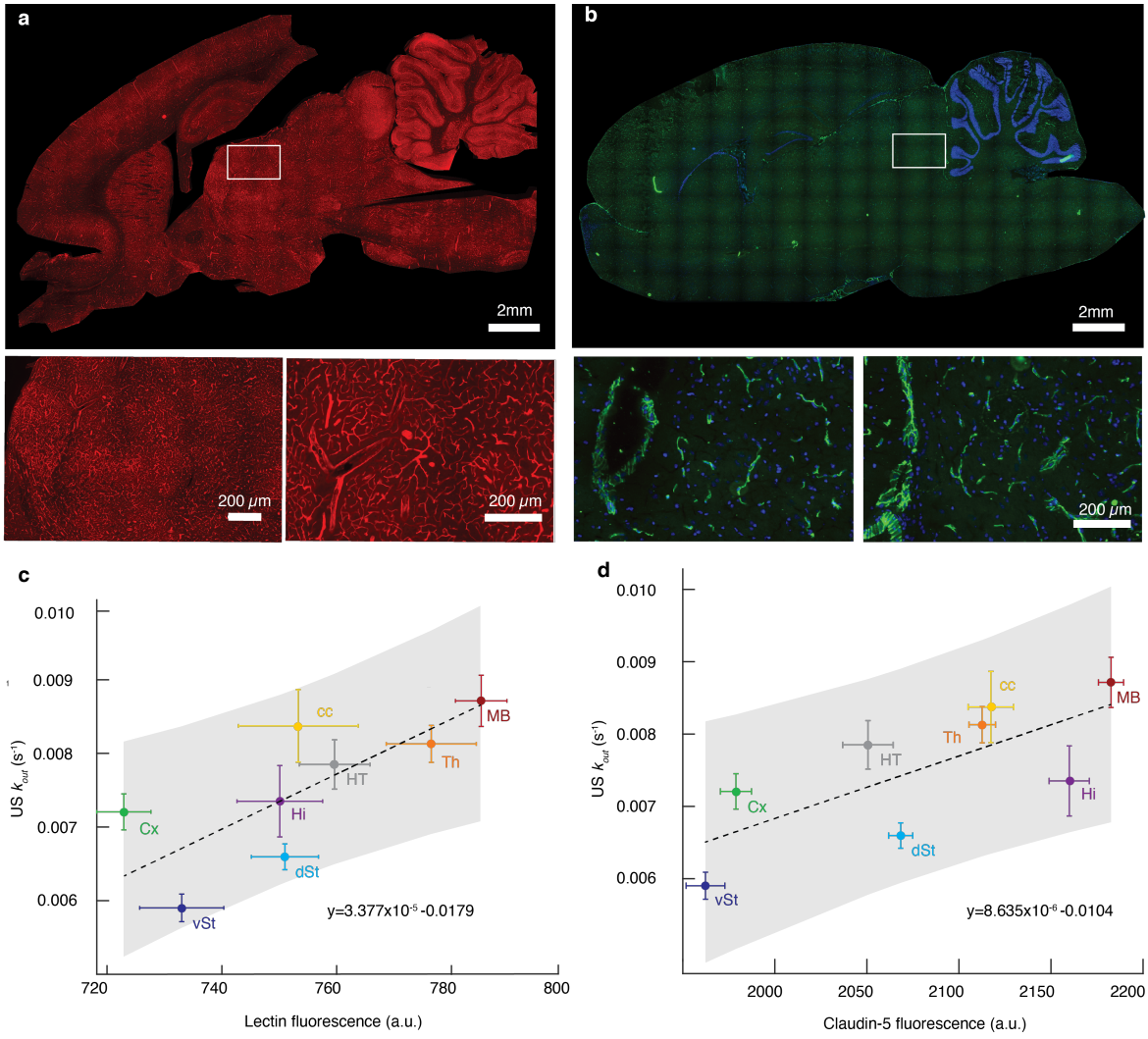

Figure 2.4: **Molecular correlates of brain delivery.**
(a) Lectin staining in a parasagittal brain slice. (b) Claudin-5 staining. (c) Correlation of k_{out} and lectin fluorescence. (d) Correlation of k_{out} and lectin fluorescence.

2.5 Materials and Methods

Animals

All animal procedures were performed in strict compliance with US Federal guidelines, with oversight by the MIT Committee on Animal Care. Male Sprague-Dawley rats (150-300g) were purchased from Charles River Laboratories (Wilmington, MA) and used for the *in vivo* data presented in this paper. Animals procured for LPA-mediated delivery or control IV injection experiments were pre-implanted with chronic carotid artery catheters targeting the left side of the brain. All animals were housed and maintained on a 12h light/dark cycle with ad libitum access to food and water.

Chemicals

All chemicals were obtained from MilliporeSigma (Burlington, MA) unless otherwise noted. Gadoteridol contrast agent formulations used for all brain delivery experiments were obtained from Bracco (Milan, Italy). Optison microbubbles used in US-mediated delivery experiments were obtained from GE Healthcare (Chicago, IL).

US-mediated brain delivery

Six rats were used for US-mediated brain delivery experiments. Animals were anesthetized with 2% isoflurane and then underwent the placement of the tail vein catheter for microbubble injection and contrast agent delivery. The tail vein was visualized by application of alcohol to the skin, and a catheter (24G Surflo, Terumo, Somerset, NJ) was slowly inserted into the vein until obvious blood back-flow was observed. The catheter was secured to the tail by placing a tongue depressor (Puritan, Guilford, ME) underneath the tail and taping the tail and the tongue depressor together using surgical tape. The catheter was flushed with 0.5% heparin in phosphate buffered saline (PBS) to prevent clotting and secured with a stopper prior to contrast agent infusion.

Animals subsequently underwent ultrasound-mediated BBB disruption. The rats were maintained under 2% isoflurane anesthesia. Heads were shaved and cleaned with alcohol and povidone-iodine prep pads for easy access to the skull. The skin over the

skull was retracted and the skull cleaned to visualize the coronal and sagittal sutures. Ultrasound transmission gel (Parker Aquasonic, Fairfield, NJ) was applied to the exposed skull. An ultrasound transducer housing was then positioned in contact with the gel, with its center 1 mm above the skull, 2 mm lateral and 3 mm posterior to bregma. The housing was filled with circulating degassed and deionized water and was affixed to a custom transducer with 25 mm diameter and 500 kHz peak operating frequency (Sonic Concepts, Bothwell, WA). Ultrasound waveforms were generated using a 25 MHz function generator (BK Precision, Yorba Linda, CA) using the following settings: 500 kHz driving frequency, 0.2 V amplitude, 5,000 burst count, and 1s burst rate. Waveforms were amplified using an ENI model 550L radiofrequency power amplifier (Bell Electronics, Renton, WA) conditioned through an impedance matching network (Sonic Concepts) connected to the transducer itself.

Sonication was applied to each animal for 5 min. Immediately after the sonication was initiated, 50 µL of Optison microbubble ultrasound contrast agent (GE Healthcare, Chicago, IL) was injected through the tail vein catheter and flushed with 0.2 mL of 0.5% heparin in PBS. After sonication was completed, the skin was glued together using tissue glue and the animal was immediately transferred to the MRI scanner for imaging.

LPA-mediated brain delivery

LPA-mediated delivery procedures were applied to five rats. Animals were pre-implanted with chronic carotid artery catheters targeting the left side of the brain. Each rat was anesthetized with 3% isoflurane and its catheter clip was removed. Catheter patency was verified and animals no backflow were excluded. The catheter was then connected to an injection line and the animal was moved to the scanner. Isoflurane was reduced to 1.5%, a level that was maintained for the duration of the experiment. Respiration, heart rate, and blood oxygen saturation were monitored, and temperature was maintained with a circulating warm water pad (Gaymar, Orchard Park, NY) for the remainder of the procedure. Animals were imaged before and after a 1 mL carotid artery injection of 2 mg/mL LPA plus 500 mM gadoteridol or 500 mM Gd alone,

delivered over approximately 17 sec in each case. The imaging continued after the injection for 1-3 hours. A subset of these animals were briefly recovered following the procedure, and demonstrated normal behaviors.

Intra-CSF injection

Intra-CSF delivery procedures were applied to four rats. A 1-mm incision was made on the atlanto-occipital membrane between the skull and C1 vertebrae to gain access to the cisterna magna. The incision was washed four times with sterile Gibco DPBS 1X (Thermo Fischer, Waltham, MA) to remove excess blood and CSF. A 28G plastic injection cannula (PlasticsOne, Roanoke, VA) was implanted through the incision and secured by tissue glue. A remote infuse/withdraw dual syringe pump was used to infuse gadoteridol solution (25 mM) at a rate of 5 µL/min for 20 min at a depth of 1mm. Upon the completion of infusion, the cannula was left in place for an additional 5 min before removal. The incision was closed using tissue glue and tissue cement. Animals were then transferred to a holder and placed in an MRI scanner for imaging.

Magnetic resonance imaging

Rats were imaged before and after procedures conducted outside the scanner. All animals were imaged using 7 T (CSF) or 9.4T (LPA and US) Biospec MRI scanners (Bruker, Ettlingen, Germany) scanner operating with birdcage transmit and surface receive coils. T_1 and T_2 mapping data were acquired using a RAREVTR (rapid acquisition with relaxation enhancement with variable repetition time) scan with TR values of 5000, 3000, 1500, 1000, 500, 250, 150, and 120 msand TE values of 10, 30, 50, 70, and 90ms in both the coronal and sagittal planes. A single slice was acquired for each scan sequence, with slice thickness of 1 mm, flip angle of 180°, RARE factor of 2, FOV of 5 x 2.5 cm (sagittal) or 2.5 x 2.5 cm (coronal), and matrix sizes of 150 x 75 (sagittal) or 75 x 75 (coronal). The coronal slice was positioned 5 mm posterior to the dip in the olfactory bulb, and sagittal slices were positioned 2 mm lateral to the midline on both left and right. Throughout imaging, data acquisition alternated between these three map scans (coronal, sagittal left, and sagittal right).

MRI data analysis

All analysis was performed in MATLAB (Wolfram) using custom scripts. To convert raw T_1-weighted MRI data to R_1 maps, the raw signal intensities at different TR values for each voxel were fit to the exponential $a*e^{-x*c}$ where x is the measured signal at different TR values, a is a constant parameter, and c is the R_1 value for that voxel. Voxels for which R_1 values could not be obtained from this procedure, or for which fitted R_1 values were excessively high (> 5 s^{-1}) were excluded from further analysis.

To convert raw MRI data to R_2 signal maps, the raw values at different TE values for each voxel were fit to the exponential $a*(1-e^{-x*c})$, where x was the signal at different TE values, a was a constant fit parameter, and c was equal to $1/T_2$ and was the R_2 value for the voxel. Voxels with an R_2 value that exceeded 80, or for which the exponential failed to find a fit, were excluded from analysis as they represented poor quality data (usually poor signal to noise).

Further analysis was performed using R_1 maps obtained by the procedure described above. Reported R_1 histograms were computed for left sagittal slices, ipsilateral to BBB disruptions created by US and LPA techniques. ROIs were defined from a custom atlas adapted from the 7^{th} edition Paxinos rat brain atlas. R_1 maps were scaled and fit to the atlas Delta R_1 values were obtained by subtracting post-injection maps from the maps obtained pre-injection.

To obtain the average time courses, maps from each treatment group were binned into 20 minute intervals, and the mean R_1 for an ROI of interest was computed for each time period. To compute the kinetic parameters k_{in} and k_{out}, individual voxels were using non-linear least squares in the MATLAB curve fitting toolbox. Only fits with an R^2 above 0.8 were accepted. After curve fitting, average k_{in} and k_{out} for ROIs were computed if greater than half of the voxels in that region had a successful curve fit. Linear correlation was assessed with the Pearson correlation coefficient. Statistical tests used in this study are noted throughout the paper, and error bars and error margins reflect SEM over animals, unless otherwise specified.

Histology procedures

Lycopersicon Esculentum (Tomato) Lectin (LEL, TL), Texas Red from Vector Laboratories was given to four rats approximately 300g each. Each rat was anesthetized with 3% isoflurane for five minutes before being transferred to 1.5% isoflurane. A tail vein catheter (24G Surflo, Terumo, Somerset, NJ) was slowly inserted into the vein until obvious blood back-flow was observed. For one rat, 1 mL of tomato lectin was administered. For the other three, 300 uL was administered. After lectin administration, rats were given 5 minutes before transcardial perfusion with PBS.

Following perfusion with PBS, the brain tissue was extracted and flash frozen in an isopentane and liquid nitrogen bath for approximately 30 seconds. Brains were transferred to a container pre-chilled on dry ice and then stored at -80C. For fixation, tissue was then embedded in OCT compound inside a cryomold and stored at -80C. All were parasagittally sectioned at a cryostat to 14 um thickness.

Antibody staining was performed on the brains from the three 300 uL lectin infused rats. Sections approximately 2 mm from midline were selected. Overnight incubation with primary antibodies was performed at 4C (1:100 dilution, 33-9100 or 35-2500, Invitrogen). This was followed by 2 hours of secondary incubation (1:500, A28175, Invitrogen) and 10 minutes incubation with 1:2000 Hoechst nuclei stain at room temperature.

The stained brain sections were mounted on glass slides with Invitrogen ProLong Gold Antifade (Fisher Scientific Company) and protected with a coverslip. Fluorescence imaging was performed using a confocal microscope (Axio Imager 2, Zeiss)

Histology data analysis

Fluorescence images of parasagittal brain slices were imported into MATLAB and down-sampled to match the resolution of the MRI data before alignment to the atlas. To calculate the correlation of histological markers with kinetic paramters, ROIs with more than 50% of voxels possessing a valid k_{out} fits were assessed.

2.6 Supplementary Information

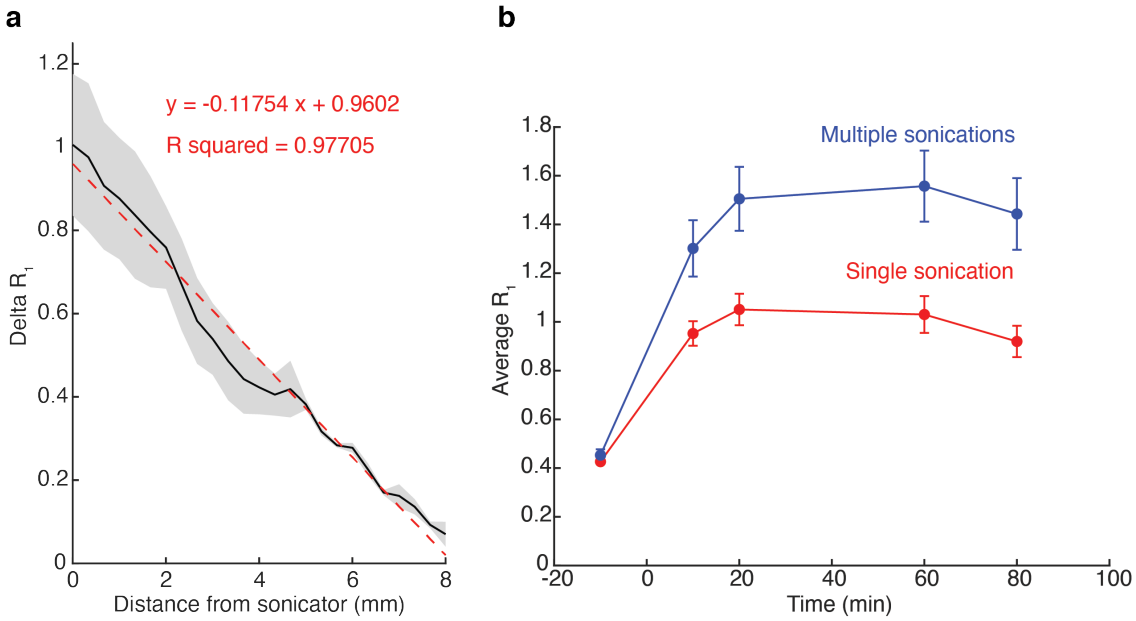

Figure S1: The impact of ultrasound sonication on delivery across the BBB. (a) ΔR_1 as a parameter of distance from the ultrasound sonicator. (b) The whole brain average ΔR_1 for rats receiving a single sonication (n=3) or multiple sonications (n=3).

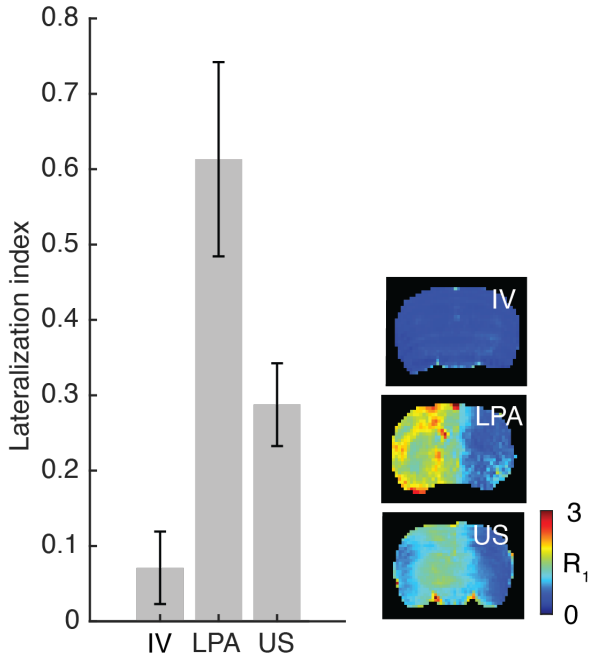

Figure S2: The lateralization of contrast agent delivery.
The heavy lateralization of the LPA rats reflect the route of delivery through a left carotid catheter. Ultrasound rats have more delivery on the side of the sonicator placement.

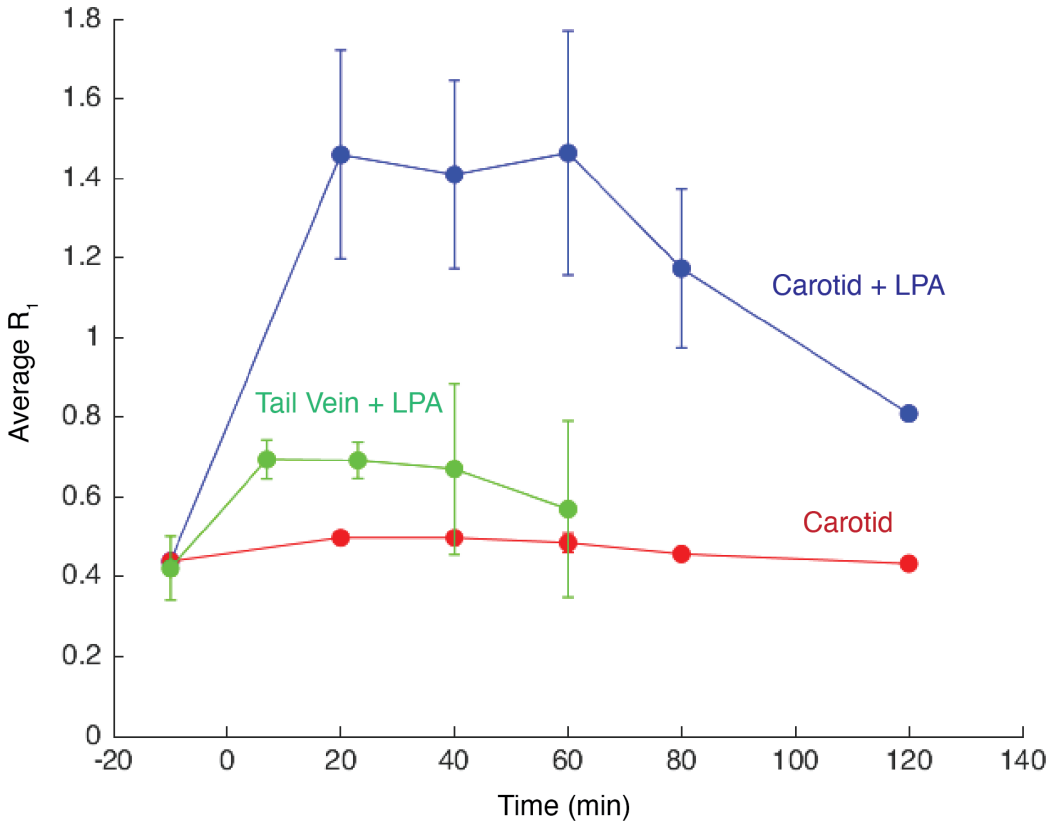

Figure S3: Average whole brain R_1 for carotid vs. tail vein catheter delivery. Conditions shown include: carotid catheter with LPA, tail vein with LPA, and carotid delivery with no LPA.

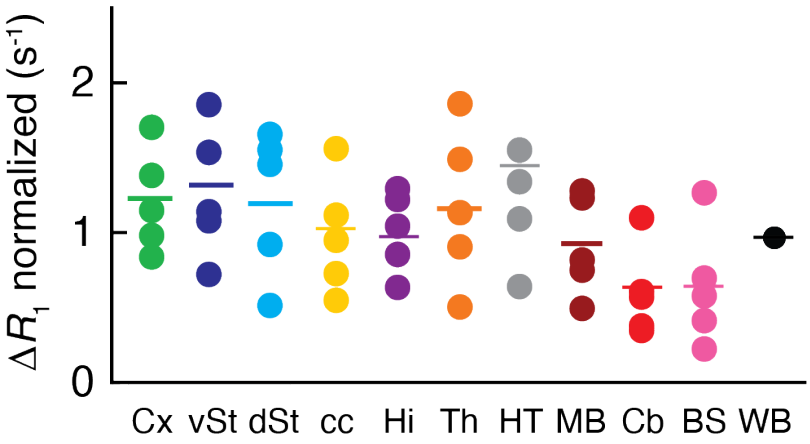

Figure S4: Normalized ΔR_1 distribution for LPA condition.
Distribution of contrast agent in the LPA condition normalized to the ΔR_1 of the whole brain.

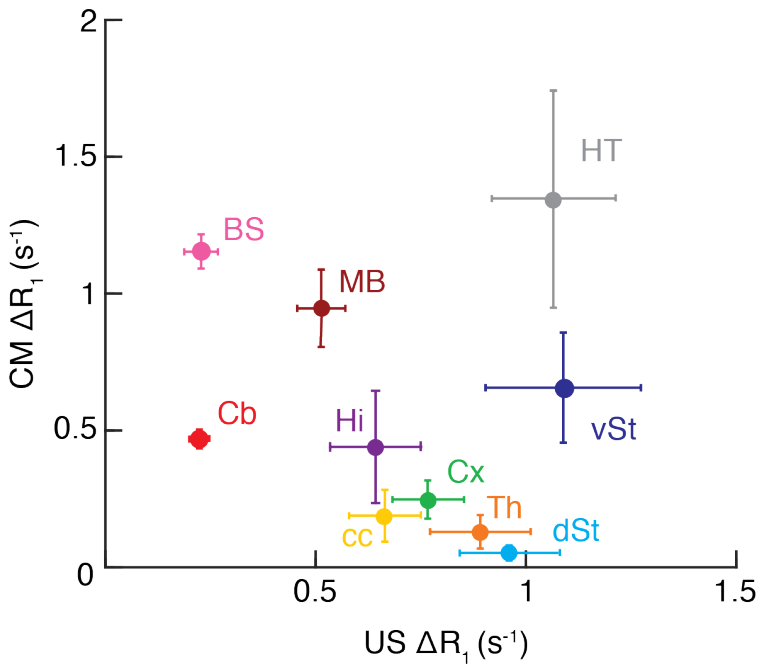

Figure S5: ΔR_1 comparison between CSF infusion and US-mediated delivery.

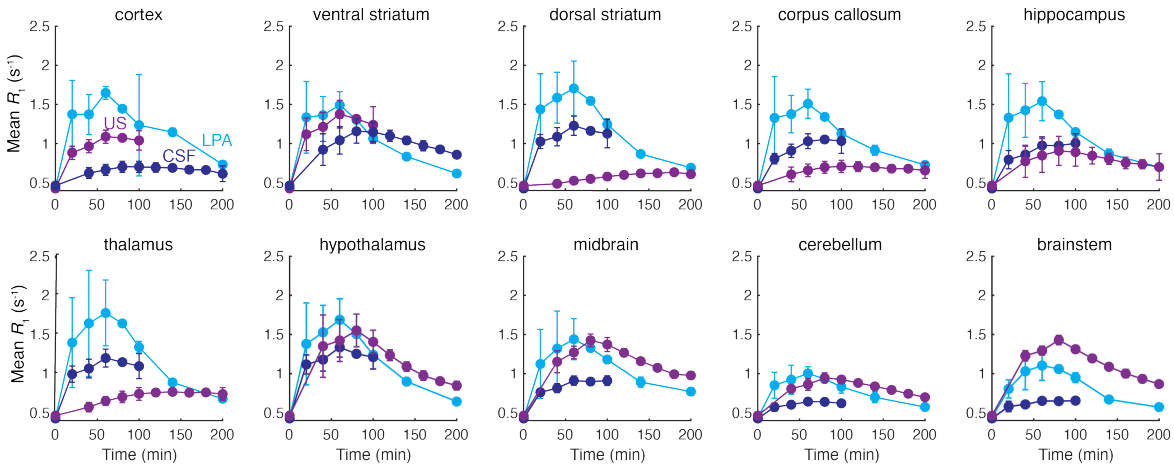

Figure S6: R_1 time courses of individual ROIs.

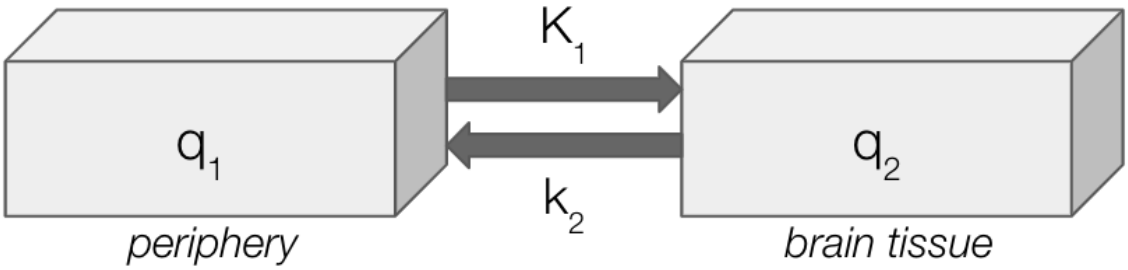

Figure S7: 2-compartment model

The standard solution to a two compartment is as follows:

$$q_2(t) = K_1 q_1(t) \otimes \ e^{-k_2 t}$$

With input function $q_1(t) = Ae^{-}k_1 t$, this means that:

$$q_2(t) = AK_1 \int_0^t e^{-k_1 s} e^{-k_2(t-s)} ds$$

$$q_2(t) = AK_1 \int_0^t e^{-(k_1-k_2)s} e^{-k_2 t} ds$$

$$q_2(t) = \frac{AK_1 e^{-k_2 t}}{k_2 - k_1} e^{-(k_1-k_2)s} \Big|_0^t$$

$$q_2(t) = \frac{AK_1 e^{-k_2 t}}{k_2 - k_1} (e^{-(k_1-k_2)t} - 1)$$

$$q_2(t) = \frac{AK_1}{k_2 - k_1} (e^{-k_1 t} - e^{-k_2 t})$$

A physical interpretation of k_2 is that it is the washout rate from compartment 2 (the brain) and k_1 is the washout rate from the input compartment. Thus, the equation can be rewritten in the following manner:

$$q_2(t) = \frac{AK_1}{k_{out} - k_{in}} (e^{-k_{in} t} - e^{-k_{out} t})$$

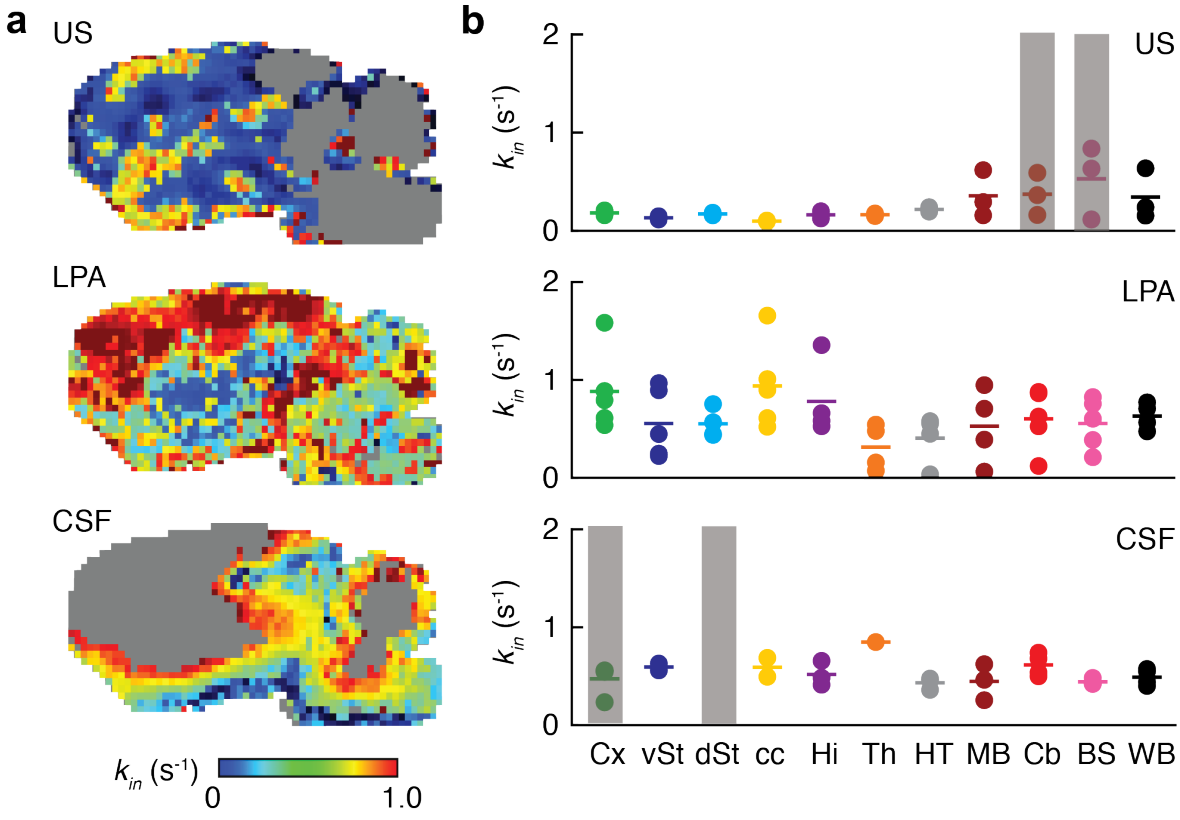

Figure S8: k_{in} for each delivery method.

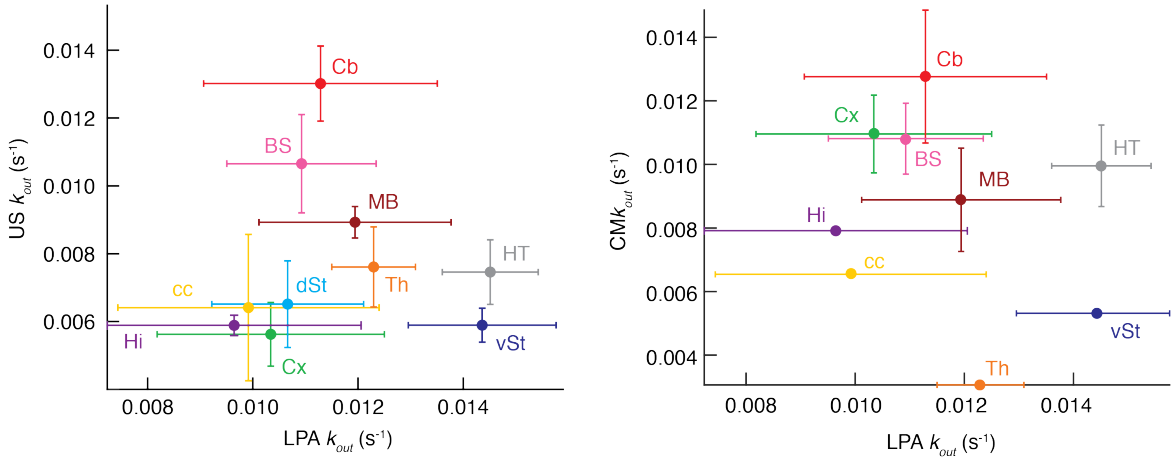

Figure S9: LPA ROI k_{out} values compared to other techniques.

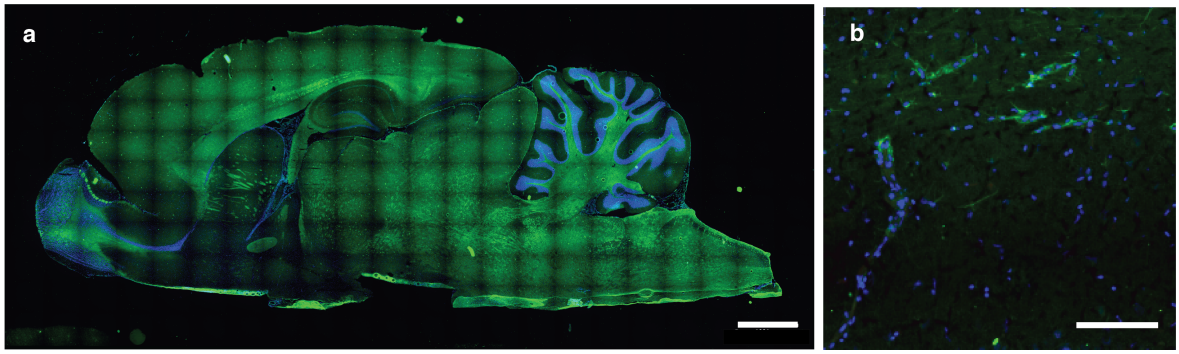

Figure S10: $LPAR_6$ staining in parasagittal slice.
(a) Whole brain staining ($LPAR_6$ = green, Hoescht = blue, lectin = red, scale bar = 2mm). (b) Expression of $LPAR_6$ localized around vasculature (scale bar = 100 μm).

	Lectin Fluoresence (a.u.)	Claudin-5 Fluoresence (a.u.)
LPA k_{out}	0.201 (p=0.578)	-0.3766 (p=.283)
LPA k_{out} (w/o vSt and HT)	0.979 (p=8.23x10^{-7})	0.9971 (p=1.19x10^{-6})
US k_{out}	0.734 (p=0.038)	0.792 (p=0.040)
CM k_{out}	0.7741 (p=0.086)	0.788 (p=0.007)

Table S1: Correlation of vascular marker and tight junction protein to k_{out}. The Pearson correlation coefficient and p-value is listed for each condition.

Chapter 3

Probing cholinergic activity with MRI

This work was done in collaboration with Dr. Sajal Sen.

3.1 Abstract

Developing molecular imaging strategies to monitor cholinergic function in living tissue is of outstanding interest in neuroscience. A tractable approach in this regard is to measure activity of cholinesterase enzymes (ChEs), which lyse choline esters at synapses. Although optical and nuclear imaging probes have been available to study ChEs, existing strategies tend to lack spatiotemporal resolution or suffer from hazardous exposure to radioactivity. To address this problem, we have developed an imaging probe that allows activity of ChE to be mapped using magnetic resonance imaging (MRI). Our agent, called ChERT, undergoes enzymatic processing that reduces its solubility, promoting accumulation near sites of ChE activity. ChERT produces particularly strong MRI contrast enhancements in brain regions known to be enriched in ChE; these signals could also be confirmed by postmortem fluorescence and photoacoustic imaging owing to the strong optical activity of ChERT. ChERT-mediated MRI changes were suppressed in the presence of the ChE inhibitor tacrine, further supporting the specificity of the molecular imaging results. ChERT should thus provide a means for preclinical assessment of phenotypes and treatments that interact with ChE, in the long term possibly including cholinergic activity monitoring and ChE-related disease diagnosis in humans.

3.2 Introduction

Acetylcholine (ACh) is a prominent neurotransmitter in the peripheral and central nervous system and a key component of cholinergic activity. Hydrolysis of ACh at synapses is critical for keeping the cholinergic system functional and neural system regulated [95]. Cholinesterase enzymes (ChE), namely, acetylcholinesterase (AChE) and butyrylcholinesterase (BChE), play a vital role by catalyzing this hydrolysis reaction [96]. Cholinergic dysfunction, especially abnormal ChE activity, have been associated with neurological diseases and disorders. In fact, several ChE inhibitors have been approved by the Federal Drug Admnistration for symptomatic treatment of Alzheimer's disease [97]. Therefore, developing probe technologies for real-time and in situ monitoring of intrinsic ChE *in vivo* is of significant interest.

To this end, several probes have been developed for monitoring AChE and BChE activity via fluorescence imaging and nuclear imaging, namely, SPECT and PET techniques [98–100]. These sensors provided valuable information for monitoring enzyme activity and high throughput screening of inhibitors. However, applications of optical probes are limited by trade-offs between depth and resolution, and use of radioligands incur harmful exposure to radiation. Histochemical analyses and enzyme-specific immunostaining have been reported for investigating ChE distributions in brain, but they can only provide information at a singular post-mortem timepoint [101, 102]. Magnetic resonance imaging (MRI) can overcome these challenges by extending the reach of deep tissue activity measurements *in vivo*. Developing ChE-responsive MRI contrast agents provides a non-radioactive platform with better spatiotemporal resolution for longitudinal studies of cholinergic activity.

Previous work from our lab has demonstrated the the use of a "solubility switch" mechanism to detect enzymes using molecular level MRI. Specifically, secreted alkaline phosphatase (SEAP) catalyzes conversion of a soluble MRI contrast agent into an insoluble product that accumulates at sites of phosphatase activity. This approach aids the visualization of enzyme distribution [29]. We surmised that a related mechanism could be used to generate a probe with selective accumulation and contrast enhance-

ment at sites of ChE activity. This mechanism provides two powerful advantages for ChE detection by molecular-level MRI. First, enzymatic amplification as the basis for MRI detection allows for a single unit of enzyme to act on multiple units of contrast. Second, the ChE-mediated hydrophobicity changes provides a mechanisms for assessing ChE activity over a broad range of temporal scales.

MRI probes based on gadolinium texaphyrin (Gd-Tex) platforms constitute an attractive basis for implementing this design (Figure 1a). Historically, Gd-Tex has been widely used as a tumor-selective MRI contrast agent, but more recently, it has been explored as a basis for neuroimaging sensors [103, 104]. Gd-Tex's hydrophobic nature makes it particularly amenable to the solubility switch approach. Besides absorbing strongly in the visible range, the versatile Tex platform will also enable the new ChE probes to be detectable by photoacoustic tomography (PAT) and fluorescence imaging. This multi-modality will permit the valuable integration of readouts over a range of spatial scales, both in living subjects and postmortem tissue. To this end, we have created and characterized a small library of candidate ChE-activity dependent imaging agents, termed as ChE Responsive Texaphyrins (ChERT).

3.3 Results

3.3.1 Design and synthesis of a cholinesterase responsive texaphyrin molecule

ChERT compounds were synthesized via an amide coupling reaction of the bis-amine version of Tex, Gd-Tex-$(NH_2)_2$, to novel choline-derivative synthons (Figure 1b). It is worth noting that in this work, Gd-Tex-$(NH_2)_2$ was obtained using a modified synthetic protocol that makes the reaction more feasible at a large scale as it does not require an inert atmosphere and dry reagents (Supplementary Figure 1). The library compounds use the same Tex framework with the linkers varying the distance and rigidity between the metal and choline moiety (Figure 1c, Supplementary Figures 2-5). After purification and characterization of the target compounds (Supplementary

Figures 6,7), stability of these complexes was compared in conditions emulating the brain environment. The results showed that within two hours, compounds 1-3 undergo rapid self-hydrolysis into intermediate and product molecules (Supplementary Figure 8). This hampers these compounds in their ability to evaluate ChE activity. In contrast, the ChERT compound undergoes self-hydrolysis at a slower rate with no formation of the product within the first 2 hours. Therefore, *in vitro* screening tests helped validate the ChERT compound as the leading candidate for further *in vitro* and *in vivo* studies. A close analog of ChERT that features an amide bond instead of the ester bond was also synthesized and employed as a control molecule for its lack of a esterase-cleavable moiety (Figure 1c).

3.3.2 *In vitro* characterization of ChERT confirms its specificity to cholinesterase

Next, we tested the cholinesterase sensitivity of ChERT *in vitro*. Liquid chromatography mass spectrometry (LCMS) studies indicated that ChERT undergoes complete bis-ester hydrolysis in the presence of ChE enzymes (Figure 2a, Supplementary Figure 9). Studies revealed that ChERT is more responsive towards BChE compared to AChE, which is reflected in the enzyme quantity and corresponding incubation time required for full conversion to product (Figure 2a). When incubated in the presence of a ChE inhibitor, tacrine, the product formation can be restricted, as demonstrated by LCMS results (Supplementary Figure 10). In congruence with its structural design, the control compound remains intact even after incubation with higher concentrations of ChE (Figure 2b). A visible color change can be observed from light to brownish green upon completion of hydrolysis. The product can then be pelleted by centrifugation (Figure 2c). This increase is particle size was confirmed with DLS (Figure 2d, Supplementary Figure 11). However, a similar trend was not observed with the control compound or in the presence of tacrine where the particle size remained the same over the course of its study (Supplementary Figure 12).

Next, ChE-mediated MRI response was monitored using longitudinal relaxation rate (R_1) maps. Before adding the enzyme, ChERT exhibited a relaxivity (r_1, slope of

R_1 versus concentration) of 12.7 ± 0.3 mM^{-1} s^{-1}. The addition of ChE caused a dramatic 48% change in relaxivity when 100 µM ChERT was incubated with 1 U/ml enzyme over 2 h of incubation at 37 °C, compared to 8.8% with no enzyme added (Figure 2e). Coincubation of ChE inhibitor tacrine with ChE was found to restrict the MRI change to 12.6% (Figure 2e). The specificity of ChE-dependent MRI signal change was further confirmed when co-incubation of ChERT with human placenta alkaline phosphatase or porcine liver esterase did not exhibit a similar response (Supplementary Figure 13). In comparison, control compound displayed no change in MRI signal, even after incubation with higher amount of BChE, which justifies the design rationale and LCMS observation (Supplementary Figure 14). To determine whether ChE-dependent responses from ChERT can be detected by other imaging modalities, we first monitored the change using fluorescence spectroscopy. It was observed that ChERT fluorescence, with an excitation at 470 nm, partially decreased (40%) when incubated (100 μM) in the presence of BChE (1 U/ml) at 37 °C. (Figure 2f). At analogous conditions, PAT experiments showed a BChE-responsive dramatic signal increase (357%) for ChERT compared to the control (15%). For both techniques, ChE-responsive changes can be restricted to 95% by using tacrine (Figure 2g). Taken in concert, these *in vitro* results confirmed that ChERT is responsive to ChE and produces enzyme-dependent contrast changes detectable by MRI, fluorescence, and photoacoustic modalities.

3.3.3 ChERT exhibits cholinesterase specificity *in vivo* following widefield delivery

To test the predicted activity of the compound *in vivo*, we delivered ChERT to the rodent brain. To this end, 25 uL of the contrast agent (5 mM) was infused bilaterally using intracerebroventricular injection for wide field brain delivery in Sprague-Dawley rats followed by imaging at a 7T MRI. Using a T1-weighted sequence, a substantial increase in MRI signal intensity was observed near cortical and thalamic regions on both sides of the brain compared to the pre-injected version (Figure 3a). Following the MRI experiments, the rat brains were perfused and extracted for optical imaging and mass spectrometric studies. Accumulation and identity of the product in the brain

were confirmed via LCMS with brain slices (Supplementary Figure 16). Owing to the strong green color of Tex, the spread of the product can be visualized in intact perfused brains and brain slices (Figure 3b). Ex vivo PAT experiment demonstrated strong photoacoustic signal from the presence of the product in the brain (Figure 3c).

We next aimed to assess the differential distribution of cholinesterase in various subregions throughout the rodent brain. All of this was done in comparison to a control condition in which the sensor was co-infused with 2.5 mM tacrine inhibitor. In the ventral tegmental area (VTA) and septal nucleus, a significant difference between the two conditions was not present (n=8 each condition, Figure 3d). This matches literature in which a lack of AChE or BChE has been identified in these subregions [101, 102, 105]. However, in the regions such as the lateral habenula and paraventricular thalamus (PVT), the difference was significant (p=0.0198 and 0.0387, Figure 3d,e). Furthermore, we found subregion specificity that certain thalamic nuclei (anterodorsal and laterodorsal) exhibited this significant increase in signal in the non-inhibited condition (p=0.0369, Figure 3d,e). These results match trends in the literature that identify these thalamic nuclei, lateral habenula, and PVT as regions of high BChE activity despite lacking much AChE [102].

To investigate the correlation between differential fluorescence signal enhancement with ChE distribution in the rat brain, we labeled BChE in the brain tissue following an immunostaining protocol. Selectively higher expression of BChE was observed in the anterodorsal thalamic nucleus compared to the rest of the thalamus, which is in accordance with the literature (Figure 3f). From these data combined, we can infer that higher accumulation of the product occurred in ChE enriched brain regions.

To further check specificity of the enzyme mediated accumulation of the product, we conducted ICPMS study with the brain slices from both cohorts collected 2 hours post injection. This revealed that ChERT treated rodent brains had $\tilde{6}0\%$ higher amount of Gd, which is congruence with higher accumulation of the product as concluded from MRI studies (Figure 3g). Taken in concert, these studies indicate that co-injection of tacrine caused less product accumulation from ChERT, owing to ChE inhibition, that was reflected in imaging and mass spectrometric studies.

3.3.4 Kinetics of ChERT reflect regional cholinesterase activity

Next, to predict cholinesterase activity *in vivo*, we developed a pharmacokinetic model. The kinetic parameters, k_{cat} and K_m, were measured from i*n vitro* studies in which time dependent product formation following incubation of ChERT with enzyme was monitored using HPLC (Supplementary Figure 16). The k_{out} of cleaved compound was estimated from previous studies of hydrophobic metallophyrin precipitates [28]. The k_{out} of uncleaved compound was based on the average rate of clearance for a macrocyclic compound as computed in Chapter 2. The results predicted that within minutes of probe delivery, changes in T_1 relaxation rate occur in approximately inverse proportion to the local concentration of BChE in the brain, modeled to vary in a physiologically relevant range from 0.01 to 10 nM (Figure 4b).

We predicted that over an extended time period (2.5 hours), more complex contrast dynamics are observed, such that BChE-rich areas are predicted to exhibit higher T_1 values due to slower washout of hydrolyzed probe versus the uncleaved ChERT. We fit our *in vivo* data to a two-compartment model (as demonstrated in Chapter 2). This allowed us to extract a k_{out} parameter describing the clearance of compound. The k_{out} is shown to in fact be higher (indicating faster clearance) in regions lacking BChE expression (Figure 4c). Mapping out the the average fitted curve for each region of interest, we see regions with higher BChE concentration map to slower washout kinetics (Figure 4d). Such kinetic features are expected to depend quantitatively on BChE activity levels in tissue.

3.4 Conclusion

In summary, our results demonstrated in this work validate that the rationally designed probe ChERT can detect cholinesterase activity both *in vitro* and *in vivo*. Benefiting from the multimodal imaging properties of the texaphyrin framework and solubility switch mechanism, ChERT showed its utility in mapping cholinesterase distribution in the rodent brain. Furthermore, a T_1 weighted MRI contrast dynamics was observed in

BChE-enriched regions in the presence or absence of the ChE inhibitor tacrine and the MRI results from temporal studies can predict BChE activity in a kinetic model. As future directions, ChERT provides a means for preclinical assessment of phenotypes and treatments that interact with ChE and ChE-related disease diagnosis. Further efforts will be focused on improving sensitivity of ChERT towards cholinesterases, in particular, AChE. Analogs of ChERT can also be manipulated for detecting other biologically important enzymes playing major roles in the nervous system.

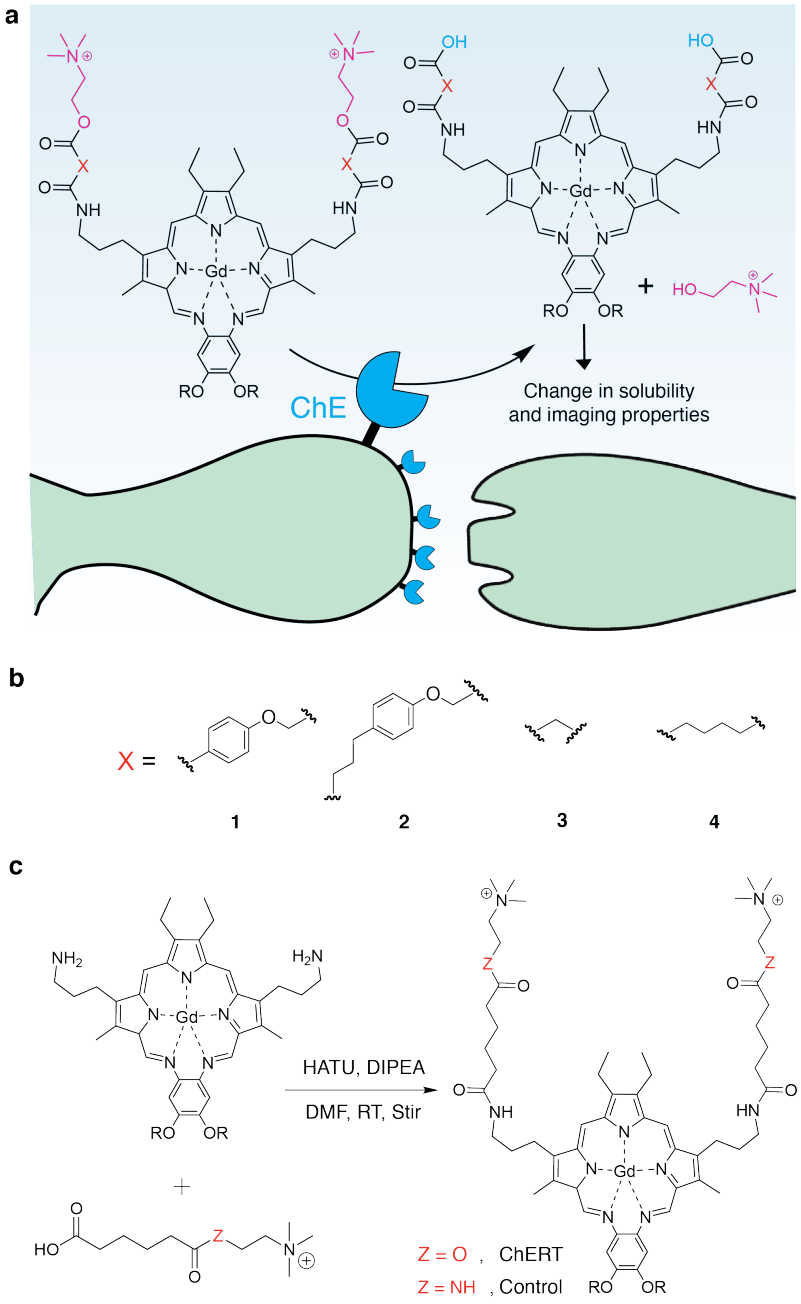

Figure 3.1: **Design of cholinesterase responsive texaphyrin molecule.** (a) The ChERT compound is the synthesis of a Gd-Tex compound with a choline derivative. In the presence of cholinesterase enzyme, the substrate is cleaved and forms an insoluble precipitate. (b) Choline-derivative synthons tested with the bis-amine version of Tex to form candidate compounds. (c) The control compound possesses an amide bond in place of the cleavable ester.

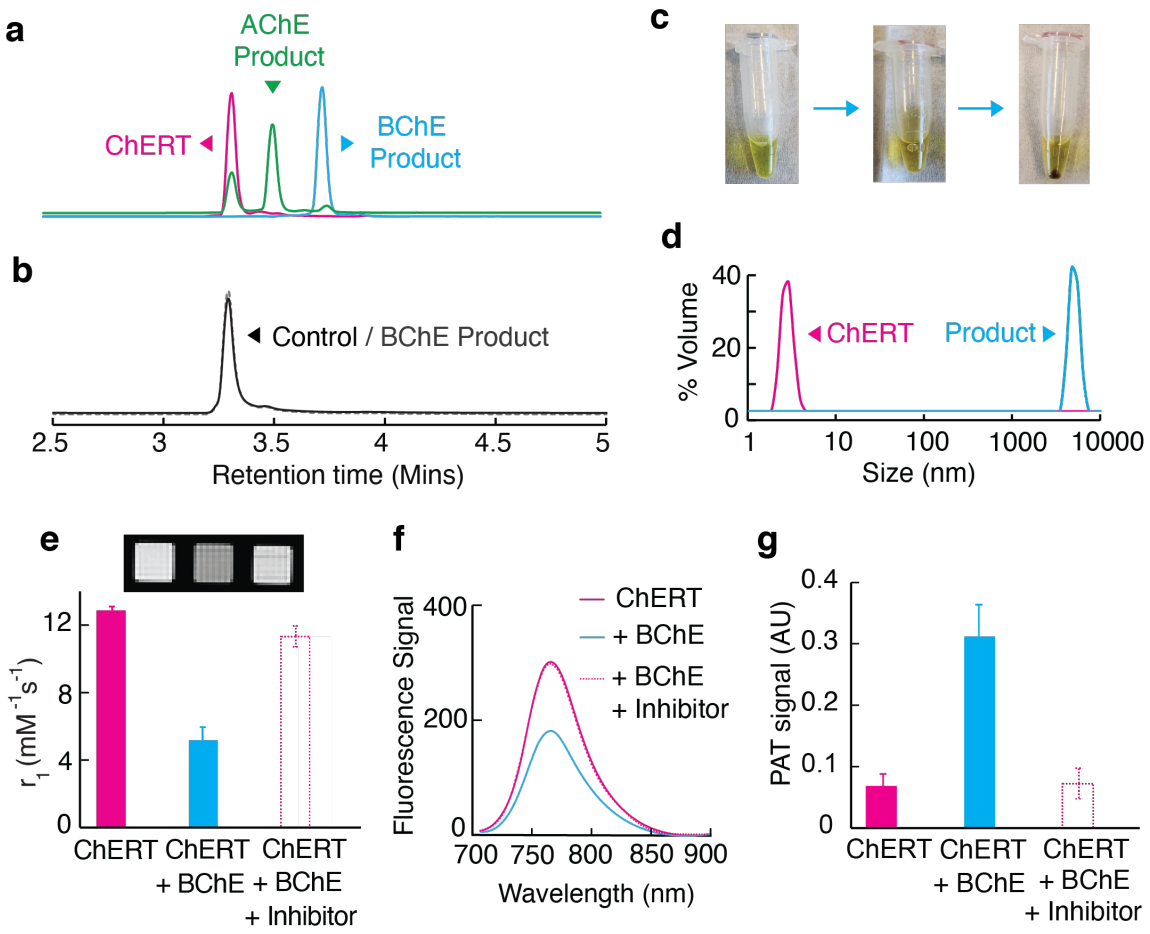

Figure 3.2: ***In vitro* characterization of ChERT.**
(a) Liquid chromatography data tracks conversion of ChERT into hydrolyzed product. (b) The control compound does not undergo hydrolysis in the presence of BChE. (c) Visible change of ChERT following incubation with enzyme and subsequent centrifugation. (d) DLS shows increase in particle size following ChE incubation. Properties of compound are altered by ChE and rescued when in presence of inhibitor for (e) MRI (f) fluorescence, and (g) photoacoustic tomography.

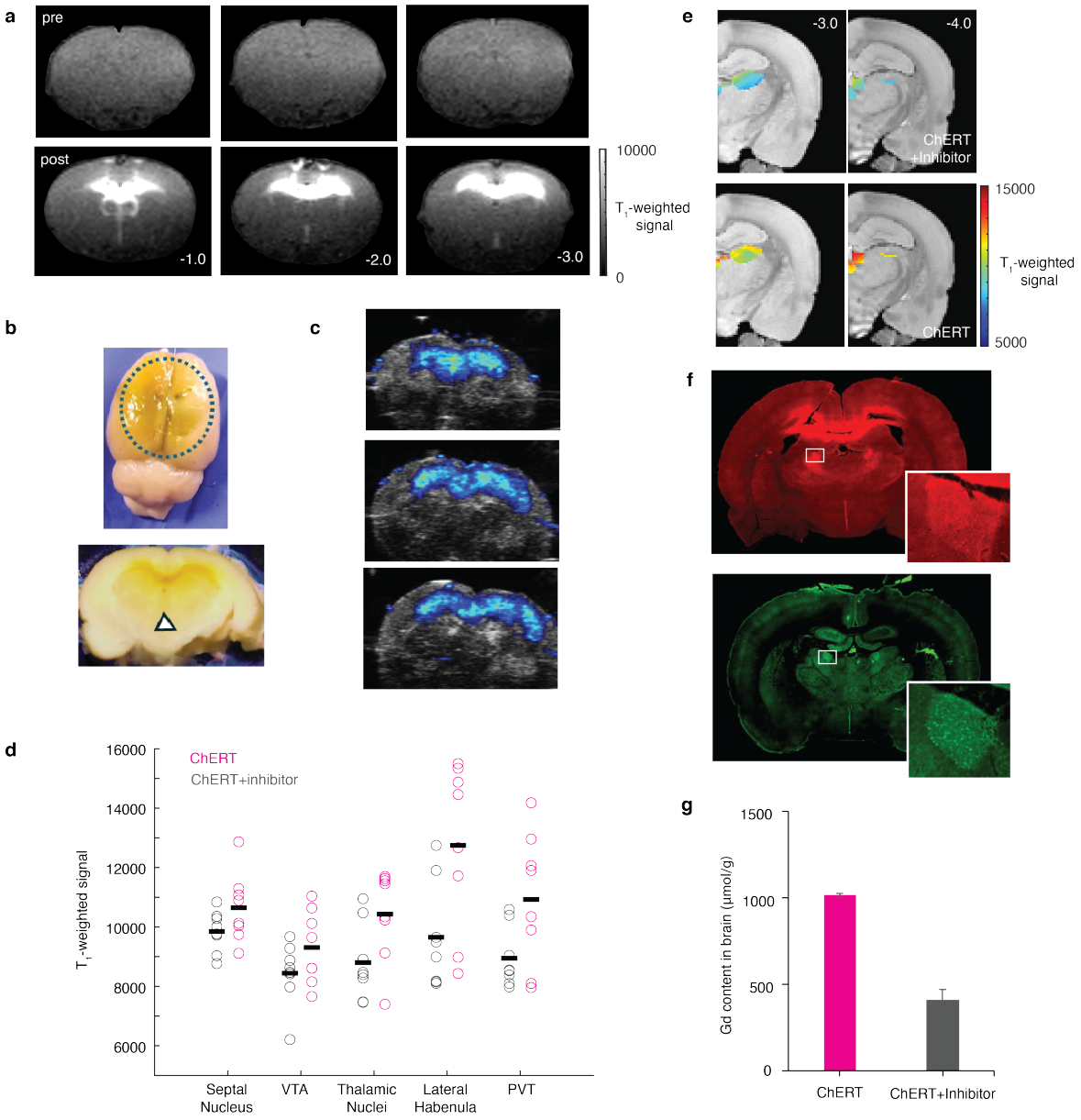

Figure 3.3: **Widefield delivery of ChERT *in vivo*.**
(a) Representative T1-weighted image showing the increase in MRI siginal intensity following intracerebroventricular injeciton. (b) Visual spread of the sensor can be see in both the intact and sliced brain. (c) *Ex vivo* PAT showing presence of compound (d) After 90 minutes, ChERT with inhibitor shows statistically significant difference from the uninhibited condition in the thalamic nuclei, lateral habenula, and paraventricular thamalus (PVT) ($p<0.05$). (e) Average T_1-signal of ROIs that have significant increase overlaid on an atlas image. (f) Fluorescent image of rat brain 90 minutes after ICV infusion of ChERT compared to a BChE stained wild-type brain. (g) ICP-MS of gadolinium content of brains 2 hours post-injection.

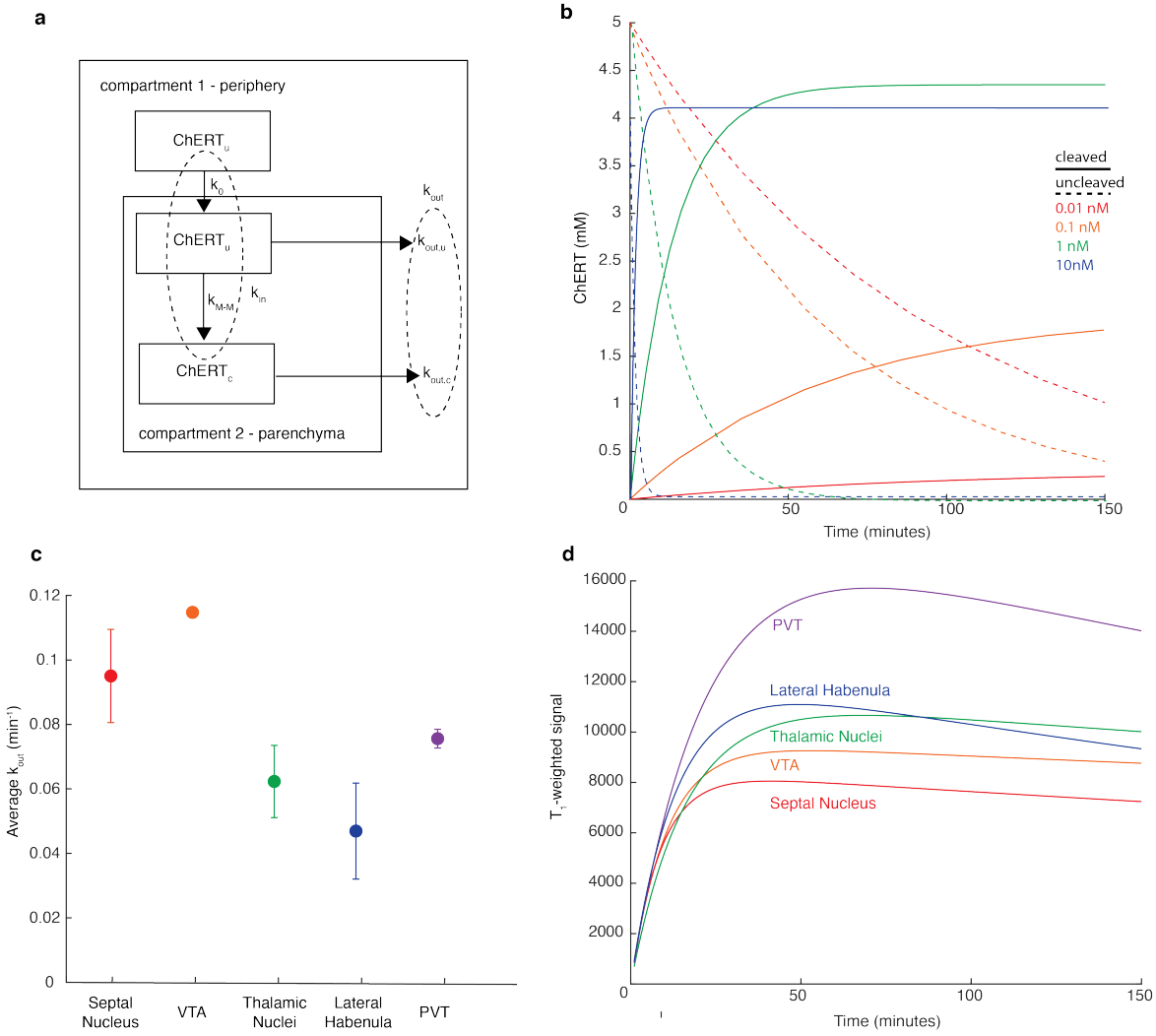

Figure 3.4: **Kinetics of ChERT reflect regional cholinesterase activity.** (a) Schematic of two-compartment model of ChERT delivery (k_{in}) with k_0 representing delivery of uncleaved ChERT (ChERT$_u$) into brain parenchma, k_{M-M} representing Michaelis-Menten kinetics of conversion to the cleaved compound (ChERT$_c$). Clearance (k_{out}) of uncleaved ($k_{out,u}$) and cleaved ($k_{out,c}$) compound. (b) Simulated concentration of cleaved and uncleaved agent in the presence of ChE concentration (0.01-10nM). (c) Average k_{out} fit model fits for ROIs. (d) Simulated T1-signal obtained from model parameters.

3.5 Materials and Methods

Reagents and materials

Solvents and starting materials were purchased from Fisher Scientific, Ambeed or Sigma Aldrich and used without further purification unless otherwise specified. Reaction progress was monitored by thin-layer chromatography (TLC, silica gel 60 F_{254}, EMD Millipore) or by LC-MS analysis (see the "Mass spectrometry" section below for further details). Texaphyrin and ChERT conjugates were purified by RP-tC18 SPE (Waters SepPak, waters®) columns containing 10 g or 2 g of C-18 using an increasing gradient of acetonitrile in either 0.1M ammonium acetate/1% acetic acid aqueous solution or a 0.1M aqueous potassium nitrate, depending on which counter anion (AcO or NO_3) was desired as the ancillary ligands for the gadolinium (III) center.

Optical spectroscopy

UV-visible spectra were recorded on a SpectraMax M2 spectrophotometer from Molecular Devices. Fluorescence spectra were recorded on a Cary Eclipse spectrofluorometer from Varian.

Photoacoustic Imaging

Photoacoustic data were recorded in the MIT Koch Institute Animal Imaging and Preclinical Testing Core, using a Fujifilm-Visualsonics Vevo3100/LAZRX ultrasound and photoacoustic imaging system equipped with a MX250S transducer (1530 MHz, center transmit: 21 MHz; axial resolution: 75 m). The solutions were injected into polyurethane tubes, which were immobilized by immersion in 1% agarose gel within the sample holder chamber. A layer of ultrasound gel was placed between the agarose gel surface and the transducer. For imaging of ex vivo rat brains, specimens were placed on an agarose gel bed and embedded in ultrasound gel. The transducer was then placed on the superior part of the brain, and the PAT signal was recorded. For 3D imaging, the interplanar step was set to 152 m. The excitation laser wavelength

was set at 750 nm.

Mass spectrometry

Mass spectrometric analyses were carried out in the Massachusetts Institute of Technology (MIT) Department of Chemistry Instrumentation Facility (DCIF), using LCMS, QToF, and MALDI-ToF instruments. The low-resolution LCMS studies were made using a nominal mass Agilent 6125B mass spectrometer attached to an Agilent 1260 Infinity LC. This instrument has an electrospray ionization (ESI) source with fast polarity switching to measure positive and negative ions simultaneously. The diode array has a wavelength range of 190 to 640 nm, and a measurable m/z range of 100 to 1500 daltons. The QToF is a high-resolution Agilent 6545 mass spectrometer coupled to an Agilent Infinity 1260 LC system that relies on a Jet Stream ESI source. The system has a mass accuracy of 1-3 ppm using real-time calibration, with a mass resolving power of 45,000 full width at half-maximum (FWHM) at m/z of 2722. MALDI -ToF measurements were made using a high-resolution Bruker Autoflex LRF Speed mass spectrometer. For ICPMS, brain slices from two rat cohorts were digested in 70% nitric acid at 60 °C for 6h and centrifuged at 10000g for 5 mins. The supernatant was collected and filtered through a 0.22 uM filter with the final residue suspended into 2% nitric acid. The ICP-MS spectra were recorded on an Agilent 7900 system.

Nuclear magnetic resonance

NMR spectra were recorded in the DCIF on either a three-channel Bruker Avance Neo 500 MHz spectrometer or a two-channel Bruker Avance-III HD Nanobay 400 MHz spectrometer. Both instruments are equipped with a 5 mm liquid nitrogen-cooled Prodigy Broadband Observe cryoprobe.

Animals

All animal procedures were performed in strict compliance with US Federal guidelines, with oversight by the MIT Committee on Animal Care. Male Sprague-Dawley rats (150-300g) were purchased from Charles River Laboratories (Wilmington, MA)

and used for the *in vivo* data presented in this paper. All animals were housed and maintained on a 12h light/dark cycle with ad libitum access to food and water.

Intra-CSF infusion

Animals were prepared for cranial surgery to expose the skull. A total of 8 rats received infusions. Each animal was anesthetized with isoflurane (4% for induction, 1.5-2% for maintenance). A small hole was drilled into the skull at the following coordinates: .9 mm posterior and +/-1.4 mm lateral to bregma. 33 gauge infusion cannula held by sterotaxic arms was then lowered into the brain 3.6 mm below the skull surface. 5 mM ChERT sensor (n=4) or 5 mM ChERT sensor with 2.5 mM tacrine inhibitor (n=4) was infused at a rate of 0.15 μL/min (25μL per side). The syringe was slowly removed 5 minutes after the infusion. Skin incisions were closed by sterile sutures. Skin incisions were closes with Vetbond tissue adhesive (MIT Pharmacy), and rats were transferred to the MRI for scanning.

Magnetic resonance imaging

All animals were imaged using a 7T Biospec MRI scanner (Bruker, Ettlingen, Germany) scanner operating with custom-made surface coils. High resolution anatomical images were obtained with a TurboRARE (rapid acquisition with relaxation enhancement) sequence with a TE of 33ms, TR of 2.5 s, a RARE factor of 8, and 12 averages. The geometry of the scan incorporated 256x256 matrices over a 2.25 x 2.25 cm FOV for a 18-slice volume with 1 mm slice thickness aligned at the olfactory bulb. This was followed by repetitions of a T_1-weighted FLASH sequence. Parameters were a TE of 4.245 ms, FA = 30, TR = 250 ms, FOV = 1.92$\times$ 1.2 cm, 128x80 matrices for an in-plane resolution of approximately 150 $\times$ 150 μm, and 18 slices with slice thickness = 1 mm.

For each scan session, rats were kept at 1.5% isoflurane in oxygen-enriched air. Animals were warmed using a water-heating pad. Heart rate and blood oxygenation saturation level were continuously monitored using an MRI-compatible infrared pulse

oximeter (Nonin Medical, Plymouth, MN).

MRI data analysis

Images were reconstructed in ParaVision 7 software and then imported into into the National Institute of Health AFNI software package. Alignment was performed by registering high-resolution anatomical images of each rat to a Waxholm coordinate space rat brain atlas. The images were then motion corrected using rigid-body volume correction.

All further analysis was performed in MATLAB (Wolfram) using custom scripts. ROIs were obtained from the Waxholm atlas. For determining ROI- level signal differences measurements were taken from images at 1.5 hours post-injection in the ChERT and ChERT with inhibitor conditions. A two-tailed, paired sample t-test was used to quantify p-values.

In vitro kinetic parameter determination

ChERT (substrate) was incubated with 1 U/ml BChE (1.8 nM) at different concentrations (25 uM, 50 uM, 75 uM, and 100 uM) at 37C. Aliquots from the solution were collected at different timepoints (1 mins, 5 mins, 10 mins, 15 mins, 20 mins, and 30 mins) and subjected to HPLC monitoring. The formation of the product was calculated using the area obtained from HPLC chromatogram. Using the Lineweaver-Burk plot (double-reciprocal plot) using V_0 (initial velocity) and [substrate], we obtained V_{max}, K_m, and K_{cat} values, respectively.

Kinetic modeling

The MATLAB SimBiology toolbox was used to model the Michaelis-Menten kinetics uncleaved ChERT converting to its cleaved and precipitated form, as well as the compound's clearance from the parenchyma. The following conditions were used: initial concentration = 5 mM, k_{cat} = 9645 min^{-1}, K_m = 148 μM, and enzyme concentrations = 0.01 nM, 0.1 nM, 1 nM, and 1 nM. The clearance of uncleaved agent was estimated to be 0.01 min^{-1} based on the average rate of clearance of a macrocyclic

compound estimated in Chapter 2. The clearance of cleaved agent in its precipitated form was estimated to have a half-life of 2 days based on previous literature of a similar agent [29].

Kinetic modeling *in vivo* used the T_1-weighted signal collected 2.5 hours post-injection. The average signal of an ROI was extracted from data fit to the Waxholm atlas. This data was fit to a two compartment model roughly approximating the influx of T_1-weighted agent (in both its cleaved and uncleaved form) as well as its efflux from the parenchyma (reference Chapter 2 for the derivation of the 2-compartment model).

$$q_2(t) = \frac{AK_1}{k_{in} - k_{out}}(e^{k_{out}t} - e^{k_{in}t})$$

Only fits with an R^2 above 0.7 were accepted. For each ROI, the fitted parameters were averaged across rats.

Immunohistochemistry

The animals were transcardially perfused with PBS followed by 4% paraformaldehyde in PBS. The brains were extracted, post-fixed overnight at 4°C and sectioned the following day. Free-floating sections (50µm thick) were cut using a vibratome (Leica VT1200 S, Leica Microsystems GmbH). We performed antigen retrieval by incubating brain sections in sodium citrate buffer (pH 6) for 30min at 80°C. For blocking unspecific antigen-antibody interactions, we used 10% donkey serum. Expression of BChE was assessed by overnight incubation with primary antibodies (1:100 dilution, 4 °C, AF-9024, R&D Systems), followed by a 1h incubation with matching secondary antibodies anti-Goat Alexa Fluor 488 (1:400 dilution, A11055, Invitrogen, RT). Finally, we incubated brain slices with Hoechst for 10 mins (1:2000 dilution, H3570, Invitrogen) for nuclei staining. The stained brain sections were mounted on glass slides with Invitrogen ProLong Gold Antifade (Fisher Scientific Company) and protected with a coverslip. Fluorescence imaging was performed using a confocal microscope (Axio Imager 2, Zeiss).

3.6 Supplementary Information

Texaphyrin component	Choline component	Final Product	Self-hydrolosis into product (%)
MGd-Bis amine	L1	ChERT	0
MGd-Bis amine	L2	Control	0
MGd-Bis amine	L3	1	35
MGd-Bis amine	L4	2	39
MGd-Bis amine	L5	3	42

Table S1: Summary of compounds investigated for ChERT sensor.

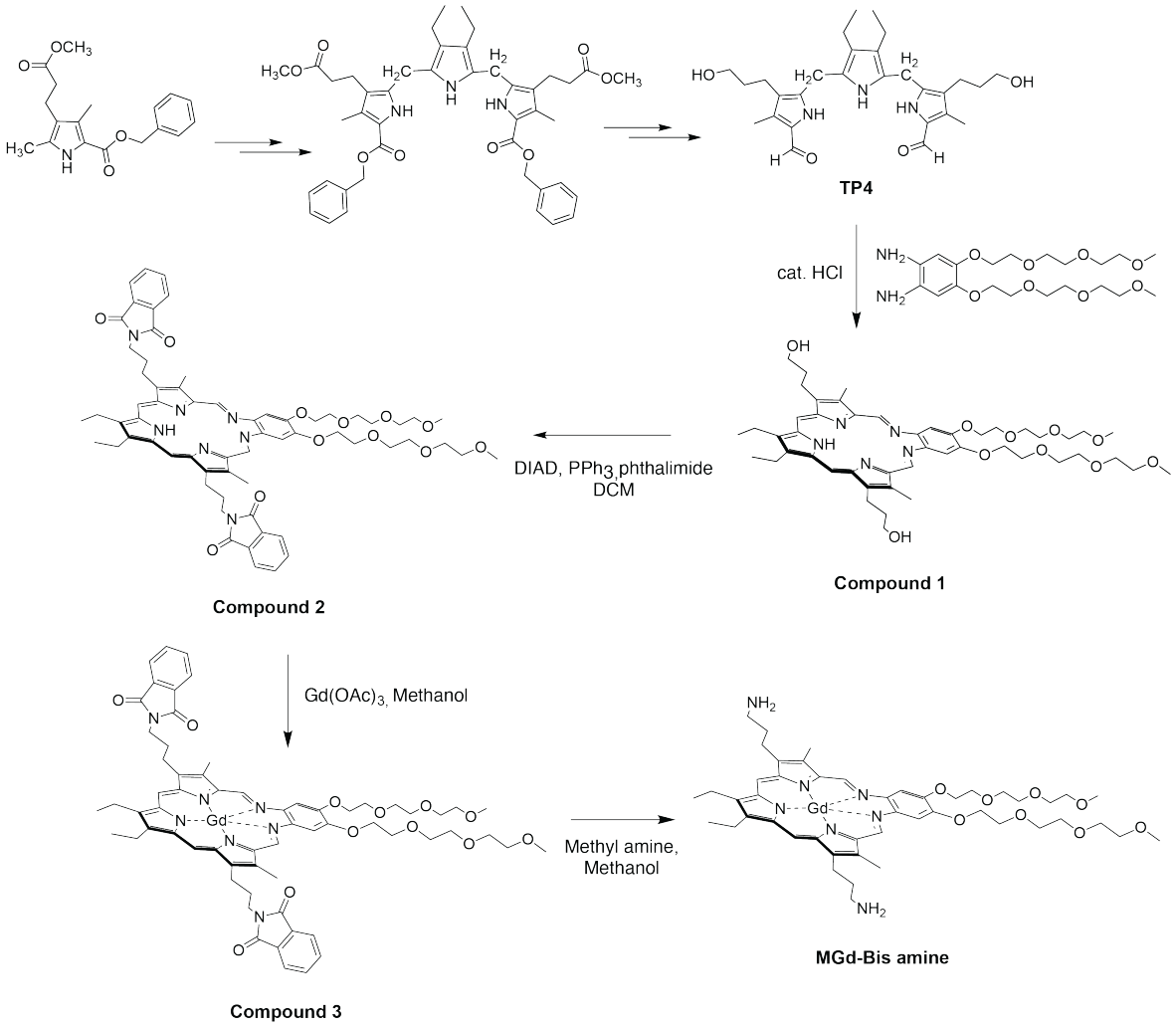

Figure S1: Modified synthesis of MGd-Bis amine.

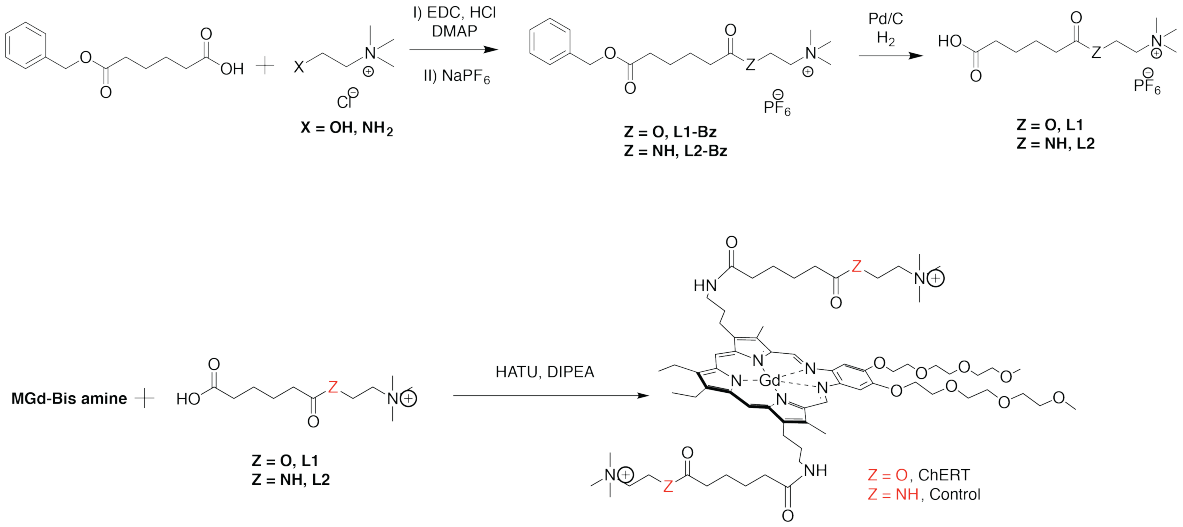

Figure S2: Synthesis of L1, L2, ChERT and control compound.

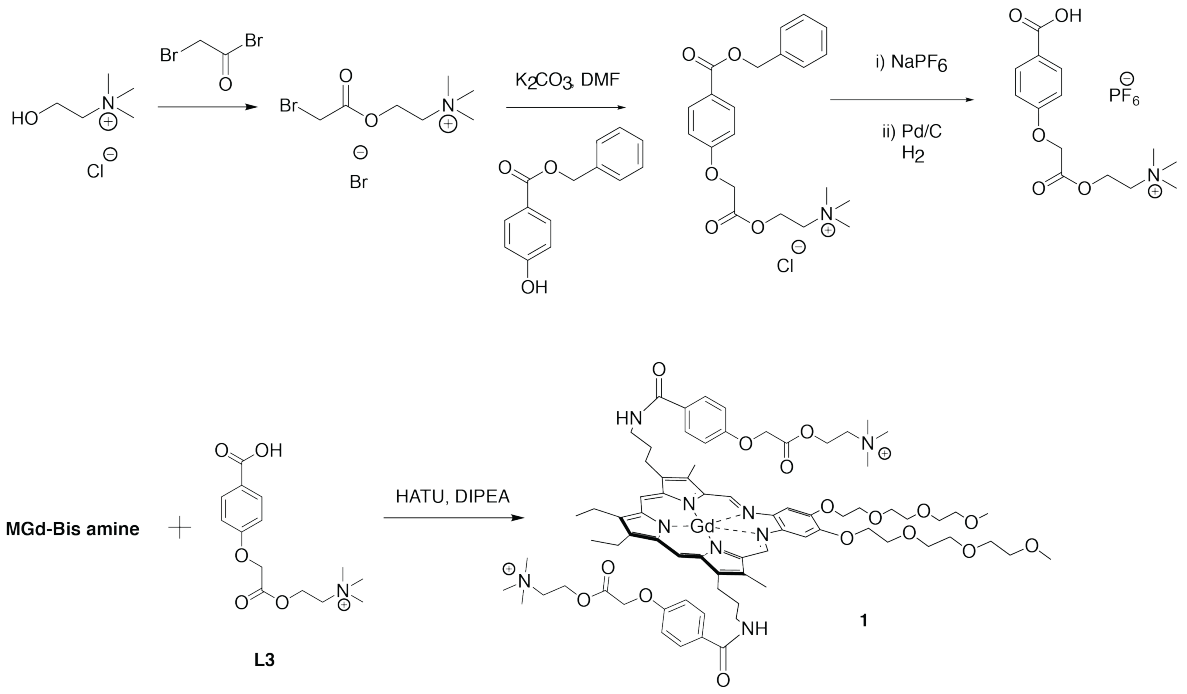

Figure S3: Synthesis of L3 and compound 1.

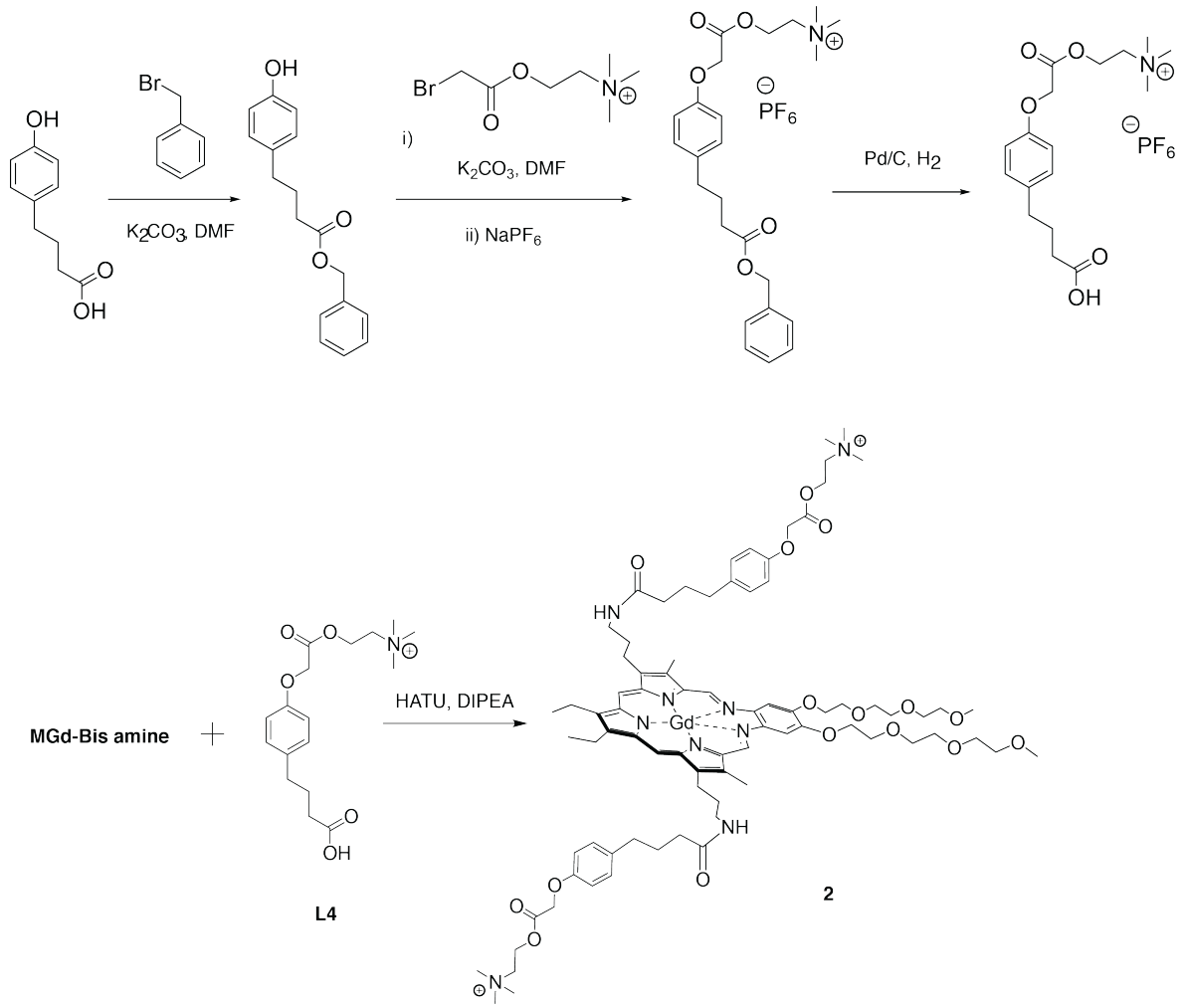

Figure S4: Synthesis of L4 and compound 2.

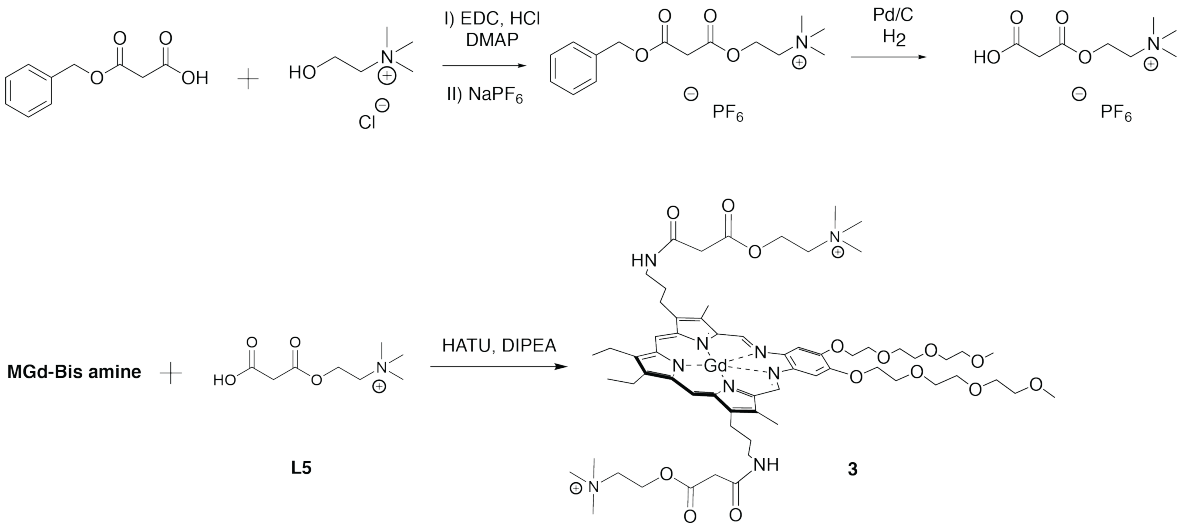

Figure S5: Synthesis of L5 and compound 3.

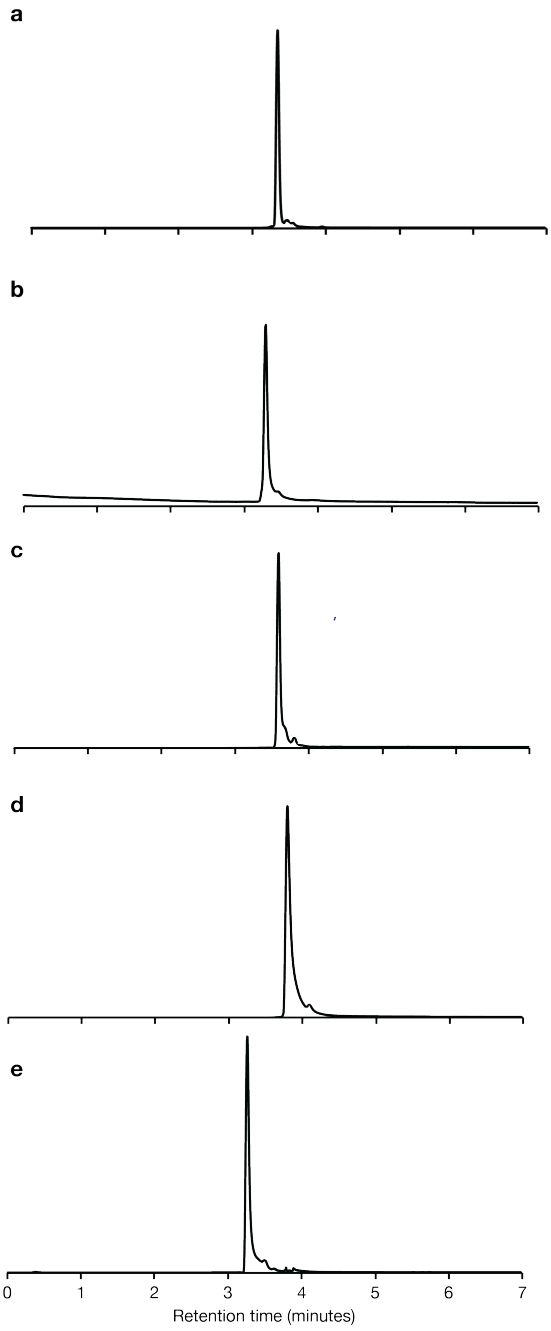

Figure S6: HPLC chromatograms of compounds.
(a) ChERT, (b) Control, C) Compound 1, (d) Compound 2, (e) Compound 3.

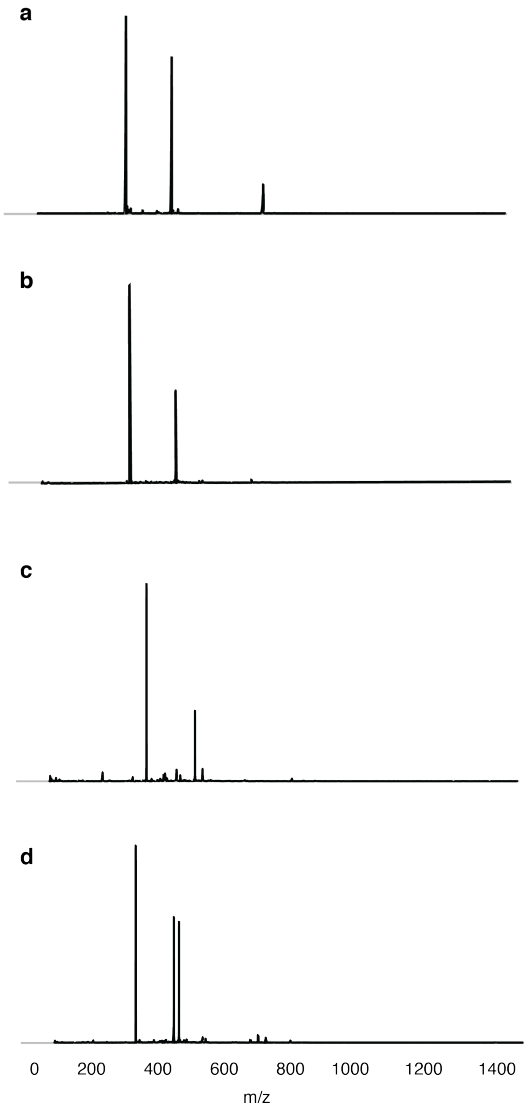

Figure S7: ESI-MS spectra of compounds.
(a) ChERT, (b) Control, C) Compound 1, (d) Compound 3.

HRMS of ChERT

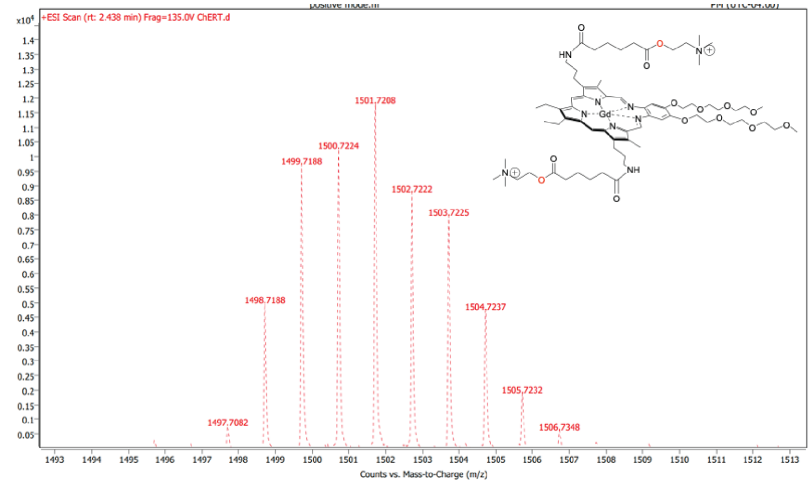

HRMS of intermediate

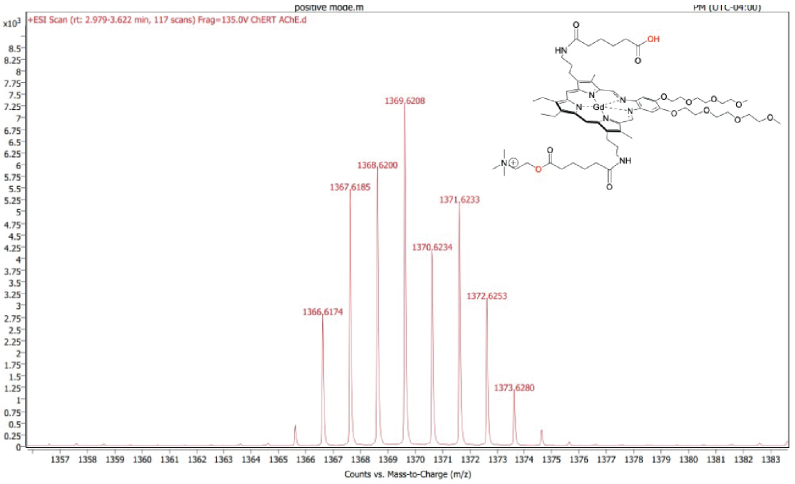

HRMS of product (M/2)

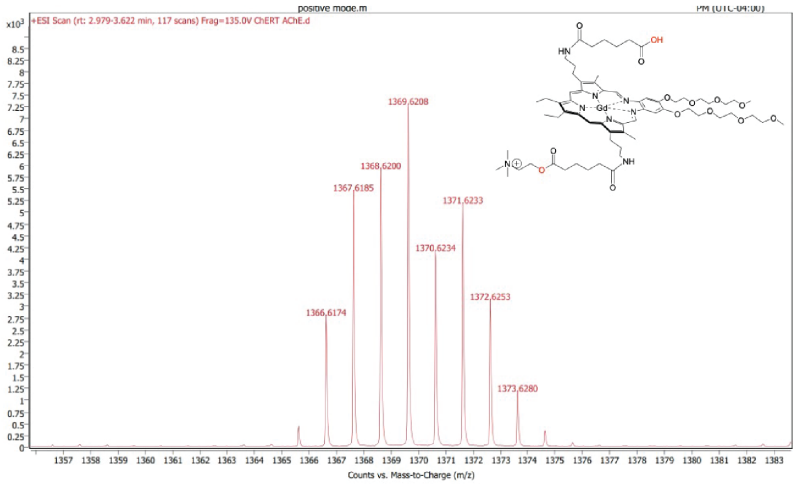

Figure S8: HR-MS of ChERT compound, intermediate, and product.

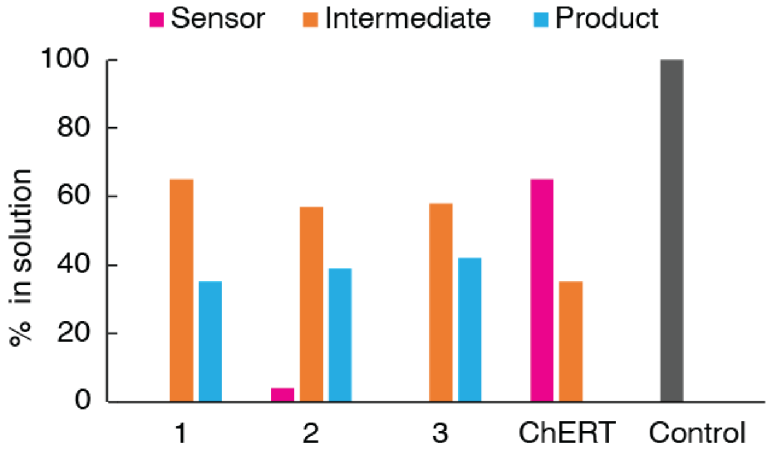

Figure S9: Self-hydrolysis pattern for library of sensors and control.
For each case, 100 μM compound was incubated in aCSF and 10 μM BSA for 2 h at 37 °C. Conversion was calculated from HPLC chromatogram area.

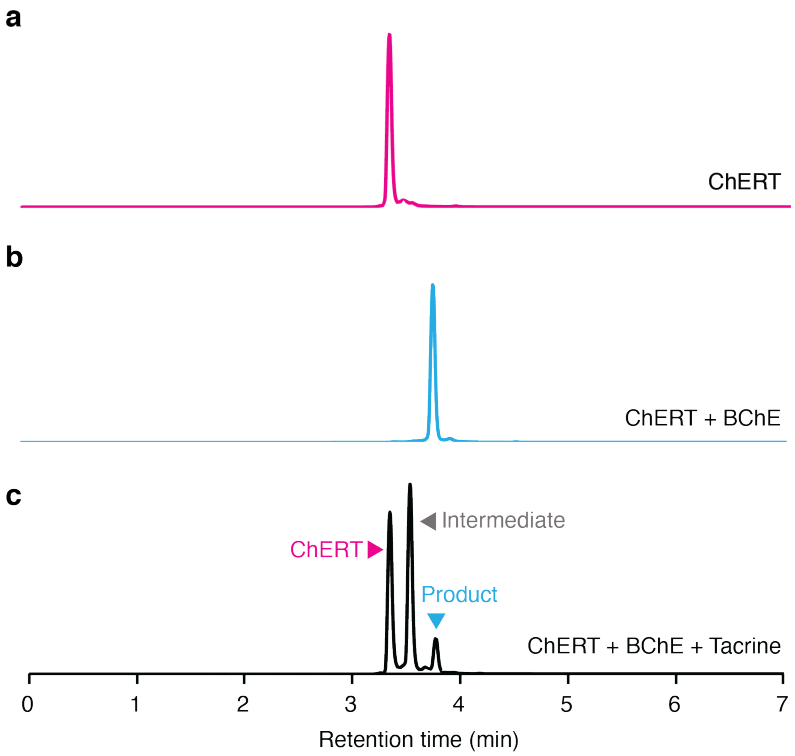

Figure S10: Enzymatic hydrolysis of ChERT can be restricted by using ChE inhibitor. (a) ChERT (100 μM), (b) ChERT with 1 U/ml BChE, and (c) ChERT with 1 U/ml BChE with tacrine (50 μM) in aCSF + 10 μM BSA incubated for 2 h at 37 °C

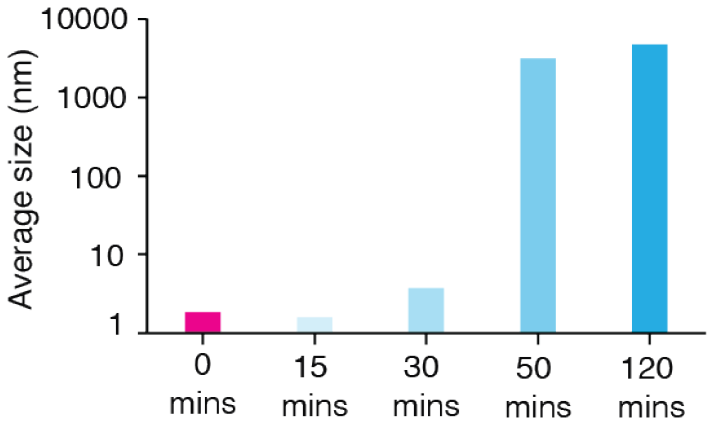

Figure S11: Time dependent DLS study of ChERT.
100 μM of ChERT was incubated with 1 U/ml BChE in aCSF + 10 uM BSA for 2 h at 37 ^{o}C.

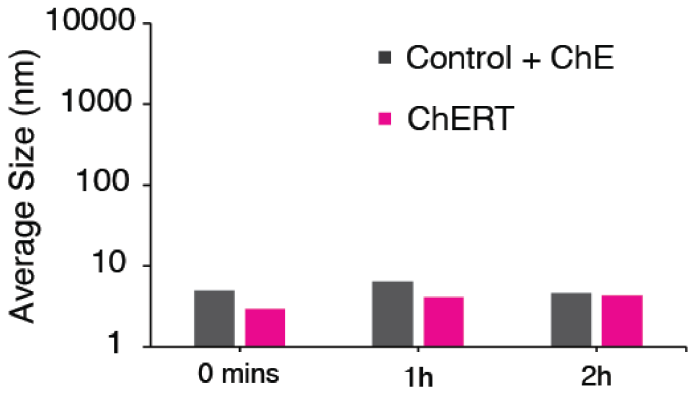

Figure S12: DLS studies with ChERT.
ChERT or control (100μM) compound in the absence of BChE (1 U/ml) or control in the presence of BChE showed no change in particle size over 2h of incubation at 37°C.

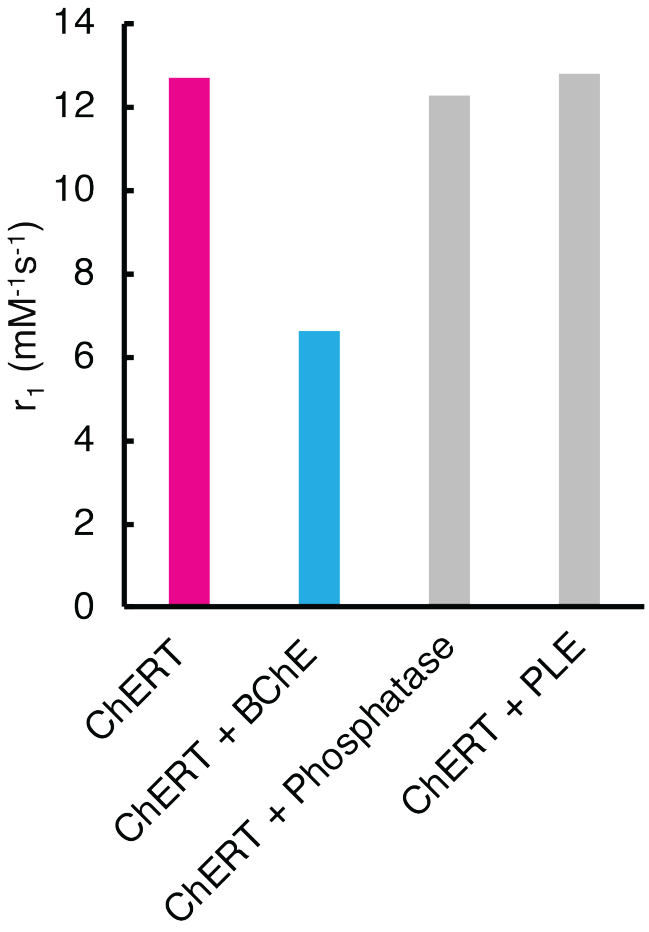

Figure S13: MRI relaxivity of ChERT in the presence of multiple enzymes. BChE (1.8 nM), alkaline phosphatase from human placenta (20 nM), and porcine liver esterase (20 nM) were incubated with 100 μM ChERT for 2h at 37°C.

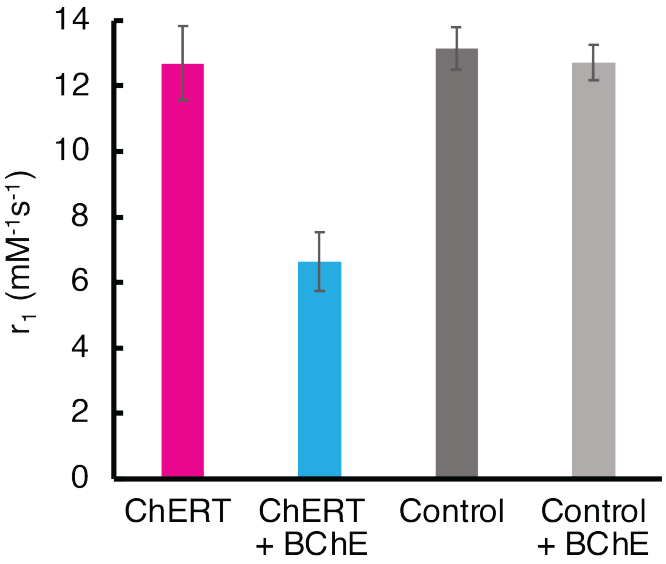

Figure S14: MRI relaxivity change of 100 μM ChERT or control compound. In the presence of 1 U/ml.

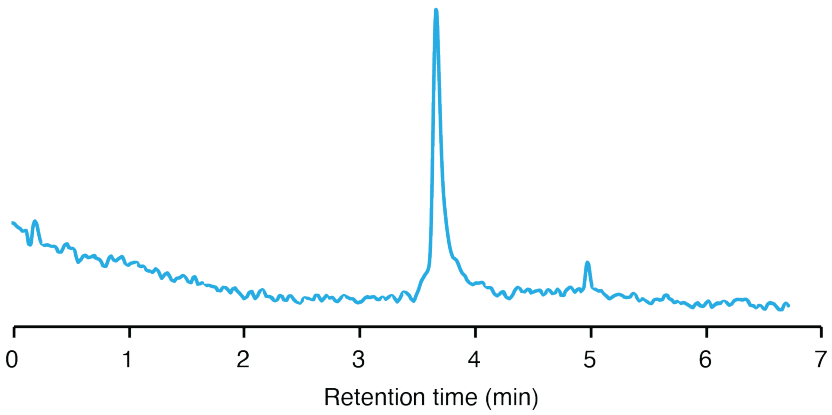

Figure S15: HPLC chromatogram from ChERT treated rat brain slice.

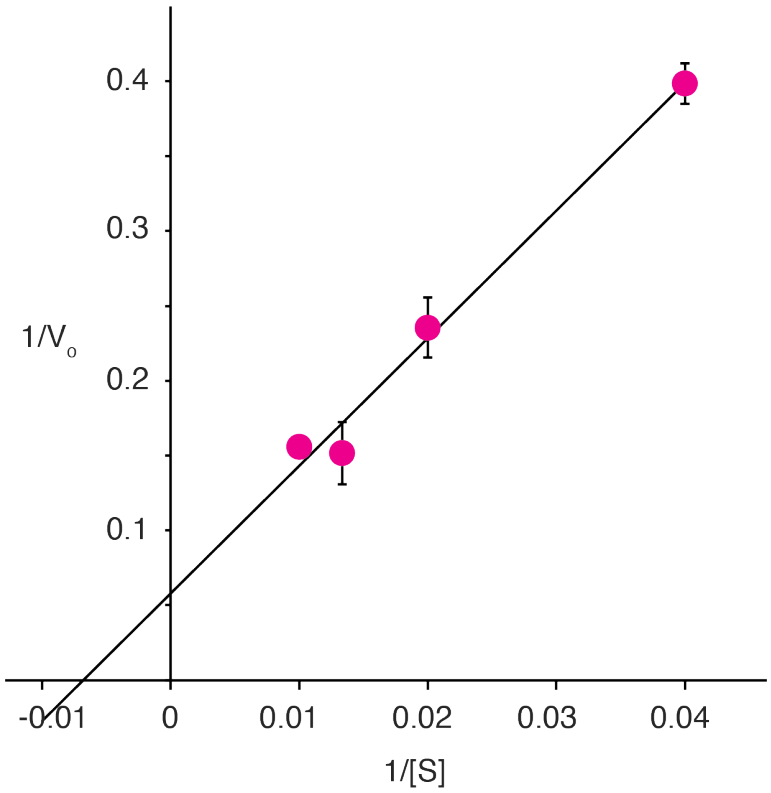

Figure S16: Lineweaver-burk plot of ChERT compound. V_{max} = 17.36 μM/min and K_m = 148 μM.

3.7 Supplementary Methods

Modified synthesis of MGd-Bis amine

Tex-OH [104] (400 mg, 0.458 mmol, 1 equiv.) was mixed with PPh_3 (360 mg, 3 equiv.) and phthalimide (202 mg, 3 equiv.) and kept under vacuum for 3 h. To this mixture was added 90 ml dry DCM. The resulting red solution was cooled over ice for about 15 minutes under Ar. Following this, DIAD (280 µL, 3 equiv.) was added to the solution dropwise. The reaction mixture was allowed to warm slowly to ambient temperature. Once confirmed of the completion of the reaction by LCMS, the solvent was removed under reduced pressure to obtain Tex-phthalimide. To the resulting residue, were added $Gd(OAc)_3.H_2O$ (dried overnight) (603 mg, 5 equiv.) and dry methanol (90 mL). The solution was stirred at 60° C for 3.5 h and the reaction progress was monitored using LCMS. Once completed, the solvent was evaporated under reduced pressure which resulted in obtaining MGd-phthalimide as a mixture and was further used without purification for the next step.

To the mixture containing MGd-phthalimide, 25 mL methanol and 20 mL methylamine were added. After 45 min of stirring, Ar was bubbled through the reaction mixture to remove excess methylamine. Next, the solution was cooled over ice and to that, acetic acid was added dropwise. Once the excess amine was quenched, the solution was poured into 300 mL aqueous 0.1 M ammonium acetate/0.1% acetic acid solution. Using a reverse phase C18 column, MGd-Bis amine was separated from the mixture using ACN:water (gradient from 10:90 to 30:70, the target elutes with 20:80 mixture). MGd-Bis amine solution was concentrated and lyophilized to obtain as dark green powder. Characterization matches previous literature [106]. Yield**:** 198 mg, 42%.

Synthesis of L1 and L2

6-(benzyloxy)-6-oxohexanoic acid (100 mg, 0.424 mmol, 1 equiv.) was mixed with choline chloride (for L1-Bz) (65 mg, 1.1 equiv.) or (2-Aminoethyl)trimethylammonium chloride hydrochloride (for L2-Bz) (64 mg, 1.1 equiv.) in 3 ml ACN. To that mixture

added EDC.HCl (243 mg, 3 equiv.) and DMAP (26 mg, 0.5 equiv.) and the reaction mixture was stirred for overnight. Once confirmed of the reaction completion using LCMS, the solvent was evaporated and the target compound was separated using a reverse phase C18 column (eluent solution - ACN:water, used gradient from 10:90 to 40:60, target products elute with 30:70). Following the concentration of the target compound, sodium hexafluorophosphate was added in excess to precipitate out L1-Bz or L2-Bz which was collected by Buchner funnel filtration. Yield: L1-Bz – 135 mg, 71%, L2-Bz – 148 mg, 77%.

L1-Bz - ^{1}H NMR (500 MHz, DMSO-d_6): 7.43 – 7.31 (m, 4H), 5.09 (s, 2H), 4.45 (dq, J = 5.0, 2.4 Hz, 2H), 3.69 – 3.62 (m, 2H), 3.11 (s, 9H), 2.38 (dddd, J = 10.1, 7.6, 4.3, 2.1 Hz, 4H), 1.58 (qt, J = 6.5, 3.6 Hz, 4H).

L1-Bz - ^{13}C NMR (500 MHz, DMSO-d_6): 173.08, 172.63, 136.71, 128.93, 128.50, 128.42, 65.85, 64.20, 58.21, 53.39, 33.55, 33.46, 24.27, 24.07.

L2-Bz - ^{1}H NMR (500 MHz, DMSO-d_6): 8.11 (t, 1H), 7.41 – 7.30 (m, 5H), 5.08 (s, 2H), 3.46 (m, 2H), 3.33 (m, 2H), 3.08 (s, 9H), 2.36 (dq, J = 6.8, 3.4 Hz, 2H), 2.11 (h, J = 3.0 Hz, 2H), 1.59 – 1.46 (m, J = 3.5 Hz, 4H).

L2-Bz - ^{13}C NMR (500 MHz, DMSO-d_6): 173.12, 172.99, 136.73, 128.92, 128.48, 128.39, 65.82, 64.27, 64.25, 64.22, 53.03, 53.00, 52.97, 35.27, 33.63, 33.39, 24.93, 24.48.

Once obtained, L1-Bz (60 mg) or L2-Bz (45 mg) was dispersed in ethyl acetate and to that solution added Pd/C (20% w/w equiv.). Followed by bubbling Ar for 15 mins, hydrogen was bubbled for overnight. Once reaction completion was confirmed by LCMS, Pd/C was separated using celite and the solution was evaporated to obtain L1 (Yield: 42 mg, 85%) or L2 as white powder (Yield: 32 mg, 87%).

L1 - ^{1}H NMR (500 MHz, DMSO-d_6): 4.45 (tt, J = 4.9, 2.4 Hz, 2H), 3.68 – 3.61 (m, 2H), 3.12 (s, 9H), 2.36 (t, J = 7.0 Hz, 2H), 2.22 (t, J = 6.9 Hz, 2H), 1.61 – 1.48 (m, 4H).

^{13}C NMR (500 MHz, DMSO-d_6): 174.80, 172.68, 64.21, 58.19, 53.39, 33.85, 33.55, 24.37, 24.20.

L2 - ^{1}H NMR (500 MHz, DMSO-d_6) 8.13 (t, J = 5.8 Hz, 1H), 3.46 (q, J = 6.4 Hz, 2H), 3.34 (d, J = 6.7 Hz, 2H), 3.08 (s, 9H), 2.20 (t, J = 6.8 Hz, 2H), 2.11 (t, J =

7.0 Hz, 2H), 1.56 – 1.43 (m, 4H).

^{13}C NMR (500 MHz, DMSO-d_6): 174.83, 173.04, 64.38, 53.15, 35.41, 33.88, 33.39, 25.07, 24.57.

ESI-MS: L1 – For $C_{11}H_{22}NO_4^+$ Exact mass: 232.15. Observed: 232.1, L2 - $C_{11}H_{23}N_2O_3^+$ Exact mass: 231.17, Observed: 231.1.

Synthesis of ChERT and control

MGd-Bis amine (30 mg, 0.026 mmol, 1 equiv.) and L1 (21 mg, 2.2 equiv.) or L2 (21 mg, 2.2 equiv.) were mixed with HATU (30 mg, 3 equiv.) and DIPEA (13 ul, 3 equiv.) in DMF and the reaction mixture was stirred overnight. Once the reaction is completed as confirmed by LCMS, solvent was evaporated. The reaction mixture was subjected to a reverse phase C18 column and the target green band was separated using ACN:water mixture (gradient from 10:90 to 30:70, target product elutes with 25:75 mixture) to obtain ChERT or Control as green powder. Yield: ChERT-19 mg, 42%; Control - 17 mg, 38%

HPLC: ChERT - R_f = 3.4 mins. Control – 3.35 mins.

ESI-MS: ChERT - For $C_{70}H_{106}GdN_9O_{14}^{2+}$ Exact mass = 1454.71, Observed: (M+2HCOO)/2 = 774.3, (M+HCOO)/3 = 500.5, M/4 = 364.0. Control - $C_{70}H_{106}GdN_{11}O_{12}^{2+}$ Exact mass = 1452.74, Observed: (M+HCOO)/3 = 499.4, M/4 = 363.4.

Synthesis of L3

Choline chloride (250 mg, 1.79 mmol, 1 equiv.) was added into 3 ml dry ACN and the mixture was cooled over an ice bath until the temperature reaches to 0-5 ^{o}C. To the cooled solution, added 2-bromoacetyl bromide (240 uL, 1.5 equiv.) and the mixture was stirred for 1-1.5 h. Upon formation of the product, the solvent was evaporated and DCM was added to precipitate out 2-(2-bromoacetoxy)-*N*,*N*,*N*-trimethylethan-1-aminium as white solid. Characterization of this solid matches previous literature. Yield: 380 mg, 70%.

2-(2-bromoacetoxy)-*N*,*N*,*N*-trimethylethan-1-aminium (50 mg, 0.165 mmol, 1 equiv) was mixed with benzyl 4-hydroxybenzoate (49 mg, 1.3 equiv.) and potassium carbon-

ate (35 mg, 1.5 equiv.) in 2 ml DMF. The reaction mixture was stirred overnight and following the completion of the reaction, solvent was evaporated and added 3 ml dry ACN. The slurry was then filtered through celite and the target compound was separated from the supernatant using a reverse phase C18 column (eluent solution - ACN:water, used gradient from 10:90 to 40:60, target product elutes with 30:70). Following the concentration of the target compound, sodium hexafluorophosphate was added in excess to precipitate out (x mg, 10 equiv.) to precipitate out L3-Bz as a white solid. Yield: 75 mg, 88%

^{1}H NMR (500 MHz, DMSO-d_6): ^{1}H NMR (500 MHz, DMSO) 8.00 – 7.94 (m, 2H), 7.50 – 7.32 (m, 5H), 7.12 – 7.07 (m, 2H), 5.33 (s, 2H), 4.96 (s, 2H), 4.61 – 4.54 (m, 2H), 3.72 – 3.65 (m, 2H), 3.10 (s, 9H).

^{13}C NMR (500 MHz, DMSO-d_6): 168.28, 165.57, 161.87, 136.76, 131.79, 129.00, 128.56, 128.38, 123.10, 115.20, 66.38, 65.13, 64.00, 59.29, 53.44.

Once obtained, L3-Bz (200 mg, 1 equiv.) was dispersed in ethyl acetate and to that solution added Pd/C (20% w/w equiv.). Followed by bubbling Ar for 15 mins, hydrogen was bubbled for overnight. Once reaction completion was confirmed by LCMS, Pd/C was separated using celite and the solution was evaporated to obtain L3 as white powder. Yield: 148 mg, 82%.

^{1}H NMR (500 MHz, DMSO-d_6): 12.72 (s, 1H), 7.93 – 7.88 (m, 2H), 7.08 – 7.03 (m, 2H), 4.95 (s, 2H), 4.60 – 4.55 (m, 2H), 3.73 – 3.66 (m, 2H), 3.10 (s, 9H).

^{13}C NMR (500 MHz, DMSO-d_6): 168.38, 167.32, 161.46, 131.78, 124.30, 114.92, 65.09, 64.01, 59.14, 53.42.

ESI-MS: For $C_{14}H_{20}NO_5^+$ Exact mass: 282.13. Observed: 282.1.

Synthesis of 1

MGd-Bis amine (30 mg, 0.026 mmol, 1 equiv.) and L3 (24 mg, 2.2 equiv.) were mixed with HATU (30 mg, 3 equiv.) and DIPEA (13 ul, 3 equiv.) in DMF and the reaction mixture was stirred overnight. Once the reaction is completed as confirmed by LCMS, solvent was evaporated. The reaction mixture was subjected to a reverse phase C18 column and the target green band was separated using ACN:water mixture

(gradient from 10:90 to 40:60, target product elutes with 25:75 to 30:70 mixture) to obtain **1** as green powder. Yield:

HPLC: R_f = 3.65 mins.

ESI-MS: For $C_{76}H_{104}GdN_9O_{16}^{2+}$ Exact mass: 1556.68. Observed: (M+HCOO)/3 = 533.8, M/4 = 389.1.

Synthesis of L4

4-(4-hydroxyphenyl)butanoic acid (170 mg, 0.944 mmol, 1 equiv.) was mixed with potassium carbonate (160 mg, 1.2 equiv.) in 3 ml DMF and to the mixture added benzyl bromide (150 uL, 1.2 equiv.). The mixture was stirred overnight to obtain benzyl 4-(4-hydroxyphenyl)butanoate as a colorless liquid which was separated from potassium carbonate through celite filtration. Characterization of the product matches previous literature. (yield: 218 mg, 86%).

2-(2-bromoacetoxy)-*N*,*N*,*N*-trimethylethan-1-aminium (102 mg, 1.2 equiv) was mixed with benzyl 4-(4-hydroxyphenyl)butanoate (75 mg, 0.277 mmol, 1 equiv.) and potassium carbonate (46 mg, 1.2 equiv.) in 2 ml DMF. The reaction mixture was stirred overnight and following the completion of the reaction, solvent was evaporated and added 3 ml dry ACN. The slurry was then filtered through celite and the target compound was separated from the supernatant using a reverse phase C18 column (eluent solution - ACN:water, used gradient from 10:90 to 40:60, target product elutes with 35:65. To that solution, added excess sodium hexafluorophosphate (1 g, 6 equiv.). The anion-exchanged L4-Bz solution was separated from excess salt and collected using another C18 column as a colorless liquid. Yield: 93 mg, 60%

^{1}H NMR (500 MHz, DMSO-d_6): 7.41 – 7.32 (m, 5H), 7.14 – 7.07 (m, 2H), 6.89 – 6.83 (m, 2H), 5.09 (s, 2H), 4.80 (s, 2H), 4.60 – 4.52 (m, 2H), 3.09 (s, 9H), 2.54 (s, 2H), 2.35 (t, J = 7.4 Hz, 2H), 1.81 (p, J = 7.5 Hz, 2H).

^{13}C NMR (500 MHz, DMSO-d_6): 173.05, 168.87, 156.22, 136.73, 134.67, 129.78, 128.92, 128.50, 114.90, 65.86, 65.10, 64.04, 58.96, 53.41, 33.82, 33.32, 26.97.

Once obtained, L4-Bz (43 mg, 1 equiv.) was dispersed in ethyl acetate and to that solution added Pd/C (20% w/w equiv.). Followed by bubbling Ar for 15 mins, hydrogen

was bubbled for overnight. Once reaction completion was confirmed by LCMS, Pd/C was separated using celite and the solution was evaporated to obtain L4 as white powder. Yield: 33 mg, 92%.

^{1}H NMR (500 MHz, DMSO-d_6): 7.16 – 7.08 (m, 2H), 6.94 – 6.81 (m, 2H), 4.80 (s, 2H), 4.60 – 4.53 (m, 2H), 3.72 – 3.64 (m, 2H), 3.10 (s, 9H), 2.54 (d, J = 7.6 Hz, 2H), 2.20 (t, J = 7.4 Hz, 2H), 1.76 (p, J = 7.5 Hz, 2H).

^{13}C NMR (500 MHz, DMSO-d_6): 174.79, 168.87, 156.18, 134.88, 129.77, 114.88, 65.08, 64.05, 58.94, 53.38, 33.93, 33.47, 26.97.

ESI-MS: For $C_{17}H_{26}NO_5^+$ Exact mass: 324.18. Observed: 324.1.

Synthesis of 2

MGd-Bis amine (25 mg, 0.022 mmol, 1 equiv.) and L4 (22 mg, 2.2 equiv.) were mixed with HATU (25 mg, 3 equiv.) and DIPEA (11 ul, 3 equiv.) in DMF and the reaction mixture was stirred overnight. Once the reaction is completed as confirmed by LCMS, solvent was evaporated. The reaction mixture was subjected to a reverse phase C18 column and the target green band was separated using ACN:water mixture (gradient from 10:90 to 40:60, target product elutes with 35:65 mixture) to obtain **2** as green powder. Yield: 17 mg, 40%.

HPLC: R_f = 3.85 mins

Synthesis of L5

3-(benzyloxy)-3-oxopropanoic acid (100 mg, 93 uL, 0.515 mmol, 1 equiv.) was mixed with overnight dried choline chloride (57 mg, 0.8 equiv.) in 3 ml ACN. To that mixture added EDC.HCl (198 mg, 2 equiv.) and DMAP (31 mg, 0.5 equiv.) and the reaction mixture was stirred for overnight. Once confirmed of the reaction completion using LCMS, the solvent was evaporated and the target compound was separated using a reverse phase C18 column (eluent solution - ACN:water, used gradient from 10:90 to 30:70, target product elutes with 15:85). Following the concentration of the target compound, sodium hexafluorophosphate was added to perform anion exchange. The final product was collected using C18 followed by evaporation of the solvent and

lyophilization to obtain L5-Bz. Yield: 89 mg, 39%.

^{1}H NMR (500 MHz, DMSO-d_6): 7.51 – 7.29 (m, 5H), 5.17 (s, 2H), 4.52 (dp, J = 4.8, 2.4 Hz, 2H), 3.71 – 3.61 (m, 4H), 3.09 (s, 9H).

^{13}C NMR (500 MHz, DMSO-d_6): 166.69, 166.46, 136.04, 128.97, 128.73, 128.57, 66.92, 63.92, 59.24, 53.43, 53.40, 53.37, 41.42.

Once obtained, L5-Bz (40 mg, 1 equiv.) was dispersed in ethyl acetate and to that solution added Pd/C (20% w/w equiv.). Followed by bubbling Ar for 15 mins, hydrogen was bubbled for overnight. Once reaction completion was confirmed by LCMS, Pd/C was separated using celite and the solution was evaporated to obtain L5 as colorless liquid. Yield: 28 mg, 92%.

^{1}H NMR (500 MHz, DMSO-d_6): 4.51 (d, J = 5.8 Hz, 2H), 3.72 – 3.64 (m, 2H), 3.45 (s, 2H), 3.12 (s, 9H).

^{13}C NMR (500 MHz, DMSO-d_6): 168.31, 166.97, 63.95, 58.96, 53.47, 42.08.

ESI-MS: For $C_8H_{16}NO_4^+$ Exact mass: 190.11. Observed: 190.1.

Synthesis of 3

MGd-Bis amine (20 mg, 0.017 mmol, 1 equiv.) and L5 (13 mg, 2.2 equiv.) were mixed with HATU (20 mg, 3 equiv.) and DIPEA (9 ul, 3 equiv.) in DMF and the reaction mixture was stirred overnight. Once the reaction is completed as confirmed by LCMS, solvent was evaporated. The reaction mixture was subjected to a reverse phase C18 column and the target green band was separated using ACN:water mixture (gradient from 10:90 to 40:60, target product elutes with 20:80 mixture) to obtain **3** as green powder. Yield: 10 mg, 35%.

HPLC: R_f = 3.25 mins

ESI-MS: For $C_{64}H_{96}GdN_9O_{14}^{2+}$ Exact mass: 1372.63. Observed mass: (M+HCOO)/3 = 472.3, M/4 = 343.1.

Chapter 4

Investigating interoception in opioid dependence

4.1 Abstract

Brain-body interactions modulate the response to drugs of abuse. Drug consumption and withdrawal elicit dramatic peripheral responses with representations in brain circuitry. To characterize the role of interoceptive processes in brain dynamics associated with substance use disorders, we applied population-level neuroimaging techniques, targeted neural manipulations, and circuit-level activity measurements in rats undergoing treatment with the synthetic opioid fentanyl. Using functional magnetic resonance imaging (fMRI), we characterized activity correlations among brain regions during acute and chronic fentanyl exposure, as well as during naloxone-precipitated withdrawal. We identified increased functional connectivity in a broad network including insular cortex, striatum, and nucleus accumbens that followed acute fentanyl administration, subsided during chronic exposure, but was then restored with greater amplitude during withdrawal. To investigate the causal role of interoceptive brain regions in these phenotypes, we examined how fMRI results are affected by pharmacological inactivation of the anterior insula using a paramagnetic version of the $GABA_A$ agonist muscimol. Preliminary data suggest that this treatment blocks the increased functional connectivity elicited by fentanyl dosing. To test whether interregional neural activity correlations affected by insular inactivation reflect patterns of direct information flow at the insula, we performed targeted injections of an inhibitory DREADD bilaterally in the anterior insular cortices. Together, our work suggests a prominent role for the insular cortex and its associated interoceptive functions in mediating brain-wide changes arising from fentanyl use and withdrawal.

4.2 Introduction

Interoception is the perception of bodily state [107]. It encompassess experiences such as one's ability to perceive heartbeats, experience thirst and hunger, and feel pain. It is thought that the integration of both interoceptive and exteroceptive cues leads to behavioral outcomes [108]. One theory is that interoceptive processes influence behavior that pushes an organism towards a homeostatic state. Aberrant interoceptive processing can thus lead to an altered behavior state. One way in which this relationship may develop is through the connection between interoceptive cues and activity in brain regions canonically related to reward processing. For instance, gastric stimulation via the vagal nerve in obese patients induces activity in the orbitofrontal cortex and striatum [109]. This extends to other aberrant forms of reward processing such as in drug addiction [110].

In human patients, interoceptive perturbations in subjects with substance use disorders (SUDs) are reflected in abnormal patterns of hemodynamic response in the anterior insula. The insular cortex is though to be a key mediator of interoceptive processing . This applies to multiple substances of abuse including nicotine, cocaine, alcohol, and opioids [83, 111]. These human findings are reflected in rodent studies. In a model of alcohol use disorder, researchers have identified chemogenetic manipulation in the anterior insula as a modulator of alcohol consumption [112–114]. In opioid use disorder, activation has been shown to reverse deficits induced by heroin self administration in rats [115]. After extinction, self-administering rats experiencing inactivation of the insular cortex have increased cue reinstatement [116].

Understanding the role of interoception in addiction requires us to consider the nature of addiction itself. In a medical context, addiction is referred to as substance used disorder (SUD). According to the DSM-5, one must exhibit two or more criteria including but not limited to: an increased tolerance for the substance, repeated attempts to quit or control use, and physical and psychological problems related to use [117]. The behavior of substance abuse occurs in three stages. In the first phase there is intoxication by the substance in which regions such as the ventral tegmental area

(VTA) and ventral striatum are heavily implicated to be involved. This is followed by a withdrawal phase with associations to structures such as the amygdala. Finally, there is a period of craving that especially engages cortical regions [118]. The interplay of these regions and the ways in which plasticity emerges from dysfunction in the mesolimbic dopamine system is still being fully elucidated.

While substance use disorder produces a combination of psychological and somatic symptoms, the disorder is often conceptualized in the framework of cognitive reward processing and motivation. However, peripheral symptoms and interoceptive processing of alterations in the viscera are implicit to these cycles of abuse [111]. Opioid use disorder (OUD), in particular, is of interest as it emerges from the engagement of receptors in both the central and peripheral system. Besides cognitive effects, the drug is paired with peripheral analgesia. Following chronic use, withdrawal induces strong somatic symptoms [58, 119]. In analyzing historical scientific literature, we see an attention to the physical symptoms of opioid addiction [120]. In 1942, a surgeon working for the United States Public Health Service published a clinical study of prisoners transitioning from a state of active opiate addiction, to withdrawal, and finally, recovery [121]. The nature of the prison environment controlled several variables related to caloric access and access to the substance of abuse. Measurements such as weight, caloric intake, rectal temperature, venous blood composition, and blood pressure were all taken into account over the course of 9 months. A few major findings emerged from the data including: (1) While in active opiate addiction, physical function "while biologically adequate, is incomplete." The subjects experienced decreased body weight and elevated body temperature among other symptoms. (2) Metabolism even 9 months into recovery is altered as the "the basal metabolic rate of the recovered addict is subnormal." These findings are still relevant in modern medical practice as treatment for opioid use disorder often involves mediating withdrawal symptoms through a tapering of -opioid agonists such as methadone and buprenorphine [119]. We understand the symptoms to include excessive sweating, tremors, teeth chatter, gastrointestinal distress, fever, and even anorexia. However, 80 years later, we have failed to bridge the heavy focus on affective state with this somatic dysfunction present in OUD. How

peripheral physiological response modulates the CNS in opioid dependence and vice versa likely contributes to this viscous cycle of abuse.

In order to understand this relationship of brain and body physiology in opioid dependence, we sought to investigate the cortical hub of interoceptive processing, the insular cortex. We chose to study fentanyl as it is a highly potent opioid. It also has major public health implications as the percentage of drug overdoses in the United States attributed to fentanyl increased from 7% to nearly 65% of all cases between 2010 to 2021 [122]. We hypothesized that brain activity changes during withdrawal depend on insular function and that manipulations to the insula would tend to normalize both drug-dependent behavioral and brain phenotypes during fentanyl exposure and withdrawal.

To test this hypothesis, we performed functional MRI (fMRI) of rats during administration of the synthetic opioid fentanyl. In particular, we examined functional connectivity. Functional connectivity is a measure of how anatomically defined brain regions share temporally dependent patterns of neuronal activation [123]. It is a particularly valuable approach as it allows us to understand how networks of brain regions are functionally coupled to specific brain states [124]. We then employed molecular tools to inhibit insular activity during intoxication and withdrawal. This revealed the insula's role in mediating striatal connectivity. We paired our findings of altered functional connectivity with behavioral tests to assess the somatic symptoms present in these conditions.

4.3 Results

4.3.1 Acute exposure to fentanyl in the ventral anterior insular cortex and striatum.

In order to assess the impact of acute exposure to fentanyl on functional brain connectivity, we performed functional MRI on Sprague-Dawley male rats lacking any previous exposure to opioids. Throughout scanning, rats were kept under an anesthetic regimen of intraperitoneal (IP) dexmedetomidine and a low level of isoflurane in oxygen-enriched air. Previous studies have indicated that this regimen maintains activity of the rodent default mode network (DMN) as well as response to sensory cues [125–127]. We verified sensory responsiveness in our rats by assessing visual response to a flashing light stimulus under this light anesthesia (Supplementary Figure 1). We performed a one hour echo-planar-imaging (EPI) scan in which a rat experienced a 20 minutes baseline period followed by IP injection of 10 ug/kg fentanyl and a subsequent 40 minute post-injection time period (Figure 1a).

For each individual rat, we assessed the functional connectivity among regions of interest. These regions were selected due to their prevalence in reward circuitry as well as paradigms of opioid use [128–132]. To quantify these relationships, Pearson correlation coefficients were computed between a regions of interest and all other voxels in the brain. Fischer z-transformation was to transform the correlation coefficient in a normally-distributed space. A difference matrix of the resultant z-scores post vs. pre fentanyl injection was computed for n=6 rats (Figure 1b). Increased connectivity was observed among regions previously implicated as undergoing increased fMRI signal change in rats exposed to the less potent opioid, heroin. This includes the striatum, frontal cortex, and cingulate cortex [133]. More correlation was observed between the orbitofrontal cortex and nucleus accumbens (p=0.0101), the prelimbic cortex and orbitofrontal cortex (p=0.0310, Figure 1b). Additionally, increased connectivity was observed between the anterior insula and striatal subregions. This included the caudate putamen (p= 0.0309) as well as the nucleus accumbens (p=0.0130, Figure 1c, d).

4.3.2 Neural correlates and somatic symptoms of pharmacologically-induced withdrawal

We next exposed rats to chronic fentanyl exposure followed by pharmacologically precipitated withdrawal. Previous literature has shown that after chronic exposure to opioids, the administration of naloxone will induce physical signs of withdrawal [134, 135]. Our paradigm involved daily injections of fentanyl ranging from 10 to 50 ug/kg over the course of five days. On day 6, a dose of 50 ug/kg fentanyl was given 90 minutes before a one hour EPI in which 10 mg/kg of naloxone was given 20 minutes into the scan. Just as with our acute fentanyl imaging, we waited 45 minutes after anesthetic induction before performing functional scanning (Figure 2a).

The correlation matrix reveals significance between the anterior insula and several regions previously implicated in rewarding and aversive pathways including the VTA (p=0.0064), substantia nigra (p=0.0065), and lateral habenula (p=0.0297, Figure 2b, c) [136]. Independent of the insular cortex, it is worth noting that connectivity between the caudate putamen and nucleus accumbens consistently decreased across rats (p=0.0075 Figure 2b, c).

In a separate cohort of rats, we tested the behavioral response to naloxone-induced withdrawal. Just as for the imaging experiments, rats were given increasing doses of fentanyl over 5 days before assessing withdrawal on day 6. As in the imaging session, we waited 90 minutes after the fentanyl dose to administer 10 mg/kg of naloxone. Compared to a control chronically dosed with saline, we saw increased levels of teeth chattering, writhing, ptosis, salivation, and fecal boli. This matched reported symptoms of rat models of opioid withdrawal in the literature [137]. While some symptoms presented variably across rats, all rats showed an increase in bouts of teeth chattering and quantities of fecal boli as compared to the control (Figure 2d, p=0.058, $5.7\text{x}10^{-4}$).

4.3.3 Disruption of insula alters the neural circuitry of reward

We hypothesized that given in the insula's role in mediateing physiological processing, it may play a role in mediating engagemetn with the reward system. To explore the impact of the insular cortex in modulating reward pathways upon acute opioid exposure, we used Paramus, a version of the $GABA_A$ agonist muscimol that is conjugated to the paramagnetic contrast agent (Figure 3a) [65]. This allows us to use T_1-weighted MRI imaging to directly visualize the spread of the agent post-injection (Figure 3b). After a unilateral injection of the agent, we mapped the correlation to both ipsilateral and contralateral regions of interest (Figure 3c). Correlation between orbitofrontal cortex and nucleus accumbens, as well as the orbital frontal cortex and prelimbic cortex were no longer significant ($p>0.05$). Furthermore, the anterior insula and striatal subregions on the side contralateral to injection show a lack of significant correlation (vIns-NAc $p=0.9620$, vIns-CPu $p=0.243$, Figure 3d). This suggests that the anterior insular cortex is mediating connections in the reward pathway.

4.3.4 Inhibiting the insular cortex produces a divergent profile of withdrawal

Given the impact of inhibiting the anterior insula during opioid intoxication, we hypothesized that inhibition of the anterior insular cortex would similarly disrupt striatal functional connectivity in withdrawal. We aimed to test this in a cell-type specific manner. To achieve this we bilaterally injected inhibitory Designer Receptors Exclusively Activated by Designer Drugs (hM4Di-DREADDS) in the anterior insula. The constructs were packaged in an AAV9 and expressed under the control of the neuronal-specific Syn promoter [66, 138]. Three weeks post-injection, we repeated our previous paradigm of chronic fentanyl administration. On the day of scanning we injected CNO (10 mg/kg I.P.) and induced naloxone-precipitated withdrawal in the scanner (Figure 4a).

What we found was that indeed, striatal connectivity was disrupted. In the unaltered withdrawal condition, the subregions of the striatum showed significantly de-

creased connectivity, but when we inhibited neuronal activity in the insular cortex, this significant decrease is abolished (Figure 4b, c). In fact, the caudate instead showed significant increases in connectivity with the amygdala (p=0.0280) and substantia nigra (p=0.0057) while the nucleus accumbens showed increased connectivity with the orbital frontal nucleus (p=0.0355).

In a separate cohort of DREADD implanted rats, we administered CNO (10 mg/kg I.P.), waited 30 minutes and tested the behavioral response to naloxone-induced withdrawal. As with the uninjected rats, the amount of teeth chattering increases post-naloxone injection. However, the phenotype of excessive fecal boli during withdrawal is vastly reduced close under anterior insular inhibition (Figure 4d).

4.4 Conclusion

These results implicate the anterior insula as a mediator of reward-related response in opioid-dependence, particularly among striatal sub-regions. Previous literature has shown there is structural connection between these regions as a subset of anatomical projections from the striatum localize to the anterior insula [139]. In addition, previous neuroimaging studies of reward have shown significant correlation of the ventral stratium and dorsal striatum to the insular cortex [140, 141]. The altered connectivity in opioid abuse is supported by evidence in both humans and rats that chronic opioid exposure and withdrawal leads to neuroadaptation of dopamine release in the dorsal and ventral striatum [142, 143]. Future directions of this work include examining other regions known to mediate brain-body interactions. Of particular interest are regions in the brain stem known to receive viscerosensory information and maintain homeostatic function. This includes the area postrema and nucleus of the solitary tract (NTS) [144]. These regions are dense in μ-opioid receptor [145]. However, their role in opioid dependence and withdrawal are less understood. Another condition to consider is investigation of these functional relationships within a self-administration paradigm [146]. In this model, we can capture drug seeking and voluntary abstinence. This would allows us to go beyond opioid dependence and understand brain-body physiology in

drug-seeking and voluntary abstinence behavior.

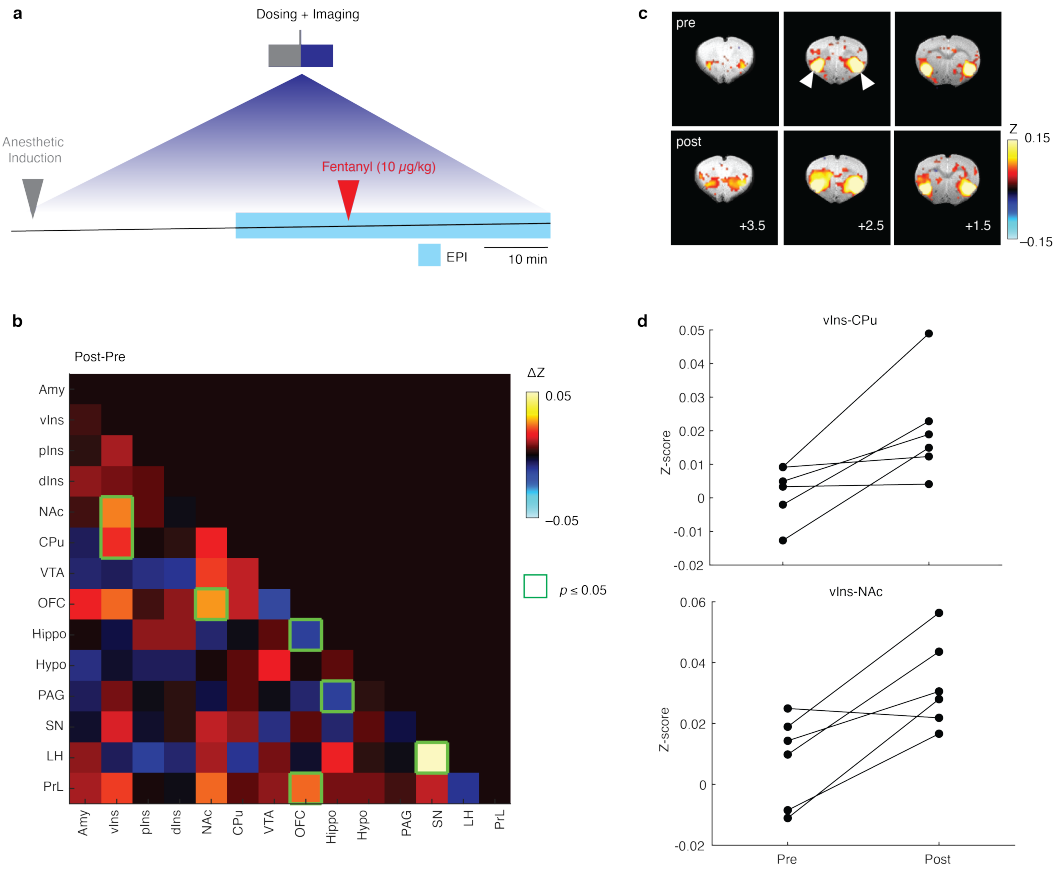

Figure 4.1: **Acute exposure to fentanyl in a naive rat induces increased functional connectivity between the ventral anterior cortex and striatum.** (a) Diagram of imaging paradigm. Rats were anesthetized. After 45 minutes (allowing the rat to fully stabilize to the regimen), EPI scanning was performed over a 1 hour period. A 10 µg/mg dose of fentanyl was given I.P. 20 minutes into the scan. (b) A difference matrix of the average Z score among ROIs 20-40 minutes after fentanyl dosing versus the 20 minute period before administration (n=6, p-values based on a two-tailed t-test). ROIs include the amygdala (Amy), ventral anterior insula (vIns), posterior insula (pIns), dorsal anterior insula (dIns), nucleus accumbens (NAc), ventral tegmental area (VTA), orbitofrontal cortex (OFC), hippocampus (Hippo), hypothalamus (Hypo), periaqueductal gray (PAG), substantia nigra (SN), lateral habenula (LH), and prelimbic cortex (PrL). (c) Seed-based functional connectivity of the bilateral anterior insular cortices before and after administration of fentanyl at +3.5, +2.5, and +1.5 mm anterior to bregma. (d) Dot plots showing the increased connectivity between the ventral insula and striatal regions (t-test, vIns-CPu p= 0.0309, vIns-NAc p=0.0130).

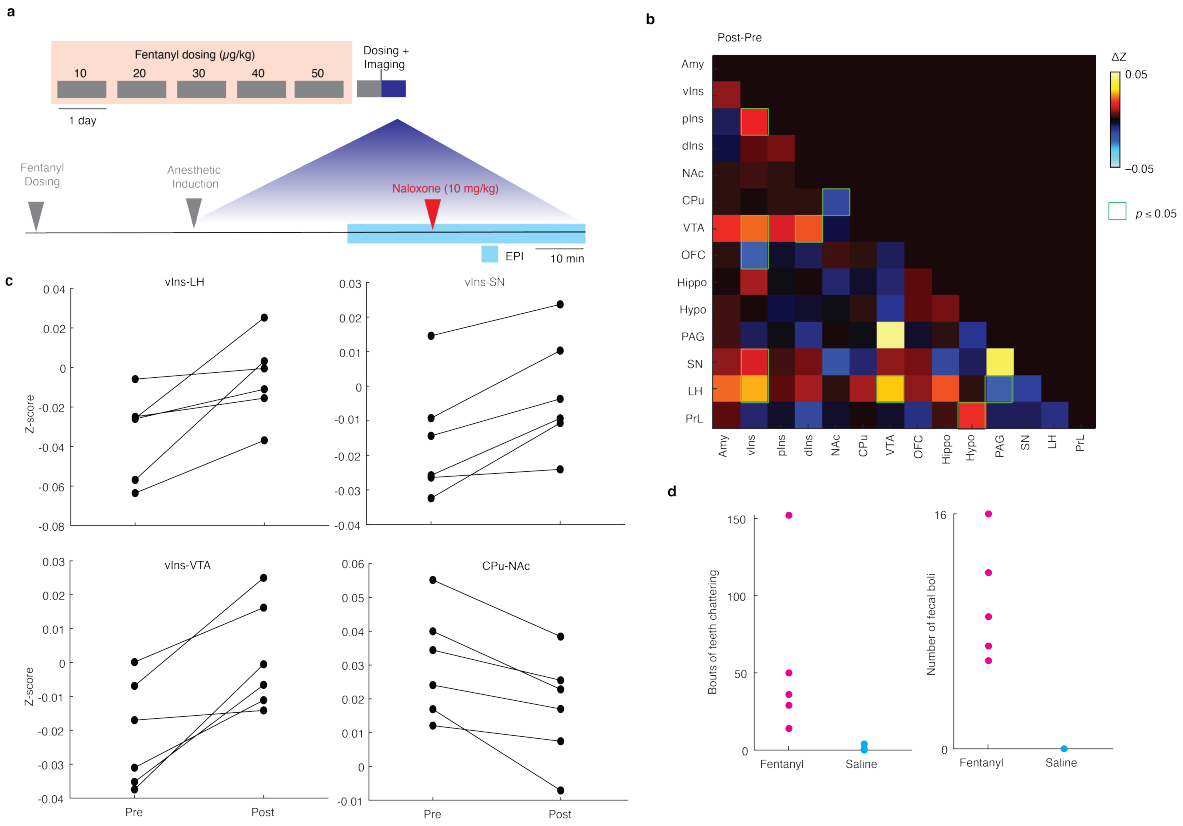

Figure 4.2: **Neural correlates and somatic symptoms of pharmacologically-induced withdrawal.**

(a) Diagram of imaging paradigm. Rats were dosed with fentanyl 90 minutes before the EPI. A 10 mg/mg dose of naloxone was given I.P. 20 minutes into the scan. (b) A difference matrix of the average Z score among ROIs 20-40 minutes after naloxone dosing versus the 20 minute period before administration (n=6, p-values based on a two-tailed one sample t-test). (c) Dot plots showing the increased connectivity between regions of interest: ventral insula and lateral habenula (p=0.0297), ventral insula and substantia nigra (p=0.0065) ventral insula and VTA (p=0.0064), and caudate putamen and nucleus accumbens (p=0.0075). (d) Quantification of somatic symptoms of naloxone-precipitated withdrawal in chronically dosed rats. Bouts of teeth chattering in rats chronically dosed with fentanyl versus saline show increased chattering in the fentanyl rats albeit statistically not significant (p=0.058). The number of fecal boli in fentanyl-dosed rats is consistently higher than in the saline condition ($p=5.7\text{x}10^{-4}$).

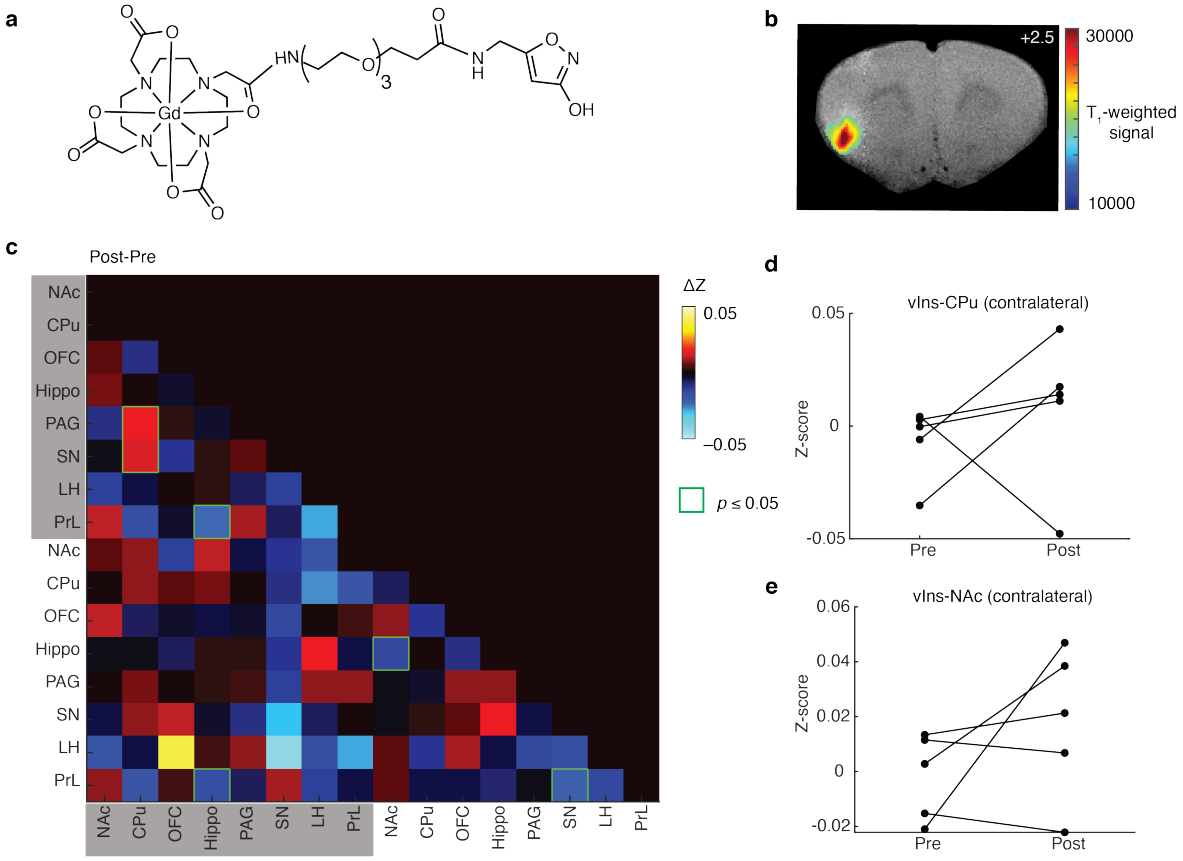

Figure 4.3: **Disruption of insula alters the neural circuitry of reward.** (a) Paramus is the conjugatiotion of a Gd-DOTA molecule and muscimol (adapted from [65]. (b) Representative image of the increased T_1-weighted signal following local injection of paramus in the left anterior insular cortex. (C) A difference matrix of the average Z score among ROIs 20-40 minutes after fentanyl dosing versus the 20 minute period before administration. Gray shading indicates regions are ipsilateral to the injection site while the non-shaded regions indicate they are contralateral (n=5, p-values based on a two-tailed t-test).

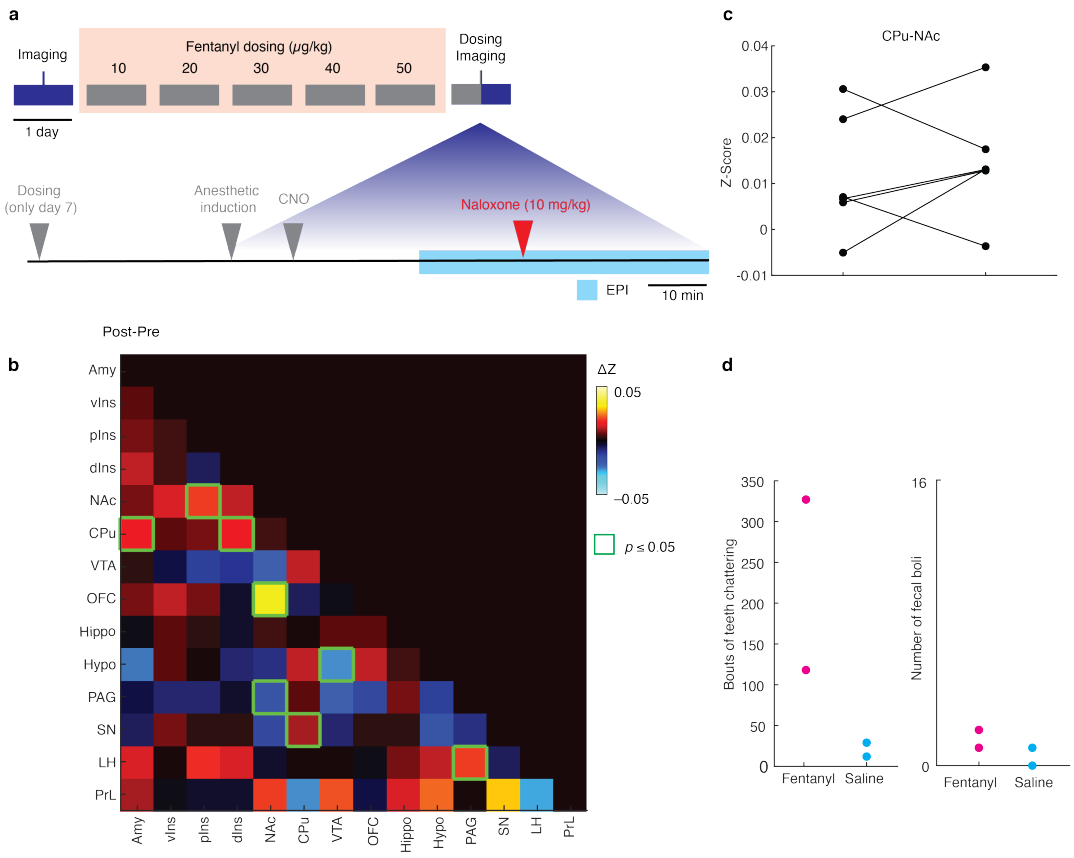

Figure 4.4: **Inhibiting the insular cortex produces a divergent profile of withdrawal.**

a) Diagram of imaging paradigm. Rats were dosed with fentanyl 90 minutes before the EPI. CNO was given 30 minutes before the EPI scan to allow for adequate induction of the inhibitory hM4Di DREADDS. A 10 mg/mg dose of naloxone was given I.P. 20 minutes into the scan. (b) A difference matrix of the average Z score among ROIs 20-40 minutes after naloxone dosing versus the 20 minute period before administration (n=6, p-values based on a two-tailed one sample t-test). (c) Dot plots showing lack of significant change between CPu and NAc connectivity ($p>0.05$). (d) Quantification of somatic symptoms of naloxone-precipitated withdrawal in chronically dosed rats. Bouts of teeth chattering in rats chronically dosed with fentanyl versus saline show increased chattering in the fentanyl rats albeit. The number of fecal boli in fentanyl-dosed rats is approximately the same as in the saline condition.

4.5 Materials and Methods

Animals

All animal procedures were performed in strict compliance with US Federal guidelines, with oversight by the MIT Committee on Animal Care. Male Sprague-Dawley rats (150-300g) were purchased from Charles River Laboratories (Wilmington, MA) and used for the *in vivo* data presented in this paper. All animals were housed and maintained on a 12h light/dark cycle with ad libitum access to food and water.

Chemicals

Fentanyl solution (1 mg/mL) was obtained from Millipore Sigma and diluted in sterile saline solution at 0.05 mg/mL for all experiments. Naloxone hydrochloride was purchased form Thermo Fisher Scientific and reconstituted in saline at 10 mg/mL. Clozapine N-oxide hydrochloride (CNO) was sourced from Cayman Chemical and administered in saline at a 5 mg/mL concentration.

Stereotaxic injection of viral vectors

Animals were prepared for cranial surgery to expose the desired viral injection site at the anterior insular cortex. A total of 10 rats received injections. Each animal was anesthetized with isoflurane (4% for induction, 1.5-2% for maintenance). A small hole was drilled into the skull above the target sites, 3.0 mm anterior and +/-4.2 mm lateral to bregma. A Hamilton Neuros syringe (5 µL, Model 75 RN, 33 gauge) was preloaded with virus (pAAV-hSyn-hM4D(Gi)-mCherry, Addgene Plasmid 50475) were then lowered into the brain and infused at a rate of 0.1 μL/min at two sites (0.75 μL per site), 6.1 mm and 5.8 mm below the skull surface. The syringe was slowly removed 5 minutes after the viral injection. Skin incisions were closed by sterile sutures. Slow-release buprenorphine (0.1 mg/kg, MIT Pharmacy) was administered subcutaneously to minimize pain and discomfort.

Paramus infusions

Five rats were used for paramus experiments. Each animal was anesthetized with isoflurane (4% for induction, 1.5-2% for maintenance). Cranial surgery was performed to expose the skull. A small hole was drilled into the skull above the target sites, 3.0 mm anterior and either +4.2 mm (n=3) or -4.2mm (n=2) lateral to bregma. A Hamilton Neuros syringe (5 µL, Model 75 RN, 33 gauge) was preloaded with paramus contrast agent (synthesized using previously outlined protocol [65]) and then lowered into the brain and infused at a rate of 0.1 μL/min at two sites (0.75 μL per site), 6.1 mm and 5.8 mm below the skull surface. The syringe was slowly removed 5 minutes after the infusion. Skin incisions were closes with Vetbond tissue adhesive (MIT Pharmacy), and rats were transferred to the MRI for scanning.

Chronic fentanyl dosing

A cohort of six rats were given chronic fentanyl. Once every 24 hours for five days, rats were given increasing doses of fentanyl: 0.01, 0.02, 0.03, 0.04, and 0.05 mg/kg. Imaging and/or behavioral testing was performed on day 6.

Magnetic resonance imaging

All animals were imaged using a 7T Biospec MRI scanner (Bruker, Ettlingen, Germany) scanner operating with custom-made surface coils. High resolution anatomical images were obtained with a TurboRARE (rapid acquisition with relaxation enhancement) sequence with a TE of 33ms, TR of 2.5 s, a RARE factor of 8, and 12 averages. The geometry of the scan incorporated 256x256 matrices over a 2.25 x 2.25 cm FOV for a 15-slice volume with 1 mm slice thickness. This was followed by 1800 repetitions of a T_2*-weighted echo planar imaging (EPI) sequence. Parameters were a TE of 16 ms, FA = 80.9, TR = 2s, FOV = 2.25× 2.25 cm, 64x64 matrices for an in-plane resolution of approximately 350 × 350 μm, and 15 slices with slice thickness = 1 mm.

For each scan session, rats were induced with 3% isoflurane in a 2:1 oxygen to air mix and administered a bolus of 0.1 mg/kg dexmedetomidine (MIT Pharmacy). This was followed by a maintenance dose at 0.1 mg/kg/hr. Isoflurane was decreased from

1.5% to 0.75% over 15 minutes and maintained at this level for the rest of the scan. Animals were warmed using a water-heating pad. Heart rate and blood oxygenation saturation level were continuously monitored using an MRI-compatible infrared pulse oximeter (Nonin Medical, Plymouth, MN). The EPI scan sequence began 45 minutes after the initial dexmedetomidine bolus.

For acute fentanyl experiments, a dose of 0.01 mg/kg of fentanyl was given over 10 seconds at 20 mintues into the EPI. For the naloxone-precipitated withdrawal scans, 0.05 mg/kg of fentanyl was given 90 minutes before the EPI and 10 mg/kg of naloxone was given at 20 minutes into the EPI. For DREADD experiments, 5 mg/kg of CNO was given 60 minutes before the EPI.

MRI data analysis

Images were reconstruction in ParaVision 7 software and then imported into into the National Institute of Health AFNI software package. Alignment was performed by registering high-resolution anatomical images of each rat to a Waxholm coordinate space rat brain atlas. Pre-processing steps included: motion correction using rigid-body volume correction and Fourier interpolation, spatial smoothing with a Gaussian spatial kernel of 1 mm FWHM, scaling voxel data to the mean of its time series, and least square detrending of the data with removal of first order Legendre polynomials.

All further analysis was performed in MATLAB (Wolfram) using custom scripts. The signal-to-noise ratio of data was computed and voxels with a tSNR <10 were omitted from the rest of the analysis. Motion parameters previously obtained during the rigid-body motion correction and the mean global signal were linearly regressed from the data. ROIs obtained from the Waxholm atlas were used to computed seed-based maps. The average time course of an ROI was correlated to all other voxels in the brain. Z-scores was obtained by taking the inverse hyperbolic tangent of the Pearson correlation coefficient.

Maps illustrating Z-score values displayed voxels in which the p-value of the Pearson correlation coefficent was above 0.05. Correlation matrices were computed by taking the average correlation between two ROIs. Difference matrices were computed from

the Z-scores obtained for the first 20 minutes and last 20 minutes of a 1-hour EPI scan session. A two-tailed, paired sample t-test was used to quantify p-values.

Behavioral experiments

To record withdrawal behavior in wild-type rats, we applied the chronic fentanyl dosing protocol (n=6) or a saline control (n=5). On day 6, 10 mg/kg of naloxone was given 90 minutes a dose of 0.05 mg/kg fentanyl or saline. Rats were placed in a Plexiglas box housed inside a MedAssociates behavioral chamber. Three IR cameras were placed around the box and rat behavior was recorded at 20 frames/second. Recording lasted for 40 minutes post-naloxone injection. For rats with DREADDs, CNO was given 30 minutes before the naloxone injection (n=2 had chronic fentanyl, n=2 had been given the saline control).

The resultant behavior was quantified manually for the entire 40 minute recording. This included the bouts of teeth chatters and the number of fecal boli expelled.

4.6 Supplemental Figures

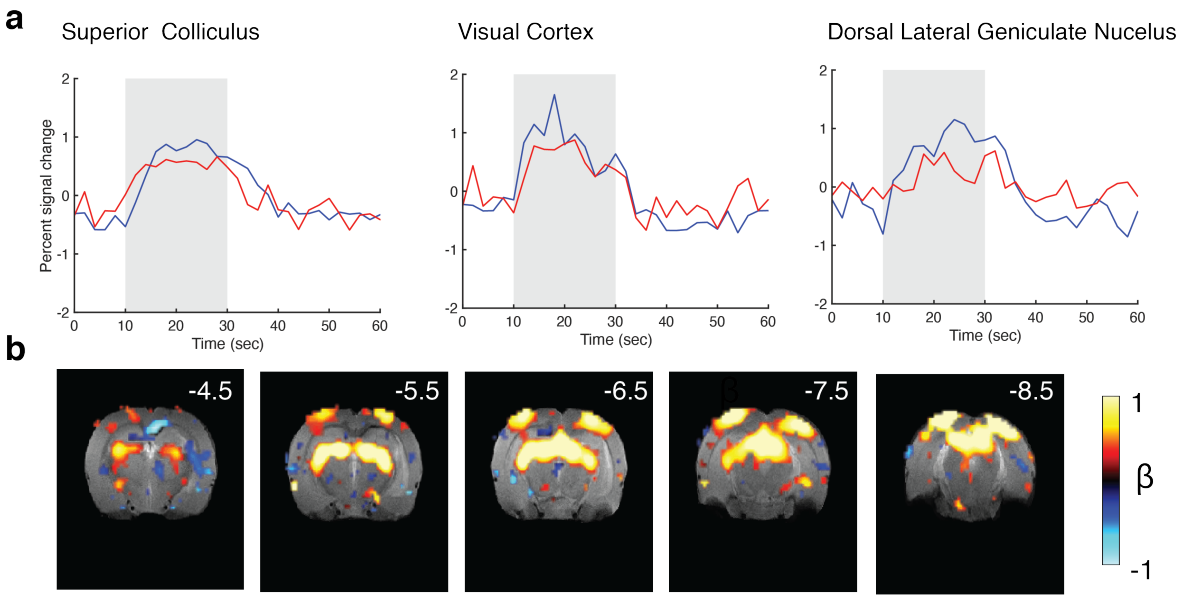

Figure S1: Visual response under light anesthetic regime.
(a) The percent signal change in regions related to visual pathway, trace is averaged over 6 trials and gray shaded regions represent the time period when a flashing light stimulus was on (10 Hz for 20 seconds). (b) Beta coefficient of the BOLD visual response

Chapter 5

Conclusion

The work in the thesis demonstrates methods for investigating brain-body interactions. This includes characterization of routes to bybass the blood-brain barrier and the application of a cholinergic imaging agent to study a system key in brain-body physiology. Imaging methods were applied to a pathology that is often solely attributed to brain dysfunciton in the revised context of whole body physiology. Despite these developments, there is work must be done to achieve holistic understanding of brain-body interactions in neurobiology.

5.1 Future directions in assessing and bypassing the blood brain barrier

Our quantitative assessment of disrupting and bypassing the BBB not only allowed us to assess the benefits of various delivery approaches, but it allowed us to assess innate properties of the BBB itself. In practical terms, our study shows that the most homogeneous profiles of delivery can be achieved through disruption of tight junctions, either mechanically or chemically. Given the dilution of exogenous molecules in the vasculature, exogenous agents limited in concentration benefit from intra-CSF delivery where they are less diluted before reaching the parenchyma. Techincally speaking, chemical disruption is the easiest to implement as it only requires estab-

lishing a peripheral catheter. Ultrasound uses specialized electronics, and in larger mammals, skull shaving may be required. Intra-CSF is the most invasive procedure as it requires access the ventricular space. However, a practiced surgeon is capable of becoming reliable in this procedure.

It is worth noting that there are some important caveats to our study. First, all our work was done with a neutral and relatively small contrast agent, gadoteridol. Assessing the transport of larger molecules possessing differing amounts of hydrophobicity and charge will allow us to see how likely these delivery methods are to translate to diverse classes of drugs and imaging agents. Second, we only assessed a single instance of administration. In clinic, multiple doses are often administered. Assessing the integrity of BBB recovery following repeated disruptions will provide insight into the safety of these techniques for long-term therapeutic use. It will also tell us something about the intrinsic rigidity of tight junction protein architecture and BBB homeostasis.

A remaining question is the exact the mechanism of LPA-mediated BBB delivery. There is evidence suggesting it induces permeability via the Rho/Rho kinase (ROCK) pathway [147, 148]. However, the precise mechanism of LPA inducing transient BBB permeability is not fully understood. A viable approach to probe this question is to assess molecular changes in 3-D models of vascualture networks co-cultured with neurons and glial cells. Using previously engineered microfluidic models of the blood–brain barrier, we can assess changes in permeability under different conditions of LPA exposure [149].

5.2 Further assessment of the cholinergic system

Our studies demonstrate the creation of a metalloporphyrin contrast agent capable of detecting cholinesterase-specific activity (ChE). Through kinetic modeling, we were able to assess differential distribution of these enzymes in anatomically-defined brain regions. While we examined these properties in a wild-type rat, it is known that cholinergic function is dysregulated in diseases such as Alzheimer's as well as austim

spectrum disorder (ASD). Thus models of Alzheimers's such as *APOE4* knock-in rodents and models of syndromic austim such as *Fmr1* knock-out mice and rats would serve as ideal systems to test this sensor [150, 151].

Furthermore, given the high concentration of peripheral acetycholine, it is worth investigating applicatin of this agent through peripheral delivery methods. This can be tested via intravascular injection (IV) or the intraperitoneal route (IP). Much like in the brain, we can apply pharmacokinetic modeling to assess relative concentrations of the enzyme in peripheral tissues. Additionally, given the multimodal nature of the compound, we are able to take advantage of its alternative properties. For instance, we can explore the appliction of live photoacoustic tomography imaging [152]. We can also take advantage of the fluorescence nature of the compound to validate distribution of cholinesterases in the peripheral nervous system with post-mortem tissue histology.

5.3 Towards a deeper undertanding of brain-body physiology in opioid use disorder

The results of our studies of the insular cortex in opioid dependence demonstrate our approach to investigating the role of brain-body interactions in drug abuse. Of note is that we used a paradigm in which precise quantities of fentanyl were administered to our rats by an experimenter. The benefit of this approach is that it controls for variables such as the amount of fentanyl given to the subjects and the timing of dosing. However, the caveat is that we are only capturing the effect of repeated opioid exposure. To capture drug seeking behavior, a self-administration paradigm should be implemented. This will allow us to correlate drug seeking behavior (i.e. lever presses a rodent makes to obtain a fentanyl infusion) with functional activity measures obtained from our MRI experiments.

Other tools for targeting cell types in the insular cortex can also be explored. An inspiring approach to capture how the insular cortex modulates peripheral function is combining Fos-TRAP with chemogenetics [153]. Specifically, neurons expressing the

immediate early gene c-Fos during withdrawal can be labeled using targeted recombination in active populations (TRAP) [154]. To test if these neurons are sufficient to drive the somatic symptoms of withdrawal, we can implement chemogenetic activation and inhibition of these populations. Combining the molecular specificity of imaging probes and viral vectors with the imaging capabilities of MRI offers an exciting world of possibilities for neurobiological investigation.

References

[1] Hans-Rudolf Berthoud and Winfried L Neuhuber. "Functional and chemical anatomy of the afferent vagal system". In: *Autonomic Neuroscience*. Fever:the role of the vagus nerve 85.1 (Dec. 20, 2000), pp. 1–17. ISSN: 1566-0702.

[2] Rachel L. Wolfson, Amira Abdelaziz, Genelle Rankin, Sarah Kushner, Lijun Qi, Ofer Mazor, Seungwon Choi, Nikhil Sharma, and David D. Ginty. "DRG afferents that mediate physiologic and pathologic mechanosensation from the distal colon". In: *Cell* 186.16 (Aug. 2023), 3368–3385.e18. ISSN: 00928674.

[3] William A. Banks. "Brain Meets Body: The Blood-Brain Barrier as an Endocrine Interface". In: *Endocrinology* 153.9 (Sept. 1, 2012), pp. 4111–4119. ISSN: 0013-7227.

[4] Alan Jasanoff. *The biological mind: How brain, body, and environment collaborate to make us who we are*. Basic Books, 2018.

[5] Iris Berent, Rachel M. Theodore, and Erick Valencia. "Autism attenuates the perception of the mind-body divide". In: *Proceedings of the National Academy of Sciences* 119.49 (Dec. 6, 2022). Publisher: Proceedings of the National Academy of Sciences, e2211628119.

[6] John H. Byrne, Ruth Heidelberger, and M. Neal Waxham. *From Molecules to Networks: An Introduction to Cellular and Molecular Neuroscience*. Google-Books-ID: SrJZAwAAQBAJ. Academic Press, May 23, 2014. 692 pp. ISBN: 978-0-12-398267-4.

[7] Uwe Windhorst and Hakan Johansson. *Modern Techniques in Neuroscience Research*. Google-Books-ID: xfXsCAAAQBAJ. Springer Science & Business Media, Dec. 6, 2012. 1336 pp. ISBN: 978-3-642-58552-4.

[8] Javier DeFelipe and Edward G. Jones. "Santiago Ramón y Cajal and methods in neurohistology". In: *Trends in Neurosciences* 15.7 (July 1, 1992). Publisher: Elsevier, pp. 237–246. ISSN: 0166-2236, 1878-108X.

[9] *The Nobel Prize in Physiology or Medicine 1906*. NobelPrize.org. URL: https://www.nobelprize.org/prizes/medicine/1906/cajal/article/ (visited on 06/09/2024).

[10] Lothar Schermelleh, Alexia Ferrand, Thomas Huser, Christian Eggeling, Markus Sauer, Oliver Biehlmaier, and Gregor P. C. Drummen. "Super-resolution microscopy demystified". In: *Nature Cell Biology* 21.1 (Jan. 2019). Publisher: Nature Publishing Group, pp. 72–84. ISSN: 1476-4679.

[11] Nikolaus Kriegeskorte, Marieke Mur, and Peter A. Bandettini. "Representational similarity analysis - connecting the branches of systems neuroscience". In: *Frontiers in Systems Neuroscience* 2 (Nov. 24, 2008). Publisher: Frontiers. ISSN: 1662-5137.

[12] Yang Shen, Alessandro Luchetti, Giselle Fernandes, Won Do Heo, and Alcino J. Silva. "The emergence of molecular systems neuroscience". In: *Molecular Brain* 15.1 (Jan. 4, 2022), p. 7. ISSN: 1756-6606.

[13] Blue B. Lake et al. "Neuronal subtypes and diversity revealed by single-nucleus RNA sequencing of the human brain". In: *Science (New York, N.Y.)* 352.6293 (June 24, 2016), pp. 1586–1590. ISSN: 1095-9203.

[14] Katarína Tiklová et al. "Single-cell RNA sequencing reveals midbrain dopamine neuron diversity emerging during mouse brain development". In: *Nature Communications* 10.1 (Feb. 4, 2019), p. 581. ISSN: 2041-1723.

[15] Yong Ku Cho et al. "Roadmap on neurophotonics". In: *Journal of Optics (2010)* 18.9 (Sept. 2016), p. 093007. ISSN: 2040-8978.

[16] Margaret M. Koletar, Adrienne Dorr, Mary E. Brown, JoAnne McLaurin, and Bojana Stefanovic. "Refinement of a chronic cranial window implant in the rat for longitudinal in vivo two–photon fluorescence microscopy of neurovascular function". In: *Scientific Reports* 9.1 (Apr. 2, 2019). Publisher: Nature Publishing Group, p. 5499. ISSN: 2045-2322.

[17] Georgia R. Frost, Valerie Longo, Thomas Li, Lauren A. Jonas, Martin Judenhofer, Simon Cherry, Jason Koutcher, Carl Lekaye, Pat Zanzonico, and Yue-Ming Li. "Hybrid PET/MRI enables high-spatial resolution, quantitative imaging of amyloid plaques in an Alzheimer's disease mouse model". In: *Scientific Reports* 10.1 (June 25, 2020). Publisher: Nature Publishing Group, p. 10379. ISSN: 2045-2322.

[18] N. Kovacević, J. T. Henderson, E. Chan, N. Lifshitz, J. Bishop, A. C. Evans, R. M. Henkelman, and X. J. Chen. "A three-dimensional MRI atlas of the mouse brain with estimates of the average and variability". In: *Cerebral Cortex (New York, N.Y.: 1991)* 15.5 (May 2005), pp. 639–645. ISSN: 1047-3211.

[19] Souparno Ghosh, Peter Harvey, Jacob C. Simon, and Alan Jasanoff. "Probing the brain with molecular fMRI". In: *Current Opinion in Neurobiology* 50 (June 2018), pp. 201–210. ISSN: 1873-6882.

[20] Timothy W Secomb. "Hemodynamics". In: *Comprehensive physiology* 6.2 (2016), p. 975.

[21] Nikos K. Logothetis. "What we can do and what we cannot do with fMRI". In: *Nature* 453.7197 (June 12, 2008), pp. 869–878. ISSN: 1476-4687.

[22] Suraj D Serai. "Basics of magnetic resonance imaging and quantitative parameters T1, T2, T2*, T1rho and diffusion-weighted imaging". In: *Pediatric radiology* 52.2 (2022), pp. 217–227.

[23] Elizabeth M.C. Hillman. "Coupling Mechanism and Significance of the BOLD Signal: A Status Report". In: *Annual Review of Neuroscience* 37.1 (July 8, 2014), pp. 161–181. ISSN: 0147-006X, 1545-4126.

[24] Mikhail G. Shapiro, Gil G. Westmeyer, Philip A. Romero, Jerzy O. Szablowski, Benedict Küster, Ameer Shah, Christopher R. Otey, Robert Langer, Frances H. Arnold, and Alan Jasanoff. "Directed evolution of a magnetic resonance imaging contrast agent for noninvasive imaging of dopamine". In: *Nature Biotechnology* 28.3 (Mar. 2010), pp. 264–270. ISSN: 1546-1696.

[25] Aviad Hai, Lili X Cai, Taekwan Lee, Victor S Lelyveld, and Alan Jasanoff. "Molecular fMRI of serotonin transport". In: *Neuron* 92.4 (2016), pp. 754–765.

[26] Satoshi Okada, Benjamin B. Bartelle, Nan Li, Vincent Breton-Provencher, Jiyoung J. Lee, Elisenda Rodriguez, James Melican, Mriganka Sur, and Alan Jasanoff. "Calcium-dependent molecular fMRI using a magnetic nanosensor". In: *Nature Nanotechnology* 13.6 (June 2018). Publisher: Nature Publishing Group, pp. 473–477. ISSN: 1748-3395.

[27] He Wei, Agata Wiśniowska, Jingxuan Fan, Peter Harvey, Yuanyuan Li, Victoria Wu, Eric C Hansen, Juanye Zhang, Michael G Kaul, Abigail M Frey, et al. "Single-nanometer iron oxide nanoparticles as tissue-permeable MRI contrast agents". In: *Proceedings of the National Academy of Sciences* 118.42 (2021), e2102340118.

[28] Gil G Westmeyer, Yves Durocher, and Alan Jasanoff. "A secreted enzyme reporter system for MRI". In: *Angewandte Chemie (International ed. in English)* 49.23 (2010), p. 3909.

[29] Gil G. Westmeyer, Yelena Emer, Jutta Lintelmann, and Alan Jasanoff. "MRI-based detection of alkaline phosphatase gene reporter activity using a

porphyrin solubility switch". In: *Chemistry and Biology* 21.3 (2014), pp. 422–429.

[30] Brian Wai Chow and Chenghua Gu. "The Molecular Constituents of the Blood–Brain Barrier". In: *Trends in Neurosciences* 38.10 (Oct. 1, 2015). Publisher: Elsevier, pp. 598–608. ISSN: 0166-2236, 1878-108X.

[31] Domenico Ribatti, Beatrice Nico, Enrico Crivellato, and Marco Artico. "Development of the blood-brain barrier: A historical point of view". In: *The Anatomical Record Part B: The New Anatomist* 289B.1 (2006). _eprint: https://onlinelibrary.wiley.com/doi/pdf/10.1002/ar.b.20087, pp. 3–8. ISSN: 1552-4914.

[32] T. S. Reese and M. J. Karnovsky. "Fine structural localization of a blood-brain barrier to exogenous peroxidase". In: *The Journal of Cell Biology* 34.1 (July 1967), pp. 207–217. ISSN: 0021-9525.

[33] John L Mikitsh and Ann-Marie Chacko. "Pathways for small molecule delivery to the central nervous system across the blood-brain barrier". In: *Perspectives in medicinal chemistry* 6 (2014), PMC–S13384.

[34] William M. Pardridge. "Treatment of Alzheimer's Disease and Blood–Brain Barrier Drug Delivery". In: *Pharmaceuticals* 13.11 (Nov. 2020). Number: 11 Publisher: Multidisciplinary Digital Publishing Institute, p. 394. ISSN: 1424-8247.

[35] Andrew Wong, Mao Ye, Amanda Levy, Jeffrey Rothstein, Dwight Bergles, and Peter Charles Searson. "The blood-brain barrier: an engineering perspective". In: *Frontiers in Neuroengineering* 6 (Aug. 30, 2013). Publisher: Frontiers. ISSN: 1662-6443.

[36] Agessandro Abrahao et al. "First-in-human trial of blood–brain barrier opening in amyotrophic lateral sclerosis using MR-guided focused ultrasound". In: *Nature Communications* 10.1 (Sept. 26, 2019). Publisher: Nature Publishing Group, p. 4373. ISSN: 2041-1723.

[37] Kushan Gandhi, Anita Barzegar-Fallah, Ashik Banstola, Shakila B. Rizwan, and John N. J. Reynolds. "Ultrasound-Mediated Blood–Brain Barrier Disruption for Drug Delivery: A Systematic Review of Protocols, Efficacy, and Safety Outcomes from Preclinical and Clinical Studies". In: *Pharmaceutics* 14.4 (Apr. 11, 2022), p. 833. ISSN: 1999-4923.

[38] *Launched: First Clinical Trial of Focused Ultrasound for Alzheimer's - SRI Magazine 2017 - Sunnybrook Research Institute*. URL: https://sunnybrook.ca/research/content/?page=sri-magazine-2017-maclinical-trial-fus-alzheimers (visited on 06/10/2024).

[39] Lazzaro Di Biase, Emma Falato, and Vincenzo Di Lazzaro. "Transcranial focused ultrasound (tFUS) and transcranial unfocused ultrasound (tUS) neuromodulation: from theoretical principles to stimulation practices". In: *Frontiers in neurology* 10 (2019), p. 455075.

[40] Marc-André Bellavance, Marie Blanchette, and David Fortin. "Recent advances in blood–brain barrier disruption as a CNS delivery strategy". In: *The AAPS journal* 10 (2008), pp. 166–177.

[41] Raleigh M Linville, Jackson G DeStefano, Matt B Sklar, Chengyan Chu, Piotr Walczak, and Peter C Searson. "Modeling hyperosmotic blood–brain barrier opening within human tissue-engineered in vitro brain microvessels". In: *Journal of Cerebral Blood Flow & Metabolism* 40.7 (July 2020), pp. 1517–1532. ISSN: 0271-678X.

[42] *Intrathecal Drug Delivery in the Era of Nanomedicine - PMC*. URL: https://www.ncbi.nlm.nih.gov/pmc/articles/PMC8182643/ (visited on 06/10/2024).

[43] Grace Lee, Marcie Glicksman, Rajan Patel, Nisheka Vanjani, and Priya Kumthekar. "Retrospetive reciew of intra-CSF drug delivery." In: *Neuro-Oncology* 25 (Supplement_5 Nov. 1, 2023), p. v103. ISSN: 1522-8517.

[44] EM Delhaas and FJPM Huygen. "Complications associated with intrathecal drug delivery systems". In: *BJA education* 20.2 (2020), pp. 51–57.

[45] I. Akdogan, Y. Kiroglu, S. Onur, and N. Karabuluti. "The volume fraction of brain ventricles to total brain volume: a computed tomography stereological study". In: *Folia Morphologica* 69.4 (Nov. 2010), pp. 193–200. ISSN: 0015-5659.

[46] Peter Reinstrup, Erik Ryding, Tomas Ohlsson, Peter Lee Dahm, and Tore Uski. "Cerebral Blood Volume (CBV) in Humans during Normo- and Hypocapnia: Influence of Nitrous Oxide (N2O)". In: *Anesthesiology* 95.5 (Nov. 1, 2001), pp. 1079–1082. ISSN: 0003-3022.

[47] Luke Kaplan, Brian W. Chow, and Chenghua Gu. "Neuronal regulation of the blood–brain barrier and neurovascular coupling". In: *Nature reviews. Neuroscience* 21.8 (Aug. 2020), pp. 416–432. ISSN: 1471-003X.

[48] Nicole Brandt and Rachel Flurie. "Acetylcholine". In: *Encyclopedia of Behavioral Medicine* (2020), pp. 18–19.

[49] Miroslav Pohanka. "Cholinesterases, a target of pharmacology and toxicology". In: *Biomedical Papers of the Medical Faculty of the University Palacky, Olomouc, Czechoslovakia* 155.3 (Sept. 2011), pp. 219–229. ISSN: 1804-7521.

[50] Mauricio Rosas-Ballina, Peder S Olofsson, Mahendar Ochani, Sergio I Valdés-Ferrer, Yaakov A Levine, Colin Reardon, Michael W Tusche, Valentin A Pavlov, Ulf Andersson, Sangeeta Chavan, et al. "Acetylcholine-synthesizing T cells relay neural signals in a vagus nerve circuit". In: *Science* 334.6052 (2011), pp. 98–101.

[51] Masato Inazu. "Functional Expression of Choline Transporters in the Blood–Brain Barrier". In: *Nutrients* 11.10 (2019), p. 2265.

[52] Hermona Soreq. "Checks and balances on cholinergic signaling in brain and body function". In: *Trends in neurosciences* 38.7 (2015), pp. 448–458.

[53] Andrea Haake, Kevin Nguyen, Lauren Friedman, Binu Chakkamparambil, and George T Grossberg. "An update on the utility and safety of cholinesterase inhibitors for the treatment of Alzheimer's disease". In: *Expert Opinion on Drug Safety* 19.2 (Feb. 2020). Publisher: Taylor & Francis, pp. 147–157. ISSN: 1474-0338.

[54] Hong Xu, Sara Garcia-Ptacek, Linus Jönsson, Anders Wimo, Peter Nordström, and Maria Eriksdotter. "Long-term Effects of Cholinesterase Inhibitors on Cognitive Decline and Mortality". In: *Neurology* 96.17 (Apr. 27, 2021). Publisher: Wolters Kluwer, e2220–e2230.

[55] Seth D Friedman, Dennis WW Shaw, Alan A Artru, Geraldine Dawson, Helen Petropoulos, and Stephen R Dager. "Gray and white matter brain chemistry in young children with autism". In: *Archives of general psychiatry* 63.7 (2006), pp. 786–794.

[56] Stephen I Deutsch, Maria R Urbano, Serina A Neumann, Jessica A Burket, and Elionora Katz. "Cholinergic abnormalities in autism: is there a rationale for selective nicotinic agonist interventions?" In: *Clinical neuropharmacology* 33.3 (2010), pp. 114–120.

[57] Golan Karvat and Tali Kimchi. "Acetylcholine elevation relieves cognitive rigidity and social deficiency in a mouse model of autism". In: *Neuropsychopharmacology* 39.4 (2014), pp. 831–840.

[58] John Strang, Nora D. Volkow, Louisa Degenhardt, Matthew Hickman, Kimberly Johnson, George F. Koob, Brandon D. L. Marshall, Mark Tyndall, and Sharon L. Walsh. "Opioid use disorder". In: *Nature Reviews Disease Primers* 6.1 (Jan. 9, 2020). Publisher: Nature Publishing Group, pp. 1–28. ISSN: 2056-676X.

[59] Christoph Stein. "Opioid receptors". In: *Annual review of medicine* 67 (2016), pp. 433–451.

[60] Elena H Chartoff and Hilary S Connery. “It’s MORe exciting than mu: crosstalk between mu opioid receptors and glutamatergic transmission in the mesolimbic dopamine system”. In: *Frontiers in pharmacology* 5 (2014), p. 87943.

[61] George F Koob, Pietro Paolo Sanna, and Floyd E Bloom. “Neuroscience of Addiction”. In: *Neuron* 21.3 (Sept. 1998), pp. 467–476. ISSN: 08966273.

[62] Thomas R. Kosten and Tony P. George. “The Neurobiology of Opioid Dependence: Implications for Treatment”. In: *Science & Practice Perspectives* 1.1 (July 2002), pp. 13–20. ISSN: 1930-4307.

[63] Alicja Lerner and Michael Klein. “Dependence, withdrawal and rebound of CNS drugs: an update and regulatory considerations for new drugs development”. In: *Brain communications* 1.1 (2019), fcz025.

[64] Xingchao Wang, Qiong Wu, Laura Egan, Xiaosi Gu, Pinan Liu, Hong Gu, Yihong Yang, Jing Luo, Yanhong Wu, Zhixian Gao, et al. “Anterior insular cortex plays a critical role in interoceptive attention”. In: *elife* 8 (2019), e42265.

[65] Sarah Bricault, Ali Barandov, Peter Harvey, Elizabeth DeTienne, Aviad Hai, and Alan Jasanoff. “Image-guided neural activity manipulation with a paramagnetic drug”. In: *Nature Communications* 11.1 (Jan. 9, 2020). Publisher: Nature Publishing Group, p. 136. ISSN: 2041-1723.

[66] Bryan L. Roth. “DREADDs for Neuroscientists”. In: *Neuron* 89.4 (Feb. 17, 2016), pp. 683–694. ISSN: 0896-6273.

[67] Blaine N. Armbruster, Xiang Li, Mark H. Pausch, Stefan Herlitze, and Bryan L. Roth. “Evolving the lock to fit the key to create a family of G protein-coupled receptors potently activated by an inert ligand”. In: *Proceedings of the National Academy of Sciences* 104.12 (Mar. 20, 2007). Publisher: Proceedings of the National Academy of Sciences, pp. 5163–5168.

[68] Amiram Grinvald and Rina Hildesheim. “VSDI: a new era in functional imaging of cortical dynamics”. In: *Nature Reviews Neuroscience* 5.11 (Nov. 2004). Publisher: Nature Publishing Group, pp. 874–885. ISSN: 1471-0048.

[69] N. Joan Abbott, Adjanie A. K. Patabendige, Diana E. M. Dolman, Siti R. Yusof, and David J. Begley. “Structure and function of the blood–brain barrier”. In: *Neurobiology of Disease*. Special Issue: Blood Brain Barrier 37.1 (Jan. 1, 2010), pp. 13–25. ISSN: 0969-9961.

[70] Edward A. Neuwelt et al. “Engaging neuroscience to advance translational research in brain barrier biology”. In: *Nature Reviews. Neuroscience* 12.3 (Mar. 2011), pp. 169–182. ISSN: 1471-0048.

[71] Georg C. Terstappen, Axel H. Meyer, Robert D. Bell, and Wandong Zhang. “Strategies for delivering therapeutics across the blood-brain barrier”. In: *Nature Reviews. Drug Discovery* 20.5 (May 2021), pp. 362–383. ISSN: 1474-1784.

[72] Loukas I. Goulatis and Eric V. Shusta. “Protein engineering approaches for regulating blood-brain barrier transcytosis”. In: *Current Opinion in Structural Biology* 45 (Aug. 2017), pp. 109–115. ISSN: 1879-033X.

[73] Victor M. Pulgar. “Transcytosis to Cross the Blood Brain Barrier, New Advancements and Challenges”. In: *Frontiers in Neuroscience* 12 (2018), p. 1019. ISSN: 1662-4548.

[74] Jeffrey J. Iliff et al. “A Paravascular Pathway Facilitates CSF Flow Through the Brain Parenchyma and the Clearance of Interstitial Solutes, Including Amyloid ”. In: *Science translational medicine* 4.147 (Aug. 15, 2012), 147ra111. ISSN: 1946-6234.

[75] Jeffrey J. Iliff, Hedok Lee, Mei Yu, Tian Feng, Jean Logan, Maiken Nedergaard, and Helene Benveniste. “Brain-wide pathway for waste clearance captured by contrast-enhanced MRI”. In: *The Journal of Clinical Investigation* 123.3 (Mar. 2013), pp. 1299–1309. ISSN: 1558-8238.

[76] Jerzy O. Szablowski, Avinoam Bar-Zion, and Mikhail G. Shapiro. "Achieving Spatial and Molecular Specificity with Ultrasound-Targeted Biomolecular Nanotherapeutics". In: *Accounts of Chemical Research* 52.9 (Sept. 17, 2019), pp. 2427–2434. ISSN: 1520-4898.

[77] Gabriel P. Howles, Kristin F. Bing, Yi Qi, Stephen J. Rosenzweig, Kathryn R. Nightingale, and G. Allan Johnson. "Contrast-enhanced in vivo magnetic resonance microscopy of the mouse brain enabled by non-invasive opening of the blood-brain barrier with ultrasound". In: *Magnetic resonance in medicine : official journal of the Society of Magnetic Resonance in Medicine / Society of Magnetic Resonance in Medicine* 64.4 (Oct. 2010), pp. 995–1004. ISSN: 0740-3194.

[78] Nathan McDannold, Yongzhi Zhang, and Natalia Vykhodtseva. "Blood-brain barrier disruption and vascular damage induced by ultrasound bursts combined with microbubbles can be influenced by choice of anesthesia protocol". In: *Ultrasound in Medicine & Biology* 37.8 (Aug. 2011), pp. 1259–1270. ISSN: 1879-291X.

[79] Kevin Beccaria et al. "Opening of the blood-brain barrier with an unfocused ultrasound device in rabbits". In: *Journal of Neurosurgery* 119.4 (Oct. 2013), pp. 887–898. ISSN: 1933-0693.

[80] Ngoc H. On, Sanjot Savant, Myron Toews, and Donald W. Miller. "Rapid and reversible enhancement of blood-brain barrier permeability using lysophosphatidic acid". In: *Journal of Cerebral Blood Flow and Metabolism: Official Journal of the International Society of Cerebral Blood Flow and Metabolism* 33.12 (Dec. 2013), pp. 1944–1954. ISSN: 1559-7016.

[81] Zhizhi Sun, Matthew Worden, James A. Thliveris, Sabine Hombach-Klonisch, Thomas Klonisch, Johan van Lierop, Torsten Hegmann, and Donald W. Miller. "Biodistribution of negatively charged iron oxide nanoparticles (IONPs) in mice and enhanced brain delivery using

lysophosphatidic acid (LPA)". In: *Nanomedicine: Nanotechnology, Biology, and Medicine* 12.7 (Oct. 2016), pp. 1775–1784. ISSN: 1549-9642.

[82] Nancy D. Doolittle, Leslie L. Muldoon, Aliana Y. Culp, and Edward A. Neuwelt. "Delivery of Chemotherapeutics Across the Blood–Brain Barrier: Challenges and Advances". In: *Advances in pharmacology (San Diego, Calif.)* 71 (2014), pp. 203–243. ISSN: 1054-3589.

[83] Jennifer L. Stewart, Sahib S. Khalsa, Rayus Kuplicki, Maria Puhl, T1000 Investigators, and Martin P. Paulus. "Interoceptive attention in opioid and stimulant use disorder". In: *Addiction Biology* 25.6 (2020). _eprint: https://onlinelibrary.wiley.com/doi/pdf/10.1111/adb.12831, e12831. ISSN: 1369-1600.

[84] Rick J. Probst, Jenny M. Lim, Danielle N. Bird, Ginger L. Pole, Aileen K. Sato, and John R. Claybaugh. "Gender differences in the blood volume of conscious Sprague-Dawley rats". In: *Journal of the American Association for Laboratory Animal Science: JAALAS* 45.2 (Mar. 2006), pp. 49–52. ISSN: 1559-6109.

[85] Joost Westerhout, Bart Ploeger, Jean Smeets, Meindert Danhof, and Elizabeth C. M. de Lange. "Physiologically Based Pharmacokinetic Modeling to Investigate Regional Brain Distribution Kinetics in Rats". In: *The AAPS Journal* 14.3 (May 17, 2012), pp. 543–553. ISSN: 1550-7416.

[86] Luce Vander Elst, Jean-Sebastien Raynaud, Veronique Vives, Robin Santus, Gaelle Louin, Philippe Robert, Marc Port, Claire Corot, and Robert N Muller. "Comparative Relaxivities and Efficacies of Gadolinium-based Commercial Contrast Agents." In.

[87] Julian Haigh. *Investigation in to the Effect of Spin Locking on Contrast Agent Relaxivity*. Jan. 1, 2000.

[88] Nickolai Sheikov, Nathan McDannold, Shipra Sharma, and Kullervo Hynynen. “Effect of focused ultrasound applied with an ultrasound contrast agent on the tight junctional integrity of the brain microvascular endothelium”. In: *Ultrasound in medicine & biology* 34.7 (July 2008), pp. 1093–1104. ISSN: 0301-5629.

[89] C. Schulze, C. Smales, L. L. Rubin, and J. M. Staddon. “Lysophosphatidic acid increases tight junction permeability in cultured brain endothelial cells”. In: *Journal of Neurochemistry* 68.3 (Mar. 1997), pp. 991–1000. ISSN: 0022-3042.

[90] Evan Hunter Stanton, Niklas Daniel Åke Persson, Ryszard Stefan Gomolka, Tuomas Lilius, Björn Sigurðsson, Hedok Lee, Anna Lenice Ribeiro Xavier, Helene Benveniste, Maiken Nedergaard, and Yuki Mori. “Mapping of CSF transport using high spatiotemporal resolution dynamic contrast-enhanced MRI in mice: Effect of anesthesia”. In: *Magnetic Resonance in Medicine* 85.6 (2021). _eprint: https://onlinelibrary.wiley.com/doi/pdf/10.1002/mrm.28645, pp. 3326–3342. ISSN: 1522-2594.

[91] Meaghan A. O’Reilly and Kullervo Hynynen. “Ultrasound Enhanced Drug Delivery to the Brain and Central Nervous System”. In: *International journal of hyperthermia : the official journal of European Society for Hyperthermic Oncology, North American Hyperthermia Group* 28.4 (2012), pp. 386–396. ISSN: 0265-6736.

[92] James J. Choi, Shougang Wang, Yao-Sheng Tung, Barclay Morrison, and Elisa E. Konofagou. “Molecules of various pharmacologically-relevant sizes can cross the ultrasound-induced blood-brain barrier opening in vivo”. In: *Ultrasound in Medicine & Biology* 36.1 (Jan. 2010), pp. 58–67. ISSN: 1879-291X.

[93] Marie Blanchette, Luc Tremblay, Martin Lepage, and David Fortin. “Impact of drug size on brain tumor and brain parenchyma delivery after a blood–brain barrier disruption”. In: *Journal of Cerebral Blood Flow & Metabolism* 34.5 (May 2014), pp. 820–826. ISSN: 0271-678X.

[94] Lijun Yang, Benjamin T. Kress, Harris J. Weber, Meenakshisundaram Thiyagarajan, Baozhi Wang, Rashid Deane, Helene Benveniste, Jeffrey J. Iliff, and Maiken Nedergaard. “Evaluating glymphatic pathway function utilizing clinically relevant intrathecal infusion of CSF tracer”. In: *Journal of Translational Medicine* 11 (May 1, 2013), p. 107. ISSN: 1479-5876.

[95] Christian Sam and Bruno Bordoni. *Physiology, Acetylcholine*. StatPearls Publishing, Treasure Island (FL), 2023.

[96] A Chatonnet and O Lockridge. “Comparison of butyrylcholinesterase and acetylcholinesterase.” In: *Biochemical Journal* 260.3 (June 15, 1989), pp. 625–634. ISSN: 0264-6021.

[97] Gabriella Marucci, Michela Buccioni, Diego Dal Ben, Catia Lambertucci, Rosaria Volpini, and Francesco Amenta. “Efficacy of acetylcholinesterase inhibitors in Alzheimer’s disease”. In: *Neuropharmacology* 190 (June 1, 2021), p. 108352. ISSN: 1873-7064.

[98] Drew R. DeBay, George A. Reid, Ian R. Pottie, Earl Martin, Chris V. Bowen, and Sultan Darvesh. “Targeting butyrylcholinesterase for preclinical single photon emission computed tomography (SPECT) imaging of Alzheimer’s disease”. In: *Alzheimer’s & Dementia (New York, N. Y.)* 3.2 (June 2017), pp. 166–176. ISSN: 2352-8737.

[99] Toshiaki Irie, Kiyoshi Fukushi, Hiroki Namba, Masaomi Iyo, Hiroshi Tamagami, Shin-ichiro Nagatsuka, and Nobuo Ikota. “Brain Acetylcholinesterase Activity: Validation of a PET Tracer in a Rat Model of Alzheimer’s Disease”. In.

[100] Tatsuya Kikuchi, Toshimitsu Okamura, Ming-Rong Zhang, and Toshiaki Irie. "PET probes for imaging brain acetylcholinesterase". In: *Journal of Labelled Compounds and Radiopharmaceuticals* 56.3 (2013). _eprint: https://onlinelibrary.wiley.com/doi/pdf/10.1002/jlcr.3002, pp. 172–179. ISSN: 1099-1344.

[101] George Paxinos, Charles R.R. Watson, and Piers C. Emson. "AChE-stained horizontal sections of the rat brain in stereotaxic coordinates". In: *Journal of Neuroscience Methods* 3.2 (Dec. 1980), pp. 129–149. ISSN: 01650270.

[102] Hisao Tago, Toshihiro Maeda, Patrick L. McGeer, and Hiroshi Kimura. "Butyrylcholinesterase-rich neurons in rat brain demonstrated by a sensitive histochemical method". In: *Journal of Comparative Neurology* 325.2 (1992). _eprint: https://onlinelibrary.wiley.com/doi/pdf/10.1002/cne.903250212, pp. 301–312. ISSN: 1096-9861.

[103] Jonathan L. Sessler, Tarak D. Mody, Gregory W. Hemmi, Vincent Lynch, Stuart W. Young, and Richard A. Miller. "Gadolinium(III) texaphyrin: a novel MRI contrast agent". In: *Journal of the American Chemical Society* 115.22 (1993), pp. 10368–10369.

[104] Grégory D. Thiabaud, Miriam Schwalm, Sajal Sen, Ali Barandov, Jacob Simon, Peter Harvey, Virginia Spanoudaki, Peter Müller, Jonathan L. Sessler, and Alan Jasanoff. "Texaphyrin-Based Calcium Sensor for Multimodal Imaging". In: *ACS Sensors* 8.10 (2023), pp. 3855–3861.

[105] C. C. D. Shute and P. R. Lewis. "Cholinesterase-Containing Systems of the Brain of the Rat". In: *Nature* 199.4899 (Sept. 1963). Publisher: Nature Publishing Group, pp. 1160–1164. ISSN: 1476-4687.

[106] Grégory Thiabaud et al. "Oxaliplatin Pt(IV) prodrugs conjugated to gadolinium-texaphyrin as potential antitumor agents". In: *Proceedings of the National Academy of Sciences* 117.13 (Mar. 31, 2020). Publisher: Proceedings of the National Academy of Sciences, pp. 7021–7029.

[107] Erik Ceunen, Johan W. S. Vlaeyen, and Ilse Van Diest. "On the Origin of Interoception". In: *Frontiers in Psychology* 7 (May 23, 2016). Publisher: Frontiers. ISSN: 1664-1078.

[108] Karen S. Quigley, Scott Kanoski, Warren M. Grill, Lisa Feldman Barrett, and Manos Tsakiris. "Functions of Interoception: From Energy Regulation to Experience of the Self". In: *Trends in Neurosciences* 44.1 (Jan. 1, 2021). Publisher: Elsevier, pp. 29–38. ISSN: 0166-2236, 1878-108X.

[109] Gene-Jack Wang, Julia Yang, Nora D. Volkow, Frank Telang, Yeming Ma, Wei Zhu, Christopher T. Wong, Dardo Tomasi, Panayotis K. Thanos, and Joanna S. Fowler. "Gastric stimulation in obese subjects activates the hippocampus and other regions involved in brain reward circuitry". In: *Proceedings of the National Academy of Sciences* 103.42 (Oct. 17, 2006). Publisher: Proceedings of the National Academy of Sciences, pp. 15641–15645.

[110] Martin P. Paulus and Jennifer L. Stewart. "Interoception and Drug Addiction". In: *Neuropharmacology* 76.0 (Jan. 2014), 10.1016/j.neuropharm.2013.07.002. ISSN: 0028-3908.

[111] Nasir H. Naqvi and Antoine Bechara. "The insula and drug addiction: an interoceptive view of pleasure, urges, and decision-making". In: *Brain Structure and Function* 214.5 (June 1, 2010), pp. 435–450. ISSN: 1863-2661.

[112] Mia Haaranen, Giulia Scuppa, Stefano Tambalo, Vilja Järvi, Sine M. Bertozzi, Andrea Armirotti, Wolfgang H. Sommer, Angelo Bifone, and Petri Hyytiä. "Anterior insula stimulation suppresses appetitive behavior while inducing forebrain activation in alcohol-preferring rats". In: *Translational Psychiatry* 10.1 (May 18, 2020). Publisher: Nature Publishing Group, pp. 1–11. ISSN: 2158-3188.

[113] Mia Haaranen, Annika Schäfer, Vilja Järvi, and Petri Hyytiä. "Chemogenetic Stimulation and Silencing of the Insula, Amygdala, Nucleus Accumbens, and

Their Connections Differentially Modulate Alcohol Drinking in Rats". In: *Frontiers in Behavioral Neuroscience* 14 (Nov. 4, 2020). Publisher: Frontiers. ISSN: 1662-5153.

[114] Anel A. Jaramillo, Patrick A. Randall, Spencer Stewart, Brayden Fortino, Kalynn Van Voorhies, and Joyce Besheer. "Functional role for cortical-striatal circuitry in modulating alcohol self-administration". In: *Neuropharmacology* 130 (Mar. 1, 2018), pp. 42–53. ISSN: 0028-3908.

[115] Seven E. Tomek, Gabriela M. Stegmann, Jonna M. Leyrer-Jackson, Jose Piña, and M. Foster Olive. "Restoration of prosocial behavior in rats after heroin self-administration via chemogenetic activation of the anterior insular cortex". In: *Social Neuroscience* 15.4 (July 3, 2020). Publisher: Routledge _eprint: https://doi.org/10.1080/17470919.2020.1746394, pp. 408–419. ISSN: 1747-0919.

[116] Matthew S. McGregor, Caitlin V. Cosme, and Ryan T. LaLumiere. "Insular cortex subregions have distinct roles in cued heroin seeking after extinction learning and prolonged withdrawal in rats". In: *Neuropsychopharmacology* (Mar. 18, 2024). Publisher: Nature Publishing Group, pp. 1–10. ISSN: 1740-634X.

[117] Deborah S. Hasin et al. "DSM-5 Criteria for Substance Use Disorders: Recommendations and Rationale". In: *The American journal of psychiatry* 170.8 (Aug. 1, 2013), pp. 834–851. ISSN: 0002-953X.

[118] George F. Koob and Nora D. Volkow. "Neurocircuitry of Addiction". In: *Neuropsychopharmacology* 35.1 (Jan. 2010). Publisher: Nature Publishing Group, pp. 217–238. ISSN: 1740-634X.

[119] Carlos Blanco and Nora D. Volkow. "Management of opioid use disorder in the USA: present status and future directions". In: *The Lancet* 393.10182 (Apr. 27, 2019). Publisher: Elsevier, pp. 1760–1772. ISSN: 0140-6736, 1474-547X.

[120] C. K. Himmelsbach. "The morphine abstinence syndrome, its nature and treatment". In: *Annals of Internal Medicine* 15.5 (Nov. 1941). Publisher: American College of Physicians, pp. 829–839. ISSN: 0003-4819.

[121] C. K. Himmelsbach. "Clinical studies of drug addiction: Physical dependence, withdrawal and recovery". In: *Archives of Internal Medicine* 69.5 (May 1, 1942), pp. 766–772. ISSN: 0730-188X.

[122] Joseph Friedman and Chelsea L Shover. "Charting the fourth wave: Geographic, temporal, race/ethnicity and demographic trends in polysubstance fentanyl overdose deaths in the United States, 2010–2021". In: *Addiction* 118.12 (2023), pp. 2477–2485.

[123] Martijn P Van Den Heuvel and Hilleke E Hulshoff Pol. "Exploring the brain network: a review on resting-state fMRI functional connectivity". In: *European neuropsychopharmacology* 20.8 (2010), pp. 519–534.

[124] Baxter P Rogers, Victoria L Morgan, Allen T Newton, and John C Gore. "Assessing functional connectivity in the human brain by fMRI". In: *Magnetic resonance imaging* 25.10 (2007), pp. 1347–1357.

[125] Hua-Shan Liu, Svetlana Chefer, Hanbing Lu, Karine Guillem, William Rea, Pradeep Kurup, Yihong Yang, Laura Peoples, and Elliot A. Stein. "Dorsolateral caudate nucleus differentiates cocaine from natural reward-associated contextual cues". In: *Proceedings of the National Academy of Sciences* 110.10 (Mar. 5, 2013). Publisher: Proceedings of the National Academy of Sciences, pp. 4093–4098.

[126] Hanbing Lu, Qihong Zou, Hong Gu, Marcus E. Raichle, Elliot A. Stein, and Yihong Yang. "Rat brains also have a default mode network". In: *Proceedings of the National Academy of Sciences* 109.10 (Mar. 6, 2012). Publisher: Proceedings of the National Academy of Sciences, pp. 3979–3984.

[127] Arun Niranjan, Isabel N. Christie, Samuel G. Solomon, Jack A. Wells, and Mark F. Lythgoe. “fMRI mapping of the visual system in the mouse brain with interleaved snapshot GE-EPI”. In: *NeuroImage* 139 (Oct. 1, 2016), pp. 337–345. ISSN: 1053-8119.

[128] Ida Fredriksson, Pei-Jung Tsai, Aniruddha Shekara, Ying Duan, Sarah V. Applebey, Hanbing Lu, Jennifer M. Bossert, Yavin Shaham, and Yihong Yang. “Orbitofrontal cortex and dorsal striatum functional connectivity predicts incubation of opioid craving after voluntary abstinence”. In: *Proceedings of the National Academy of Sciences* 118.43 (Oct. 26, 2021). Publisher: National Academy of Sciences Section: Biological Sciences. ISSN: 0027-8424, 1091-6490.

[129] Andrew S. Lowe, Steve C. R. Williams, Mark R. Symms, Ian P. Stolerman, and Mohammed Shoaib. “Functional Magnetic Resonance Neuroimaging of Drug Dependence: Naloxone-Precipitated Morphine Withdrawal”. In: *NeuroImage* 17.2 (Oct. 1, 2002), pp. 902–910. ISSN: 1053-8119.

[130] Y. B. Shah, L. Haynes, M. J. W. Prior, C. A. Marsden, P. G. Morris, and V. Chapman. “Functional magnetic resonance imaging studies of opioid receptor-mediated modulation of noxious-evoked BOLD contrast in rats”. In: *Psychopharmacology* 180.4 (Aug. 1, 2005), pp. 761–773. ISSN: 1432-2072.

[131] R. A. Wise. “Opiate reward: sites and substrates”. In: *Neuroscience and Biobehavioral Reviews* 13.2 (1989), pp. 129–133. ISSN: 0149-7634.

[132] Roy A. Wise and Michael A. Bozarth. “Brain reward circuitry: Four circuit elements “wired” in apparent series”. In: *Brain Research Bulletin* 12.2 (Feb. 1984), pp. 203–208. ISSN: 03619230.

[133] Haiyun Xu, Shi-Jiang Li, Jerzy Bodurka, Xiaoli Zhao, Zheng Xiong Xi, and Elliot A Stein. “Heroin-induced neuronal activation in rat brain assessed by functional MRI”. In: *Neuroreport* 11.5 (2000), pp. 1085–1092.

[134] I. Nylander, M. Vlaskovska, and L. Terenius. “The effects of morphine treatment and morphine withdrawal on the dynorphin and enkephalin systems in sprague-dawley rats”. In: *Psychopharmacology* 118.4 (Apr. 1, 1995), pp. 391–400. ISSN: 1432-2072.

[135] Yingjie Zhu, Carl F.R. Wienecke, Gregory Nachtrab, and Xiaoke Chen. “A thalamic input to the nucleus accumbens mediates opiate dependence”. In: *Nature* 530.7589 (Feb. 11, 2016), pp. 219–222. ISSN: 0028-0836.

[136] Hailan Hu. “Reward and Aversion”. In: *Annual Review of Neuroscience* 39 (Volume 39, 2016 July 8, 2016). Publisher: Annual Reviews, pp. 297–324. ISSN: 0147-006X, 1545-4126.

[137] Olivia Uddin, Carleigh Jenne, Megan E. Fox, Keiko Arakawa, Asaf Keller, and Nathan Cramer. *Divergent profiles of fentanyl withdrawal and associated pain in mice and rats*. Section: New Results Type: article. bioRxiv, Nov. 16, 2020, p. 2020.11.16.384818.

[138] S Kügler, E Kilic, and Mathias Bähr. “Human synapsin 1 gene promoter confers highly neuron-specific long-term transgene expression from an adenoviral vector in the adult rat brain depending on the transduced area”. In: *Gene therapy* 10.4 (2003), pp. 337–347.

[139] AJ McGeorge and RLM Faull. “The organization of the projection from the cerebral cortex to the striatum in the rat”. In: *Neuroscience* 29.3 (1989), pp. 503–537.

[140] Lauri Nummenmaa, Jussi Hirvonen, Jarna C Hannukainen, Heidi Immonen, Markus M Lindroos, Paulina Salminen, and Pirjo Nuutila. “Dorsal striatum and its limbic connectivity mediate abnormal anticipatory reward processing in obesity”. In: *PloS one* 7.2 (2012), e31089.

[141] Estela Camara, Antoni Rodriguez-Fornells, and Thomas F Münte. “Functional connectivity of reward processing in the brain”. In: *Frontiers in human neuroscience* 2 (2009), p. 419.

[142] Soyon Ahn, Haiyan Zou, Jeremy K Seamans, and Anthony G Phillips. "Differential patterns of basal and naloxone-evoked dopamine efflux in the rat dorsal and ventral striatum following prolonged-intermittent exposure to morphine". In: *European Journal of Neuroscience* 59.6 (2024), pp. 1067–1078.

[143] Ehsan Shokri-Kojori, Gene-Jack Wang, and Nora D Volkow. "Naloxone precipitated withdrawal increases dopamine release in the dorsal striatum of opioid dependent men". In: *Translational Psychiatry* 11.1 (2021), p. 445.

[144] Carolyn W Roman, Victor A Derkach, and Richard D Palmiter. "Genetically and functionally defined NTS to PBN brain circuits mediating anorexia". In: *Nature communications* 7.1 (2016), p. 11905.

[145] Julie Le Merrer, Jérôme AJ Becker, Katia Befort, and Brigitte L Kieffer. "Reward processing by the opioid system in the brain". In: *Physiological reviews* (2009).

[146] Laura J Sim-Selley, Dana E Selley, Leslie J Vogt, Steven R Childers, and Thomas J Martin. "Chronic heroin self-administration desensitizes μ opioid receptor-activated G-proteins in specific regions of rat brain". In: *Journal of Neuroscience* 20.12 (2000), pp. 4555–4562.

[147] Ying Yu, Jun Qin, Meizhen Liu, Qingyuan Ruan, Yiliang Li, and Zhaohui Zhang. "Role of Rho kinase in lysophosphatidic acid-induced altering of blood-brain barrier permeability". In: *International Journal of Molecular Medicine* 33.3 (Mar. 2014), pp. 661–669. ISSN: 1791-244X.

[148] Kayo Masago, Yasuyuki Kihara, Keisuke Yanagida, Fumie Hamano, Shinsuke Nakagawa, Masami Niwa, and Takao Shimizu. "Lysophosphatidic acid receptor, LPA6, regulates endothelial blood-brain barrier function: Implication for hepatic encephalopathy". In: *Biochemical and Biophysical Research Communications* 501.4 (July 2, 2018), pp. 1048–1054. ISSN: 1090-2104.

[149] Cynthia Hajal, Giovanni S Offeddu, Yoojin Shin, Shun Zhang, Olga Morozova, Dean Hickman, Charles G Knutson, and Roger D Kamm. "Engineered human blood–brain barrier microfluidic model for vascular permeability analyses". In: *Nature protocols* 17.1 (2022), pp. 95–128.

[150] Jürgen Götz, Liviu-Gabriel Bodea, and Michel Goedert. "Rodent models for Alzheimer disease". In: *Nature Reviews Neuroscience* 19.10 (2018), pp. 583–598.

[151] Tatiana M Kazdoba, Prescott T Leach, Jill L Silverman, and Jacqueline N Crawley. "Modeling fragile X syndrome in the Fmr1 knockout mouse". In: *Intractable & rare diseases research* 3.4 (2014), pp. 118–133.

[152] Shuangyang Zhang, Li Qi, Xipan Li, Jiaming Liu, Shixian Huang, Jian Wu, Ruiyuan Liu, Yanqiu Feng, Qianjin Feng, and Wufan Chen. "Photoacoustic imaging of living mice enhanced with a low-cost contrast agent". In: *Biomedical Optics Express* 10.11 (2019), pp. 5744–5754.

[153] Tamar Koren et al. "Insular cortex neurons encode and retrieve specific immune responses". In: *Cell* 184.24 (Nov. 24, 2021), 5902–5915.e17. ISSN: 0092-8674.

[154] Casey J Guenthner, Kazunari Miyamichi, Helen H Yang, H Craig Heller, and Liqun Luo. "Permanent genetic access to transiently active neurons via TRAP: targeted recombination in active populations". In: *Neuron* 78.5 (2013), pp. 773–784.